1

Cyclic Loading/Unloading Tensile Fatigue of Ceramic-Matrix Composites

1.1 Introduction

Ceramic materials possess high strength and modulus at elevated temperature, but their use as structural components is severely limited due to their brittleness. Continuous fiber-reinforced ceramic-matrix composites (CMCs), by incorporating fibers in ceramic matrices, not only exploit their attractive high-temperature strength but also reduce the propensity for catastrophic failure (Naslain 2004; Cheng 2010; Li 2013, 2016a,b).

As the strain-to-failure of the matrix tends to be less than that of the fibers, the first noticeable damage event under tensile loading in the fiber direction is the occurrence of matrix cracks perpendicular to the loading direction (Ramakrishnan and Arunachalam 1993; Dalmaz et al. 1996). The matrix cracks will develop, and some matrix cracks will deflect along the fiber/matrix interface as the load increases (Chiang 2001). When multiple matrix cracking, interface debonding, and sliding occur, interface shear stress transfers loads between the fiber and matrix, which is critical for the nonlinear behavior of the C/SiC CMCs (Curtin 2000).

Upon unloading and subsequent reloading, stress–strain hysteresis loops develop due to the frictional sliding that occurs along any interface debonded region (Rouby and Reynaud 1993; Evans et al. 1995; Reynaud 1996; Mei and Cheng 2009). Kotil et al. (1990) firstly performed an investigation on the effect of interface shear stress on the shape and area of the hysteresis loops. Pryce and Smith (1993) investigated the effect of interface partially debonding on the hysteresis loops based on the assumption of purely frictional load transfer between the fiber and matrix. Based on the Pryce–Smith model, Keith and Kedward (1995) investigated the effect of hysteresis loops when fiber/matrix interface is completely debonded. Solti et al. (1995) investigated the effect of hysteresis loops when fiber/matrix interface was chemically bonded and partially debonded by adopting the maximum interface shear stress criterion to determine the interface debonded length. Ahn and Curtin (1997) investigated the effect of matrix stochastic cracking on hysteresis loops by assuming the two-parameter Weibull distribution of matrix flaw and compared with the Pryce–Smith model. Li et al. (2009) investigated the effect of interface debonding and fiber Poisson contraction on hysteresis loops when fiber/matrix interface was chemically

Thermomechanical Fatigue of Ceramic-Matrix Composites, First Edition. Longbiao Li.

bonded. It was found that after unloading completely, the residual strain and the area of the hysteresis loops decrease as the interface debonded energy and interface frictional coefficient increase. Li and Song (2010a, 2011a) developed an approach to estimate interface shear stress and interface frictional coefficient of CMCs from hysteresis loops. It was found that the interface shear stress and interface frictional coefficient degraded as cycle increased, and the degradation rate depends on the fatigue maximum stress, fatigue load ratio, and loading rate. Fantozzi and Reynaud (2009) investigated the fatigue hysteresis behavior of bi- or multidirectional (cross-weave, cross-ply, 2.5D, $[0/+60/-60]_n$) with SiC or C long fiber-reinforced SiC, MAS-L, Si-B-C, or C matrix at room temperature and at high temperature under inert and oxidation atmosphere. It was found that the macroscopic hysteresis behavior of these materials was not always controlled by the friction at the fiber/matrix interfaces but can be controlled by the friction at the yarn/matrix, yarn/yarn, or ply/ply interface. By assuming that the mechanical behavior of the composite is mainly controlled by the mechanical behavior of the longitudinal yarns, the hysteresis loop shape variation of theses composites during cyclic loading was analyzed. It should be noted that the models mentioned earlier do not consider the effect of fiber failure on hysteresis loops. Upon unloading and subsequent reloading, the fracture and intact fibers both slip in the interface debonded region, which affect the shape, area, and location of the hysteresis loops (Kun and Herrmann 2000; Yang and Mall 2003; Li and Song 2011b).

In this chapter, the cyclic loading/unloading hysteresis behavior of CMCs with different fiber preforms, i.e. unidirectional, cross-ply, 2D and 2.5D woven, 3D braided, and 3D needled, are investigated. Based on fiber sliding mechanisms, the hysteresis loop models considering different interface slip cases are developed. The matrix crack spacing and interface debonding length are obtained by matrix cracking statistical model and fracture mechanics interface debonding criterion. The two-parameter Weibull model is used to describe fiber strength distribution. The stress carried by the intact and fracture fibers at the matrix crack plane during unloading and subsequent reloading is determined by the Global Load Sharing (GLS) criterion. The axial stress distribution of the intact fibers is determined based on the damage mechanisms of fiber sliding relative to matrix in the interface debonded region. The unloading interface counter slip length and reloading interface new slip length are determined by the fracture mechanics approach. The effects of fiber volume fraction, matrix cracking density, interface shear stress, interface debonded energy, and fiber failure on the hysteresis loops, hysteresis dissipated energy, hysteresis width, and hysteresis modulus are analyzed. The hysteresis loops, hysteresis dissipated energy, and hysteresis modulus of unidirectional, cross-ply, 2D and 2.5D woven, 3D braided, and 3D needled CMCs are predicted.

1.2 Unidirectional Ceramic-Matrix Composites

The cyclic loading/unloading hysteresis loops of unidirectional CMCs are investigated for different fiber volume fraction, matrix cracking density,

fiber/matrix interface shear stress, and interface debonded energy with and without considering fiber failure. The experimental C/SiC, C/Si_3N_4, SiC/Si_3N_4, and SiC/CAS composites are predicted for different peak stresses. The peak stress affects the interface debonding and sliding and also the hysteresis loops.

1.2.1 Materials and Experimental Procedures

1.2.1.1 C/SiC Composite

The unidirectional T-700™ C/SiC composites were manufactured by the hot-pressing method, which offered the ability to fabricate dense composites via a liquid phase sintering method at a low temperature. The fibers have an average diameter of 7 μm and come on a spool as a tow of 12K fibers. The volume fraction of fibers was approximately 42%. Low pressure chemical vapor infiltration (CVI) was employed to deposit approximately 5–20 layers of PyC/SiC with the mean thickness of 0.2 μm in order to enhance the desired nonlinear/non-catastrophic tensile behavior. The nano-SiC powder and sintering additives were ball milled for four hours using SiC balls. After drying, the powders were dispersed in xylene with polycarbonsilane (PCS) to form the slurry. Carbon fiber tows were infiltrated by the slurry and wound to form aligned unidirectional composite sheets. After drying, the sheets were cut to a size of 150 mm × 150 mm and pyrolyzed in argon. Then, the sheets were stacked in a graphite die and sintered by hot pressing.

The dog-bone shaped specimens, with 120 mm length, 3.2 mm thickness, and 4.5 mm width in the gage section, were cut from the 150 mm × 150 mm panels by water cutting. Specimens were further coated with SiC of about 20 μm thick by chemical vapor deposition (CVD) to prevent oxidation at high temperature. These processing steps resulted in a material having bulk density about 2.0 g/cm^3 and an open porosity below 5%.

The cyclic loading/unloading tensile experiments at room temperature were conducted on an MTS Model 809 servo hydraulic load frame (MTS Systems Corp., Minneapolis, MN) equipped with edge-loaded grips, operated at a loading rate of 2.0 MPa/s. Gage-section strains were measured using a clip-on extensometer (Model No. 634.12F-24, MTS Systems Corp., modified for a 25 mm gage length). Direct observations of matrix cracking were made using HiROX optical microscope. Matrix crack densities were determined by counting the number of cracks in a length of about 15 mm.

1.2.1.2 C/Si_3N_4 and SiC/Si_3N_4 Composites

THORNEL P25™ (Amoco, USA) carbon fiber-reinforced silicon nitride matrix (Ube Industries, Japan) composite (C/Si_3N_4 CMCs) was prepared by Joint Research Centre, Petten, NL. In order to promote liquid phase sintering of silicon nitride, the powder mixture for the preparation of the slurry contains 10% by weight of Al_2O_3 and Y_2O_3. The individual unidirectional fibrous preforms were infiltrated by the mixture of Si_3N_4, Al_2O_3, and Y_2O_3. The densification process was conducted by sintering under load of 27 MPa at a temperature of 1700 °C for 30 minutes and 1650 °C for 60 minutes. The final dimensions of the composite panels were fixed to be 72 mm × 45 mm × 3.9 mm to control the

fiber volume fraction and ensure the reproducibility of the process. The fiber volume fraction of C/Si_3N_4 composite was about 40%, and the average density was 2.6–2.7 g/cm^3. The porosity of the composite is less than 1%.

The Hi-Nicalon™ SiC (Nippon Carbon Co., Ltd., Tokyo, Japan) fiber-reinforced silicon nitride (Ube Industries, Japan) matrix composite (SiC/Si_3N_4 CMCs) was also fabricated by Joint Research Centre, Petten, NL. The pyrolytic carbon (PyC) interphase was deposited on the Hi-Nicalon fibers by CVD. Based on the interface bonding condition between fibers and matrix, the SiC/Si_3N_4 composite can be divided into two cases, i.e. type A composite, where the carbon coating is perfectly attached to SiC fibers, indicating strong interface bonding; and type B composite, where the adhesion between SiC fibers and carbon coating is low. The volume fraction of the composite was about 30%, and the average density was 2.8–2.95 g/cm^3. The porosity of the composite is less than 3%.

The mechanical testing specimen was rectangle in shape with dimensions of 72 mm × 7 mm × 1.5 mm for C/Si_3N_4 composite and 72 mm × 7 mm × 1.2 mm for SiC/Si_3N_4 composite according to the French AFNOR standardization (French National Organization for Standardization, 1989). Cyclic loading/unloading tensile and tension–tension fatigue tests of unidirectional C/Si_3N_4 and SiC/Si_3N_4 composites were conducted on an Instron Model 8511 servo hydraulic load frame (INSTRON System Corp., Norwood, Massachusetts, USA). The clamping stresses performed on the surface of the specimens are less than 5 MPa for C/Si_3N_4 composite and 9 MPa for SiC/Si_3N_4 composite. The longitudinal deformation was measured with the aid of an extensometer Schenk knife of 14 mm. The cyclic tensile loading/unloading tests were conducted under strain control with the loading rate of 0.05 mm/min. During tensile loading, the test is interrupted regularly, and the applied stress is maintained using the load control mode to make replicas on the front surface of the specimen, in order to *in situ* measure the matrix cracking density at different applied stress levels.

1.2.1.3 SiC/CAS Composite

Nicalon™ SiC fiber-reinforced calcium aluminosilicate glass ceramic matrix laminates were manufactured by hot-pressing prepreg. Tensile coupons, 80 mm by 20 mm, were cut from the laminates. Abraded and etched aluminum end tags were bonded to specimens for ease of gripping in wedge grips. Quasi-static tests were carried out using Instron 1175 under displacement control at a crosshead speed of 0.05 mm/min. Direct observations of matrix cracking were made using optical and scanning electron microscopy of the polished coupon edges. Crack densities were determined by counting the number of cracks in a gage length of about 15 mm.

1.2.2 Theoretical Analysis

1.2.2.1 Stress Analysis

Upon first loading to the peak stress of σ_{max}, which is higher than the initial matrix cracking stress σ_{mc}, it is assumed that matrix cracks run across the cross section of the composites and fiber/matrix interface debonds. To analyze stress distributions in the fiber and the matrix, a unit cell is extracted from the

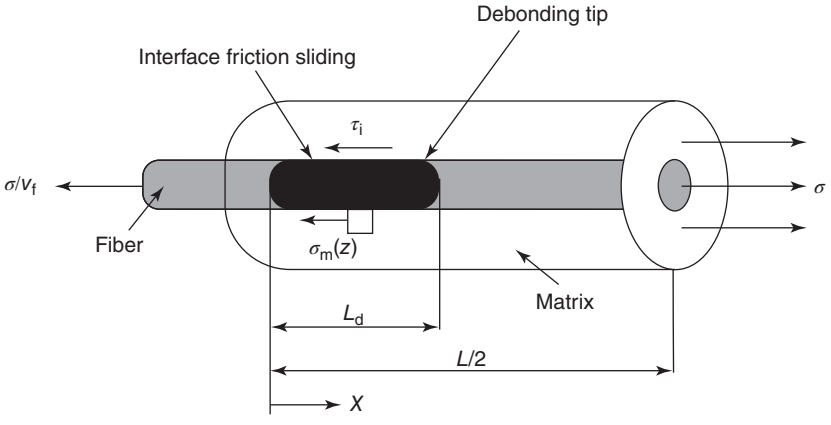

Figure 1.1 The unit cell of the Budiansky–Hutchinson–Evans shear-lag model.

CMCs, as shown in Figure 1.1. The unit cell contains a single fiber surrounded by a hollow cylinder of matrix. The fiber radius is r_f, and the matrix radius is $R(R = r_f/V_f^{1/2})$. The length of the unit cell is $l_c/2$, which is just the half matrix crack space. The fiber/matrix interface debonding length is l_d. At the matrix crack plane, fibers carry all the loads (σ/V_f), where σ denotes far-field applied stress and V_f denotes fiber volume fraction. The shear-lag model adopted by Budiansky–Hutchinson–Evans (Budiansky et al. 1986) is applied to perform stress and strain calculations in the interface debonded region ($x \in [0, l_d]$) and interface bonded region ($x \in [l_d, l_c/2]$):

$$\sigma_f(x) = \begin{cases} \frac{\sigma}{V_f} - \frac{2\tau_i}{r_f}x, & x \in (0, l_d) \\ \sigma_{fo} + \left(\frac{V_m}{V_f}\sigma_{mo} - 2\frac{l_d}{r_f}\tau_i\right)\exp\left(-\rho\frac{x-l_d}{r_f}\right), & x \in (l_d, l_c/2) \end{cases} \tag{1.1}$$

$$\sigma_m(x) = \begin{cases} 2\tau_i\frac{V_f}{V_m}\frac{x}{r_f}, & x \in (0, l_d) \\ \sigma_{mo} - \left(\sigma_{mo} - 2\tau_i\frac{V_f}{V_m}\frac{l_d}{r_f}\right)\exp\left[-\frac{\rho(x-l_d)}{r_f}\right], & x \in (l_d, l_c/2) \end{cases} \tag{1.2}$$

$$\tau_i(x) = \begin{cases} \tau_i, & x \in (0, l_d) \\ \frac{\rho}{2}\left(\frac{V_m}{V_f}\sigma_{mo} - 2\tau_i\frac{l_d}{r_f}\right)\exp\left[-\frac{\rho(x-l_d)}{r_f}\right], & x \in (l_d, l_c/2) \end{cases} \tag{1.3}$$

where V_m denotes the matrix volume fraction, τ_i denotes the fiber/matrix interface shear stress, and ρ denotes the shear-lag parameter (Budiansky et al. 1986).

$$\rho^2 = \frac{4E_cG_m}{V_mE_mE_f\varphi} \tag{1.4}$$

where G_m denotes matrix shear modulus, and

$$\varphi = -\frac{2\ln V_f + V_m(3 - V_f)}{2V_m^2} \tag{1.5}$$

σ_{fo} and σ_{mo} denote fiber and matrix axial stress in the interface bonded region, respectively:

$$\sigma_{fo} = \frac{E_f}{E_c}\sigma + E_f(\alpha_c - \alpha_f)\Delta T \tag{1.6}$$

$$\sigma_{mo} = \frac{E_m}{E_c}\sigma + E_m(\alpha_c - \alpha_m)\Delta T \tag{1.7}$$

where E_f, E_m, and E_c denote fiber, matrix, and composite elastic modulus, respectively. α_f, α_m, and α_c denote fiber, matrix, and composite thermal expansion coefficient. ΔT denotes the temperature difference between the fabricated temperature T_0 and testing temperature T_1 ($\Delta T = T_1 - T_0$). The axial elastic modulus of composite is approximated by the rule of mixture:

$$E_c = V_f E_f + V_m E_m \tag{1.8}$$

When the fiber fails, the fiber axial stress distribution in the interface debonded region and bonded region is determined using the following equation:

$$\sigma_f(x) = \begin{cases} T - \frac{2\tau_i}{r_f}x, & x \in (0, l_d) \\ \sigma_{fo} + \left(T - \sigma_{fo} - 2\frac{l_d}{r_f}\tau_i\right)\exp\left(-\rho\frac{x-l_d}{r_f}\right), & x \in (l_d, l_c/2) \end{cases} \tag{1.9}$$

where T denotes the intact fiber axial stress at the matrix cracking plane.

1.2.2.2 Matrix Cracking

When loading of fiber-reinforced CMCs, cracks typically initiate within the composite matrix since the strain-to-failure of the matrix is usually less than that of the fiber. The matrix crack spacing decreases with applied stress above the initial matrix cracking stress σ_{mc} and may eventually attain saturation at stress σ_{sat}. There are four dominant failure criterions for modeling matrix cracking evolution of unidirectional CMCs, i.e. the maximum stress criterion (Daniel and Lee 1993), the energy balance approach (Aveston et al. 1971; Zok and Spearing 1992; Zhu and Weitsman 1994), the critical matrix strain energy criterion (Solti et al. 1995), and the statistical failure approach (Curtin 1993). The brittle nature of the matrix material and the possible formation of initial cracks distribution throughout the microstructure suggest that a statistical approach to matrix crack evolution is warranted in CMCs. The tensile strength of the brittle matrix is assumed to be described using the two-parameter Weibull distribution. The matrix failure can be determined using the following equation (Curtin 1993):

$$P_m = 1 - \exp\left[-\left(\frac{\sigma_m}{\sigma_R}\right)^m\right] \tag{1.10}$$

where σ_m denotes the tensile stress in the matrix and σ_R and m denote the matrix characteristic strength and matrix Weibull modulus, respectively. To estimate the instantaneous matrix crack space with increasing applied stress, it leads to the following equation:

$$P_m = l_{sat}/l_c \tag{1.11}$$

where l_c denotes the instantaneous matrix crack space and l_{sat} denotes the saturation matrix crack space. Using Eqs. (1.10) and (1.11), the instantaneous matrix crack space can be determined using the following equation (Curtin 1993):

$$l_c = l_{sat}\left\{1 - \exp\left[-\left(\frac{\sigma_m}{\sigma_R}\right)^m\right]\right\}^{-1} \tag{1.12}$$

1.2.2.3 Interface Debonding

When matrix crack propagates to the fiber/matrix interface, it deflects along the fiber/matrix interface. There are two approaches to the problem of fiber/matrix interface debonding, i.e. the shear stress approach (Hsueh 1996) and the fracture mechanics approach (Gao et al. 1988). It has been proved that the fracture mechanics approach is preferred to the shear stress approach for interface debonding (Sun and Singh 1998). The fracture mechanics approach is adopted in the present analysis. The interface debonding criterion can be described using the following equation (Gao et al. 1988):

$$\xi_d = \frac{F}{4\pi r_f}\frac{\partial w_f(0)}{\partial l_d} - \frac{1}{2}\int_0^{l_d}\tau_i\frac{\partial v(x)}{\partial l_d}dx \tag{1.13}$$

where $F(=\pi r_f^2\sigma/V_f)$ denotes the fiber load at the matrix crack plane, $w_f(0)$ denotes the fiber axial displacement at the matrix crack plane, and $v(x)$ denotes the relative displacement between the fiber and the matrix. The axial displacement of fiber and matrix can be determined using the following equations:

$$\begin{aligned} w_f(x) &= \int_x^{l_c/2}\frac{\sigma_f}{E_f}dx = \frac{\sigma}{V_f E_f}(l_d - x) - \frac{\tau_i}{r_f E_f}(l_d^2 - x^2) \\ &\quad -\frac{2\tau_i}{\rho E_f}l_d + \frac{r_f V_m E_m}{\rho V_f E_f E_c}\sigma + \frac{\sigma}{E_c}(l_c/2 - l_d) \end{aligned} \tag{1.14}$$

$$\begin{aligned} w_m(x) &= \int_x^{l_c/2}\frac{\sigma_m}{E_m}dx \\ &= \frac{V_f\tau_i}{V_m E_m r_f}(l_d^2 - x^2) + \frac{2V_f\tau_i}{\rho V_m E_m}l_d - \frac{r_f}{\rho E_c}\sigma + \frac{\sigma}{E_c}(l_c/2 - l_d) \end{aligned} \tag{1.15}$$

Using Eqs. (1.14) and (1.15), the relative displacement between the fiber and matrix can be described using the following equation:

$$\begin{aligned} v(x) &= |w_f(x) - w_m(x)| \\ &= \frac{\sigma}{V_f E_f}(l_d - x) - \frac{\tau_i E_c}{V_m E_m E_f r_f}(l_d^2 - x^2) - \frac{2\tau_i E_c l_d}{\rho V_m E_m E_f} + \frac{r_f}{\rho V_f E_f}\sigma \end{aligned} \tag{1.16}$$

Substituting $w_f(x=0)$ and $v(x)$ into Eq. (1.13), it forms the following equation

$$\frac{E_c\tau_i^2}{V_m E_m E_f r_f}l_d^2 + \left(\frac{E_c\tau_i^2}{\rho V_m E_m E_f} - \frac{\tau_i\sigma}{V_f E_f}\right)l_d + \frac{r_f V_m E_m\sigma^2}{4{V_f}^2 E_f E_c} - \frac{r_f\tau_i}{2\rho V_f E_f}\sigma - \xi_d = 0 \tag{1.17}$$

To solve Eq. (1.17), the interface debonding length can be determined using the following equation:

$$l_{\mathrm{d}} = \frac{r_{\mathrm{f}}}{2}\left(\frac{V_{\mathrm{m}}E_{\mathrm{m}}\sigma}{V_{\mathrm{f}}E_{\mathrm{c}}\tau_{\mathrm{i}}} - \frac{1}{\rho}\right) - \sqrt{\left(\frac{r_{\mathrm{f}}}{2\rho}\right)^2 + \frac{r_{\mathrm{f}}V_{\mathrm{m}}E_{\mathrm{m}}E_{\mathrm{f}}}{E_{\mathrm{c}}\tau_{\mathrm{i}}^2}\xi_{\mathrm{d}}} \tag{1.18}$$

1.2.2.4 Fiber Failure

There are relatively fewer models for the fiber failure of CMCs compared with analyses for damage mechanisms, such as matrix cracking and interface debonding. As fibers begin to break, the loads dropped by the broken fibers must be transferred to the intact fibers in the cross section. Two dominant failure criterions are present in the literature for modeling fiber failure: GLS and Local Load Sharing (LLS). The GLS criterion assumes that the load from any one fiber is transferred equally to all other intact fibers in the same cross-section plane. The GLS assumption neglects any local stress concentrations in the neighborhood of existing breaks and is expected to be accurate when the interface shear stress is sufficiently low. Models that include GLS explicitly have been developed by Thouless and Evans (1988), Cao and Thouless (1990), Sutcu (1989), Schwietert and Steif (1990), Curtin (1991), Weitsman and Zhu (1993), Hild et al. (1994), Zhu and Weitsman (1994), Curtin et al. (1998), Paar et al. (1998), and Liao and Reifsnider (2000). The LLS assumes that the load from the broken fiber is transferred to the neighborhood intact fibers and is expected to be accurate when the interface shear stress is sufficiently high. Models that include LLS explicitly have been developed by Zhou and Curtin (1995), Dutton et al. (2000), and Xia and Curtin (2000).

The two-parameter Weibull model is adopted to describe fiber strength distribution, and the GLS assumption is used to determine the loads carried by the intact and fracture fibers (Curtin 1991):

$$\frac{\sigma}{V_{\mathrm{f}}} = T(1 - P(T)) + \langle T_{\mathrm{b}}\rangle P(T) \tag{1.19}$$

where $\langle T_{\mathrm{b}}\rangle$ denotes the load carried by the broken fibers and $P(T)$ denotes the fiber failure volume fraction (Curtin 1991):

$$P(T) = 1 - \exp\left[-\left(\frac{T}{\sigma_{\mathrm{c}}}\right)^{m_{\mathrm{f}}+1}\right] \tag{1.20}$$

where m_{f} is the fiber Weibull modulus and σ_{c} is the fiber characteristic strength of a length δ_{c} of fiber:

$$\sigma_{\mathrm{c}} = \left(\frac{l_{\mathrm{o}}\sigma_{\mathrm{o}}^{m_{\mathrm{f}}}\tau_{\mathrm{i}}}{r_{\mathrm{f}}}\right)^{1/m_{\mathrm{f}}+1}, \quad \delta_{\mathrm{c}} = \left(\frac{\sigma_{\mathrm{o}}r_{\mathrm{f}}l_{\mathrm{o}}^{1/m_{\mathrm{f}}}}{\tau_{\mathrm{i}}}\right)^{m_{\mathrm{f}}/m_{\mathrm{f}}+1} \tag{1.21}$$

where l_{o} is the reference length and σ_{o} is the fiber reference strength of a length of l_{o} of fiber.

When fiber fractures, the fiber stress drops to zero at the break, and the stress in the fiber builds up through the stress transfer across the fiber/matrix interface

shear stress:

$$T_{\mathrm{b}}(x) = \frac{2\tau_{\mathrm{i}}}{r_{\mathrm{f}}}x \tag{1.22}$$

The sliding length l_{f} required to build the fiber stress up to its previous intact value is given by the following equation:

$$l_{\mathrm{f}} = \frac{r_{\mathrm{f}}T}{2\tau_{\mathrm{i}}} \tag{1.23}$$

The probability distribution $f(x)$ of the distance x of a fiber break from reference matrix crack plane, provided that a break occurs within a distance $\pm l_{\mathrm{f}}$, is constructed based on the Weibull statistics by Phoenix and Raj (1992):

$$f(x) = \frac{1}{P(T)l_{\mathrm{f}}}\left(\frac{T}{\sigma_{\mathrm{c}}}\right)^{m_{\mathrm{f}}+1}\exp\left[-\left(\frac{x}{l_{\mathrm{f}}}\right)\left(\frac{T}{\sigma_{\mathrm{c}}}\right)^{m_{\mathrm{f}}+1}\right], \quad x \in [0, l_{\mathrm{f}}] \tag{1.24}$$

where $x \in [0, l_{\mathrm{f}}]$.

Using Eqs. (1.22) and (1.24), the average stress carried by the broken fiber is given by the following equation:

$$\langle T_{\mathrm{b}}\rangle = \int_0^{l_{\mathrm{f}}} T_{\mathrm{b}}(x)f(x)\mathrm{d}x = T\left[\left(\frac{\sigma_{\mathrm{c}}}{T}\right)^{m_{\mathrm{f}}+1} - \frac{1-P(T)}{P(T)}\right] \tag{1.25}$$

Substituting Eq. (1.25) into Eq. (1.19) leads to the following equation:

$$\frac{\sigma}{V_{\mathrm{f}}} = T\left(\frac{\sigma_{\mathrm{c}}}{T}\right)^{m_{\mathrm{f}}+1}\left\{1 - \exp\left[-\left(\frac{T}{\sigma_{\mathrm{c}}}\right)^{m_{\mathrm{f}}+1}\right]\right\} \tag{1.26}$$

The load carried by the intact fibers T at the matrix crack plane for different applied stress can be obtained by solving Eq. (1.26), and then the fiber failure volume fraction can be obtained by substituting T into Eq. (1.20). When the load carried by the intact fibers reach the maximum value, composites fail. The composite ultimate tensile strength σ_{UTS} is given by the following equation:

$$\sigma_{\mathrm{UTS}} = V_{\mathrm{f}}\sigma_{\mathrm{c}}\left(\frac{2}{m_{\mathrm{f}}+2}\right)^{\frac{1}{m_{\mathrm{f}}+1}}\left(\frac{m_{\mathrm{f}}+1}{m_{\mathrm{f}}+2}\right) \tag{1.27}$$

1.2.2.5 Hysteresis Theories

When CMCs are under tensile loading, matrix cracking occurs first. As the applied stress increases, the amounts of the matrix cracks increase, partially matrix cracks deflect along fiber/matrix interface, and some matrix cracks propagate penetration through fibers, which makes fiber fracture. The interface debonded length, which includes the effect of fiber failure, is given by the following equation:

$$l_{\mathrm{df}} = \frac{r_{\mathrm{f}}}{2}\left(\frac{V_{\mathrm{m}}E_{\mathrm{m}}}{E_{\mathrm{c}}\tau_{\mathrm{i}}}T - \frac{1}{\rho}\right) - \sqrt{\left(\frac{r_{\mathrm{f}}}{2\rho}\right)^2 - \frac{r_{\mathrm{f}}^2V_{\mathrm{f}}V_{\mathrm{m}}E_{\mathrm{f}}E_{\mathrm{m}}T}{4E_{\mathrm{c}}^2\tau_{\mathrm{i}}{}^2}\left(T - \frac{\sigma}{V_{\mathrm{f}}}\right) + \frac{r_{\mathrm{f}}V_{\mathrm{m}}E_{\mathrm{m}}E_{\mathrm{f}}}{E_{\mathrm{c}}\tau_{\mathrm{i}}{}^2}\xi_{\mathrm{d}}} \tag{1.28}$$

It is shown from Eq. (1.28) that, when none of the fibers fails, $T = \sigma/V_f$ and $l_{df} = l_d$. When $l_{df} < l_c/2$, the fiber/matrix interface partially debonds; and when $l_{df} = l_c/2$, the fiber/matrix interface completely debonds. Two cases of hysteresis loops are discussed in the following: (i) the interface partially debonding and the fiber sliding relative to matrix in the interface debonded region upon unloading and subsequent reloading; and (ii) the interface completely debonding and the fiber sliding relative to matrix in the entire matrix crack spacing upon unloading and subsequent reloading.

1.2.2.5.1 Interface Partially Debonding When the fiber/matrix interface partially debonds, the unit cell can be divided into the interface debonded region ($x \in [0, l_{df}]$) and the interface bonded region ($x \in [l_{df}, l_c/2]$). Upon unloading to the applied stress of σ ($\sigma_{min} < \sigma < \sigma_{max}$), the interface debonded region can be divided into the interface counter slip region ($x \in [0, y]$) and the interface slip region ($x \in [y, l_{df}]$).

The fiber axial stress distribution upon unloading is given by the following equation:

$$\begin{cases} \sigma_f(x) = T^U + \frac{2\tau_i}{r_f}x, & x \in (0, y) \\ \sigma_f(x) = T^U + \frac{2\tau_i}{r_f}(2y - x), & x \in (y, l_{df}) \\ \sigma_f(x) = \sigma_{fo} + \left[T^U - \sigma_{fo} - 2\frac{\tau_i}{r_f}(l_{df} - 2y)\right] \\ \qquad \times \exp\left(-\rho\frac{x - l_{df}}{r_f}\right), & x \in (l_{df}, l_c/2) \end{cases} \tag{1.29}$$

where

$$y = \frac{1}{2}\left\{l_{df} - \left[\frac{r_f}{2}\left(\frac{V_m E_m}{E_c \tau_i}T^U - \frac{1}{\rho}\right) - \sqrt{\left(\frac{r_f}{2\rho}\right)^2 - \frac{r_f^2 V_f V_m E_f E_m T^U}{4E_c^2 \tau_i^2}\left(T^U - \frac{\sigma}{V_f}\right) + \frac{r_f V_m E_m E_f}{E_c \tau_i^2}\xi_d}\right]\right\} \tag{1.30}$$

where T^U denotes the stress carried by the intact fibers at the matrix crack plane upon unloading, which satisfied the relationship of the following equation:

$$\frac{\sigma}{V_f} = 2T\left(\frac{\sigma_c}{T}\right)^{m_f+1}\left\{\exp\left[-\left(\frac{T - T^U}{2T}\right)\left(\frac{T}{\sigma_c}\right)^{m_f+1}\right] - 1 + \frac{1}{2}P(T)\right\} \tag{1.31}$$

Upon reloading to the applied stress of σ, slip again occurs near the matrix cracking plane over a distance of z, which denotes the new slip region. The interface debonded region can be divided into the new slip region ($x \in [0, z]$), counter slip region ($x \in [z, y]$), and slip region ($x \in [y, l_{df}]$).

The fiber axial stress distribution upon reloading is given by the following equation:

$$\begin{cases} \sigma_{\mathrm{f}}(x) = T^{\mathrm{R}} - \frac{2\tau_{\mathrm{i}}}{r_{\mathrm{f}}}x, & x \in (0, z) \\ \sigma_{\mathrm{f}}(x) = T^{\mathrm{R}} + \frac{2\tau_{\mathrm{i}}}{r_{\mathrm{f}}}(x - 2z), & x \in (z, y) \\ \sigma_{\mathrm{f}}(x) = T^{\mathrm{R}} - \frac{2\tau_{\mathrm{i}}}{r_{\mathrm{f}}}(x - 2y + 2z), & x \in (y, l_{\mathrm{df}}) \\ \sigma_{\mathrm{f}}(x) = \sigma_{\mathrm{fo}} + \left[T^{R} - \sigma_{\mathrm{fo}} - 2\frac{\tau_{\mathrm{i}}}{r_{\mathrm{f}}}(l_{\mathrm{df}} - 2y + 2z)\right] \\ \qquad \times \exp\left(-\rho\frac{x - l_{\mathrm{df}}}{r_{\mathrm{f}}}\right), & x \in (l_{\mathrm{df}}, l_{\mathrm{c}}/2) \end{cases} \tag{1.32}$$

where

$$z = y - \frac{1}{2} \times \left\{ l_{\mathrm{df}} - \left[\frac{r_{\mathrm{f}}}{2} \left(\frac{V_{\mathrm{m}} E_{\mathrm{m}}}{E_{\mathrm{c}} \tau_{\mathrm{i}}} T^{\mathrm{R}} - \frac{1}{\rho} \right) - \sqrt{ \left(\frac{r_{\mathrm{f}}}{2\rho} \right)^2 - \frac{r_{\mathrm{f}}^2 V_{\mathrm{f}} V_{\mathrm{m}} E_{\mathrm{f}} E_{\mathrm{m}} T^{\mathrm{R}}}{4 E_{\mathrm{c}}^2 \tau_{\mathrm{i}}^2} \left(T^{\mathrm{R}} - \frac{\sigma}{V_{\mathrm{f}}} \right) + \frac{r_{\mathrm{f}} V_{\mathrm{m}} E_{\mathrm{m}} E_{\mathrm{f}}}{E_{\mathrm{c}} \tau_{\mathrm{i}}^2} \xi_{\mathrm{d}} } \right] \right\} \tag{1.33}$$

where T^{R} denotes the stress carried by the intact fibers at the matrix crack plane upon reloading, which satisfies the relationship of the following equation:

$$\frac{\sigma}{V_{\mathrm{f}}} = 2T\left(\frac{\sigma_{\mathrm{c}}}{T}\right)^{m_{\mathrm{f}}+1} \left\{ \exp\left[-\left(\frac{T_{\mathrm{m}}}{2T} \right) \left(\frac{T}{\sigma_{\mathrm{c}}} \right)^{m_{\mathrm{f}}+1} \right] - \exp\left[-\left(\frac{T^{\mathrm{R}} - T + T_{\mathrm{m}}}{2T} \right) \left(\frac{T}{\sigma_{\mathrm{c}}} \right)^{m_{\mathrm{f}}+1} \right] + \frac{1}{2}P(T) \right\} \tag{1.34}$$

where T_{m} satisfies the relationship of the following equation:

$$0 = 2T\left(\frac{\sigma_{\mathrm{c}}}{T}\right)^{m_{\mathrm{f}}+1} \left\{ \exp\left[-\left(\frac{T_{\mathrm{m}}}{2T} \right) \left(\frac{T}{\sigma_{\mathrm{c}}} \right)^{m_{\mathrm{f}}+1} \right] - 1 + \frac{1}{2}P(T) \right\} \tag{1.35}$$

1.2.2.5.2 Completely Debonding of Interface When the fiber/matrix interface completely debonds, the unit cell can be divided into the interface counter slip region ($x \in [0, y]$) and slip region ($x \in [y, l_{\mathrm{c}}/2]$) upon unloading.

The fiber axial stress distribution upon unloading is given by the following equation:

$$\begin{cases} \sigma_{\mathrm{f}}(x) = T^{\mathrm{U}} + \frac{2\tau_{\mathrm{i}}}{r_{\mathrm{f}}}x, & x \in (0, y) \\ \sigma_{\mathrm{f}}(x) = T^{\mathrm{U}} + \frac{2\tau_{\mathrm{i}}}{r_{\mathrm{f}}}(2y - x), & x \in (y, l_{\mathrm{c}}/2) \end{cases} \tag{1.36}$$

where

$$y = \frac{r_{\mathrm{f}}}{4\tau_{\mathrm{i}}}\left[(T - T^{\mathrm{U}}) - \frac{E_{\mathrm{f}}}{E_{\mathrm{c}}}(\sigma_{\max} - \sigma) \right] \tag{1.37}$$

where T^{U} denotes the stress carried by the intact fibers at the matrix crack plane upon unloading, which satisfies Eq. (1.31).

Upon reloading, the unit cell can be divided into the interface new slip region ($x \in [0, z]$), interface counter slip region ($x \in [z, y]$), and slip region ($x \in [y,$

$l_c/2]$). The fiber axial stress distribution upon reloading is given by the following equation:

$$\begin{cases} \sigma_f(x) = T^R - \frac{2\tau_i}{r_f}x, & x \in (0, z) \\ \sigma_f(x) = T^R + \frac{2\tau_i}{r_f}(x - 2z), & x \in (z, y) \\ \sigma_f(x) = T^R - \frac{2\tau_i}{r_f}(x - 2y + 2z), & x \in (y, l_c/2) \end{cases} \tag{1.38}$$

where

$$z = y(\sigma_{min}) - \frac{r_f}{4\tau_i}\left[(T - T^R) - \frac{E_f}{E_c}(\sigma_{max} - \sigma)\right] \tag{1.39}$$

where T^R denotes the stress carried by the intact fibers at the matrix crack plane upon reloading, which satisfies Eq. (1.34).

1.2.2.5.3 Hysteresis Loops and Hysteresis-Based Parameters When damage forms within the composite, the composite strain can be determined using the following equation, which assumes that the composite strain is equivalent to the average strain in an undamaged fiber:

$$\varepsilon_c = \frac{2}{E_f l_c}\int_{l_c/2} \sigma_f(x)dx - (\alpha_c - \alpha_f)\Delta T \tag{1.40}$$

Substituting Eq. (1.29) into Eq. (1.40), the unloading stress–strain relationship for the interface partially debonding is given by the following equation:

$$\varepsilon_c = \frac{T^U}{E_f} + 4\frac{\tau_i}{E_f}\frac{y^2}{r_f l_c} - \frac{\tau_i}{E_f}\frac{1}{r_f l_c}(2y - l_{df})(2y + l_{df} - l_c) - (\alpha_c - \alpha_f)\Delta T \tag{1.41}$$

Substituting Eq. (1.32) into Eq. (1.40), the reloading stress–strain relationship for the interface partially debonding is given by the following equation:

$$\begin{aligned} \varepsilon_c = {} & \frac{T^R}{E_f} - 4\frac{\tau_i}{E_f}\frac{z^2}{r_f l_c} + 4\frac{\tau_i}{E_f}\frac{(y - 2z)^2}{r_f l_c} \\ & + 2\frac{\tau_i}{E_f}\frac{(l_{df} - 2y + 2z)(l_{df} + 2y - 2z - l_c)}{r_f l_c} - (\alpha_c - \alpha_f)\Delta T \end{aligned} \tag{1.42}$$

Substituting Eq. (1.36) into Eq. (1.40), the unloading stress–strain relationship for the interface completely debonding is given by the following equation:

$$\varepsilon_c = \frac{T^U}{E_f} + 4\frac{\tau_i}{E_f}\frac{y^2}{r_f l_c} - 2\frac{\tau_i}{E_f}\frac{(2y - l_c/2)^2}{r_f l_c} - (\alpha_c - \alpha_f)\Delta T \tag{1.43}$$

Substituting Eq. (1.38) into Eq. (1.40), the reloading stress–strain relationship for the interface completely debonding is given by the following equation:

$$\varepsilon_c = \frac{T^R}{E_f} - 4\frac{\tau_i}{E_f}\frac{z^2}{r_f l_c} + 4\frac{\tau_i}{E_f}\frac{(y - 2z)^2}{r_f l_c} - 2\frac{\tau_i}{E_f}\frac{(l_c/2 - 2y + 2z)^2}{r_f l_c} - (\alpha_c - \alpha_f)\Delta T \tag{1.44}$$

The area associated with the hysteresis loops is the dissipated energy during corresponding cycle, which is defined as the following equation:

$$U = \int_{\sigma_{\min}}^{\sigma_{\max}} [\varepsilon_{c\_unload}(\sigma) - \varepsilon_{c\_reload}(\sigma)]d\sigma \tag{1.45}$$

where ε_{c_unload} and ε_{c_reload} denote unloading and reloading strain, respectively. Substituting unloading and reloading strains corresponding to the interface partially and completely debonding into Eq. (1.45), the hysteresis dissipated energy U can be obtained.

The hysteresis width $\Delta\varepsilon$ is defined by the following equation:

$$\Delta\varepsilon = \varepsilon_{c\_unload}\left(\frac{\sigma_{\min} + \sigma_{\max}}{2}\right) - \varepsilon_{c\_reload}\left(\frac{\sigma_{\min} + \sigma_{\max}}{2}\right) \tag{1.46}$$

The hysteresis modulus E is defined by the following equation:

$$E = \frac{\sigma_{\max} - \sigma_{\min}}{\varepsilon_c(\sigma_{\max}) - \varepsilon_c(\sigma_{\min})} \tag{1.47}$$

1.2.3 Results and Discussion

The fatigue hysteresis loops, fatigue hysteresis dissipated energy, fatigue hysteresis width, and fatigue hysteresis modulus of unidirectional SiC/CAS composite are analyzed for different fiber volume fraction, matrix cracking density, fiber/matrix interface shear stress, and interface debonded energy.

1.2.3.1 Effect of Fiber Volume Fraction on Fatigue Hysteresis Loops and Fatigue Hysteresis-Based Damage Parameters

The fatigue hysteresis loops, fatigue hysteresis dissipated energy, fatigue hysteresis width, and fatigue hysteresis modulus of SiC/CAS composite are shown in Figure 1.2 for fiber volume fractions of $V_f = 30\%$ and 40%.

When the fiber volume is $V_f = 30\%$, the fatigue hysteresis dissipated energy increases with fatigue peak stress, i.e. from $U = 22.3\,\text{kJ/m}^3$ at the fatigue peak stress of $\sigma_{\max} = 200\,\text{MPa}$ to $U = 178.6\,\text{kJ/m}^3$ at the fatigue peak stress of $\sigma_{\max} = 400\,\text{MPa}$; the fatigue hysteresis width increases with the fatigue peak stress, i.e. from $\Delta\varepsilon = 0.016\%$ at the fatigue peak stress of $\sigma_{\max} = 200\,\text{MPa}$ to $\Delta\varepsilon = 0.067\%$ at the fatigue peak stress of $\sigma_{\max} = 400\,\text{MPa}$; and the fatigue hysteresis modulus decreases with the fatigue peak stress, i.e. from $E = 99.8\,\text{GPa}$ at the fatigue peak stress of $\sigma_{\max} = 200\,\text{MPa}$ to $E = 85.5\,\text{GPa}$ at the fatigue peak stress of $\sigma_{\max} = 400\,\text{MPa}$.

When the fiber volume is $V_f = 40\%$, the fatigue hysteresis dissipated energy increases with the fatigue peak stress, i.e. from $U = 5.8\,\text{kJ/m}^3$ at the fatigue peak stress of $\sigma_{\max} = 200\,\text{MPa}$ to $U = 62.9\,\text{kJ/m}^3$ at the fatigue peak stress of $\sigma_{\max} = 400\,\text{MPa}$; the fatigue hysteresis width increases with fatigue peak stress, i.e. from $\Delta\varepsilon = 0.004\%$ at the fatigue peak stress of $\sigma_{\max} = 200\,\text{MPa}$ to $\Delta\varepsilon = 0.023\%$ at the fatigue peak stress of $\sigma_{\max} = 400\,\text{MPa}$; and the fatigue hysteresis modulus decreases with the fatigue peak stress, i.e. from $E = 121.5\,\text{GPa}$ at the fatigue peak stress of $\sigma_{\max} = 200\,\text{MPa}$ to $E = 112.6\,\text{GPa}$ at the fatigue peak stress of $\sigma_{\max} = 400\,\text{MPa}$.

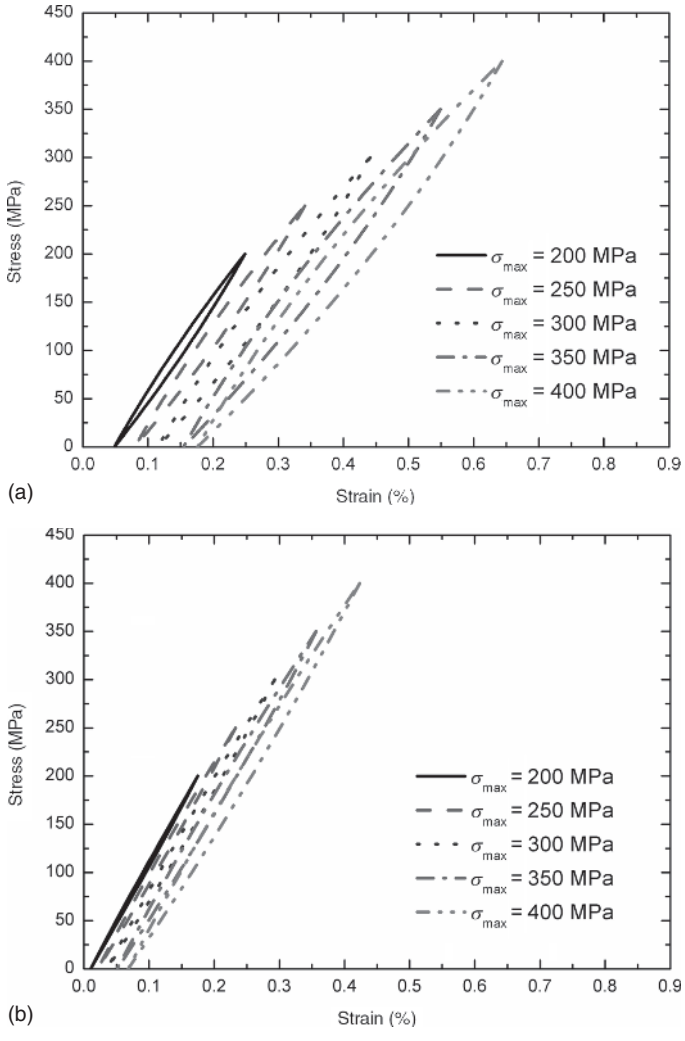

Figure 1.2 (a) The fatigue hysteresis loops at different fatigue peak stresses when the fiber volume fraction is $V_f = 30\%$; (b) the fatigue hysteresis loops at different fatigue peak stresses when the fiber volume fraction is $V_f = 40\%$; (c) the fatigue hysteresis dissipated energy for different fatigue peak stresses when the fiber volume fraction is $V_f = 30\%$ and 40%; (d) the fatigue hysteresis width for different fatigue peak stresses when the fiber volume fraction is $V_f = 30\%$ and 40%; and (e) the fatigue hysteresis modulus for different fatigue peak stresses when the fiber volume fraction is $V_f = 30\%$ and 40%.

When the fiber volume fraction increases, the fiber/matrix interface slip range inside of the matrix crack spacing decreases, i.e. the interface debonded length, interface counter slip, and new slip length decrease, leading to the decrease in the fatigue hysteresis dissipated energy and fatigue hysteresis width and the increase in the fatigue hysteresis modulus.

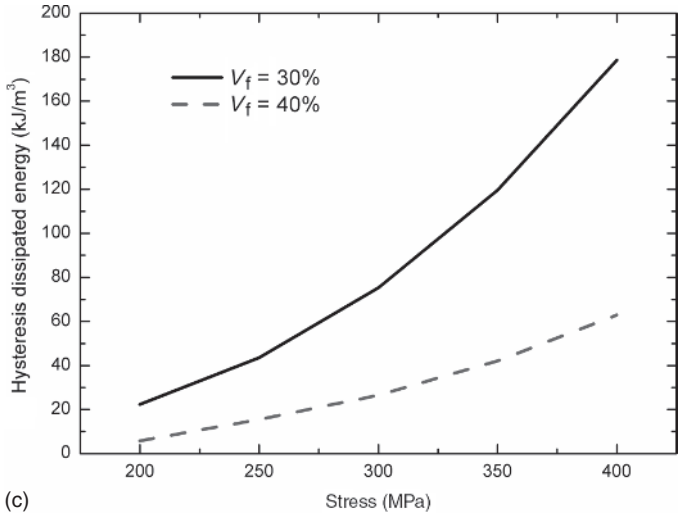

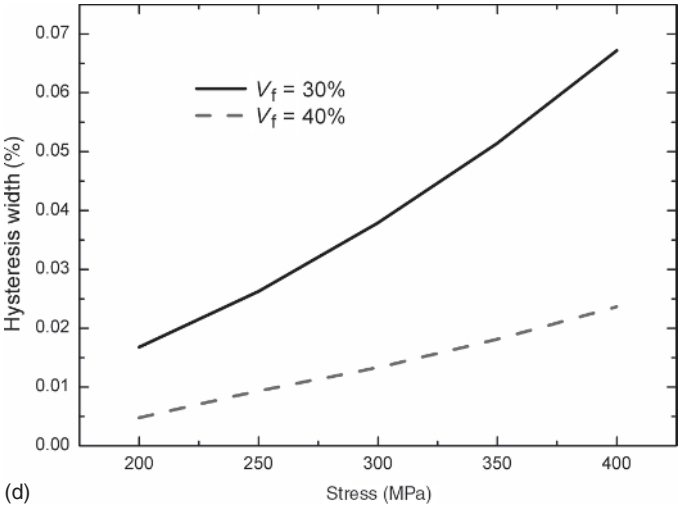

Figure 1.2 (*Continued*)

1.2.3.2 Effect of Matrix Cracking Density on Fatigue Hysteresis Loops and Fatigue Hysteresis-Based Damage Parameters

The matrix cracking density versus the applied stress curves for different saturation matrix crack spacing are shown in Figure 1.3a. When the saturation matrix crack spacing increases, the matrix cracking density decreases at the same applied stress. The fatigue hysteresis loops, fatigue hysteresis dissipated energy, fatigue hysteresis width, and fatigue hysteresis modulus for different matrix cracking densities are shown in Figure 1.3.

When the saturation matrix crack spacing is $l_{sat} = 140\,\mu m$, the fatigue hysteresis dissipated energy increases from $U = 8.3\,kJ/m^3$ at the fatigue peak stress of $\sigma_{max} = 200\,MPa$ to $U = 198.4\,kJ/m^3$ at the fatigue peak stress of $\sigma_{max} = 400\,MPa$;

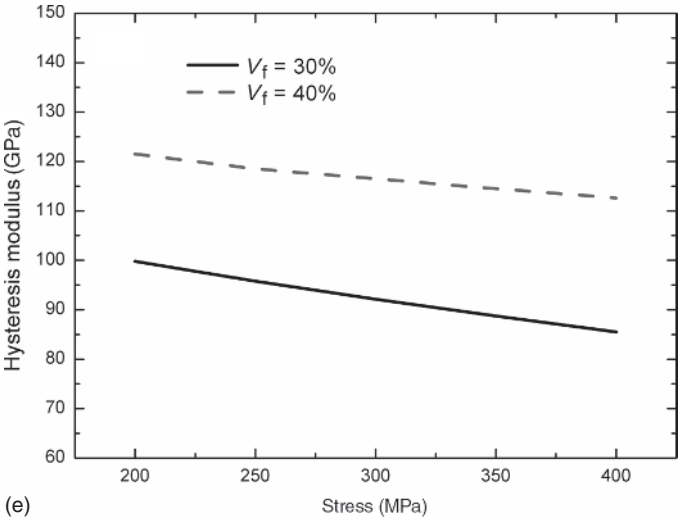

Figure 1.2 (*Continued*)

the fatigue hysteresis width increases from $\Delta\varepsilon = 0.006\%$ at the fatigue peak stress of $\sigma_{max} = 200$ MPa to $\Delta\varepsilon = 0.074\%$ at the fatigue peak stress of $\sigma_{max} = 400$ MPa; and the fatigue hysteresis modulus decreases from $E = 115$ GPa at the fatigue peak stress of $\sigma_{max} = 200$ MPa to $E = 84.7$ GPa at the fatigue peak stress of $\sigma_{max} = 400$ MPa.

When the saturation matrix crack spacing is $l_{sat} = 240$ μm, the fatigue hysteresis dissipated energy increases from $U = 4.8$ kJ/m^3 at the fatigue peak stress of $\sigma_{max} = 200$ MPa to $U = 115.7$ kJ/m^3 at the fatigue peak stress of $\sigma_{max} = 400$ MPa; the fatigue hysteresis width increases from $\Delta\varepsilon = 0.003\%$ at the fatigue peak stress of $\sigma_{max} = 200$ MPa to $\Delta\varepsilon = 0.043\%$ at the fatigue peak stress of $\sigma_{max} = 400$ MPa; and the fatigue hysteresis modulus decreases from $E = 118$ GPa at the fatigue peak stress of $\sigma_{max} = 200$ MPa to $E = 97.6$ GPa at the fatigue peak stress of $\sigma_{max} = 400$ MPa.

When the matrix cracking density increases and the matrix crack spacing decreases, the interface debonding and sliding extent inside of composite (i.e. $2l_d/l_c$, $2y/l_c$, and $2z/l_c$) increase, leading to the increase of the fatigue hysteresis dissipated energy and fatigue hysteresis width and the decrease of the fatigue hysteresis modulus.

1.2.3.3 Effect of Fiber/Matrix Interface Shear Stress on Fatigue Hysteresis Loops and Fatigue Hysteresis-Based Damage Parameters

The fatigue hysteresis loops, fatigue hysteresis dissipated energy, fatigue hysteresis width, and fatigue hysteresis modulus of SiC/CAS composite for different fiber/matrix interface shear stress are shown in Figure 1.4.

When the interface shear stress is $\tau_i = 10$ MPa, the fatigue hysteresis dissipated energy increases with the fatigue peak stress, i.e. from $U = 10.1$ kJ/m^3 at the fatigue peak stress of $\sigma_{max} = 200$ MPa to $U = 113.2$ kJ/m^3 at the fatigue peak stress

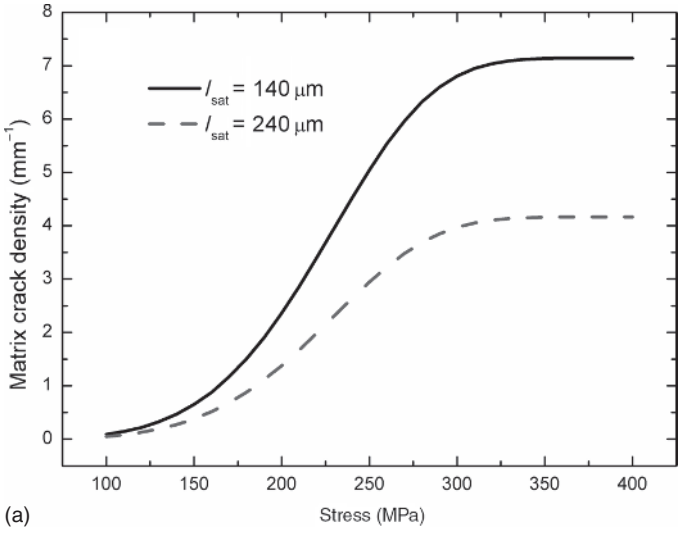

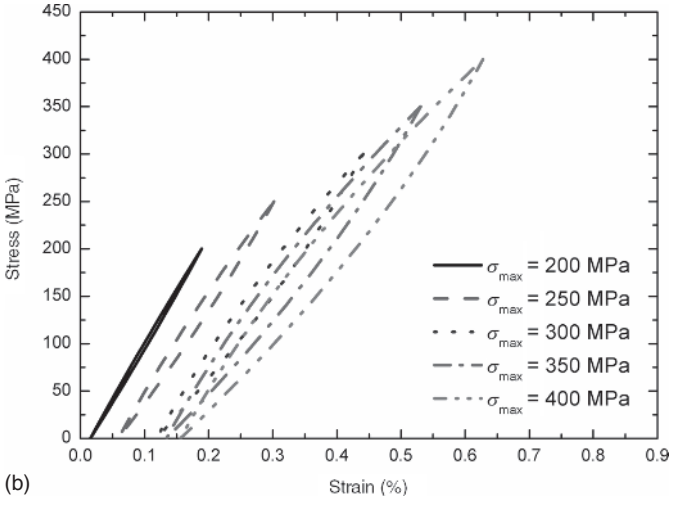

Figure 1.3 (a) The matrix cracking density versus the applied stress when the saturation matrix crack spacing is l_{sat} = 140 and 240 μm; (b) the fatigue hysteresis loops for different fatigue peak stresses when the saturation matrix crack spacing is l_{sat} = 140 μm; (c) the fatigue hysteresis loops for different fatigue peak stresses when the saturation matrix crack spacing is l_{sat} = 240 μm; (d) the fatigue hysteresis dissipated energy for different fatigue peak stresses when the saturation matrix crack spacing is l_{sat} = 140 and 240 μm; (e) the fatigue hysteresis width for different fatigue peak stresses when the saturation matrix crack spacing is l_{sat} = 140 and 240 μm; and (f) the fatigue hysteresis modulus for different fatigue peak stresses when the saturation matrix crack spacing is l_{sat} = 140 and 240 μm.

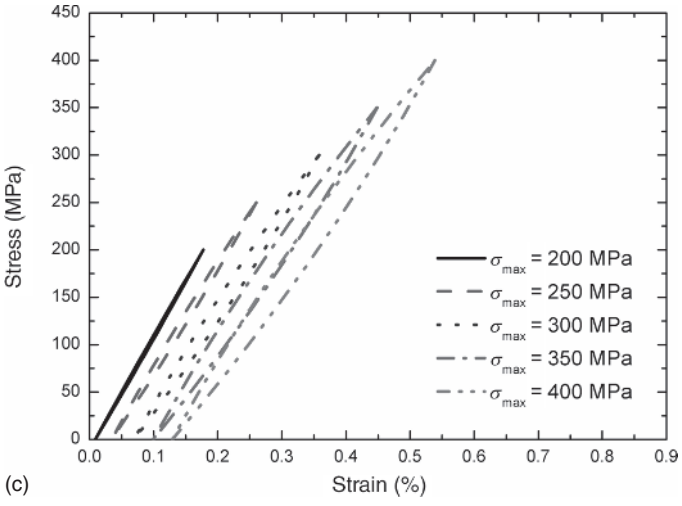

(c)

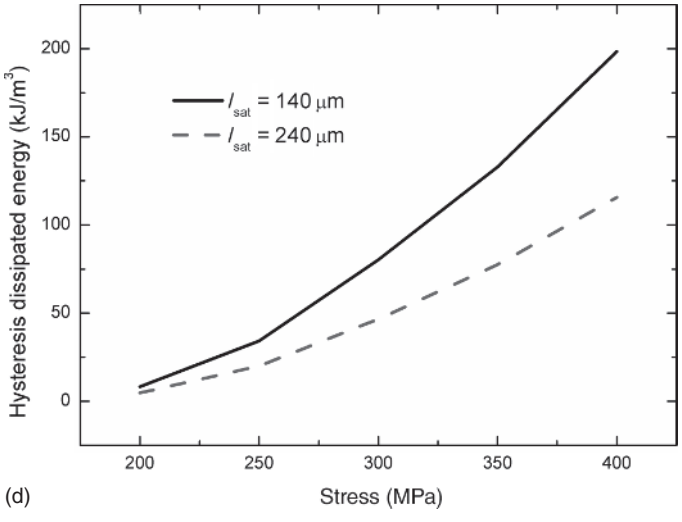

(d)

Figure 1.3 (*Continued*)

of $\sigma_{max} = 400$ MPa; the fatigue hysteresis width increases with fatigue peak stress, i.e. from $\Delta\varepsilon = 0.008\%$ at the fatigue peak stress of $\sigma_{max} = 200$ MPa to $\Delta\varepsilon = 0.042\%$ at the fatigue peak stress of $\sigma_{max} = 400$ MPa; and the hysteresis modulus decreases with the fatigue peak stress, from $E = 115.8$ GPa at the fatigue peak stress of $\sigma_{max} = 200$ MPa to $E = 101.8$ GPa at the fatigue peak stress of $\sigma_{max} = 400$ MPa.

When the interface shear stress is $\tau_i = 20$ MPa, the fatigue hysteresis dissipated energy increases with the fatigue peak stress, i.e. from $U = 5.5\,\text{kJ/m}^3$ at the fatigue peak stress of $\sigma_{max} = 200$ MPa to $U = 56.6\,\text{kJ/m}^3$ at the fatigue peak stress of $\sigma_{max} = 400$ MPa; the fatigue hysteresis width increases with fatigue

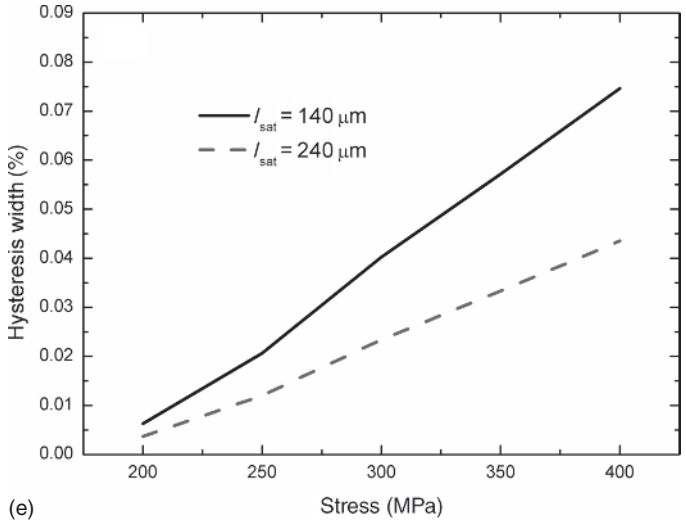

(e)

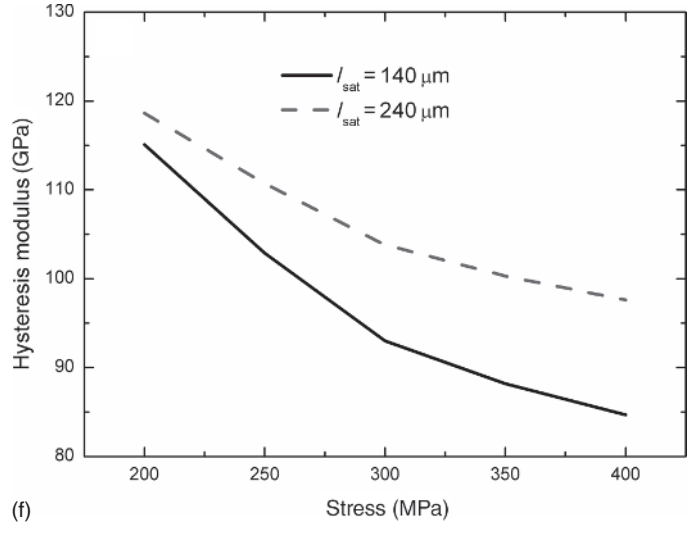

(f)

Figure 1.3 (*Continued*)

peak stress, i.e. from $\Delta\varepsilon = 0.004\%$ at the fatigue peak stress of $\sigma_{max} = 200$ MPa to $\Delta\varepsilon = 0.021\%$ at the fatigue peak stress of $\sigma_{max} = 400$ MPa; and the fatigue hysteresis modulus decreases with fatigue peak stress, i.e. from $E = 122.1$ GPa at the fatigue peak stress of $\sigma_{max} = 200$ MPa to $E = 114.2$ GPa at the fatigue peak stress of $\sigma_{max} = 400$ MPa.

When the fiber/matrix interface shear stress increases, the interface debonded length and interface slip length decrease, leading to the decrease in the fatigue hysteresis dissipated energy and fatigue hysteresis width and the increase in the fatigue hysteresis modulus.

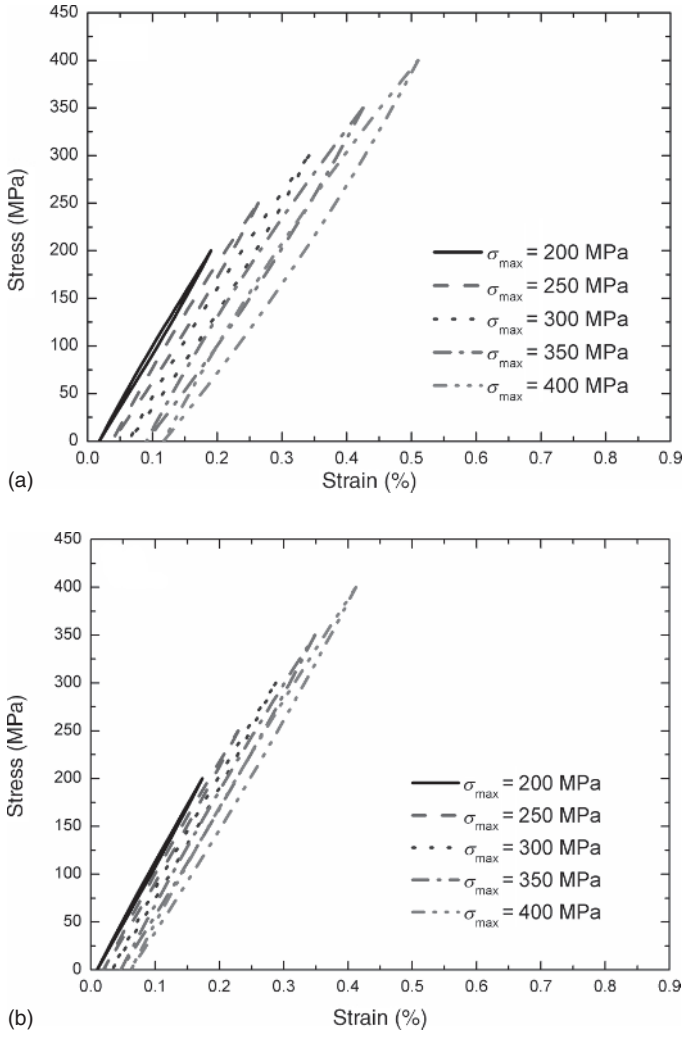

Figure 1.4 (a) The fatigue hysteresis loops at different fatigue peak stresses when the interface shear stress is $\tau_i = 10$ MPa; (b) the fatigue hysteresis loops at different fatigue peak stresses when the interface shear stress is $\tau_i = 20$ MPa; (c) the fatigue hysteresis dissipated energy at different fatigue peak stresses when the interface shear stress is $\tau_i = 10$ and 20 MPa; (d) the fatigue hysteresis width at different fatigue peak stresses when the interface shear stress is $\tau_i = 10$ and 20 MPa; and (e) the fatigue hysteresis modulus at different fatigue peak stresses when the interface shear stress is $\tau_i = 10$ and 20 MPa.

1.2.3.4 Effect of Fiber/Matrix Interface Debonded Energy on Fatigue Hysteresis Loops and Fatigue Hysteresis-Based Damage Parameters

The fatigue hysteresis loops, fatigue hysteresis dissipated energy, fatigue hysteresis width, and fatigue hysteresis modulus of SiC/CAS composite are shown in Figure 1.5 for different interface debonded energies.

When the interface debonded energy is $\xi_d = 0.1\,\mathrm{J/m^2}$, the fatigue hysteresis dissipated energy increases with the fatigue peak stress, i.e. from $U = 9.4\,\mathrm{kJ/m^3}$ at

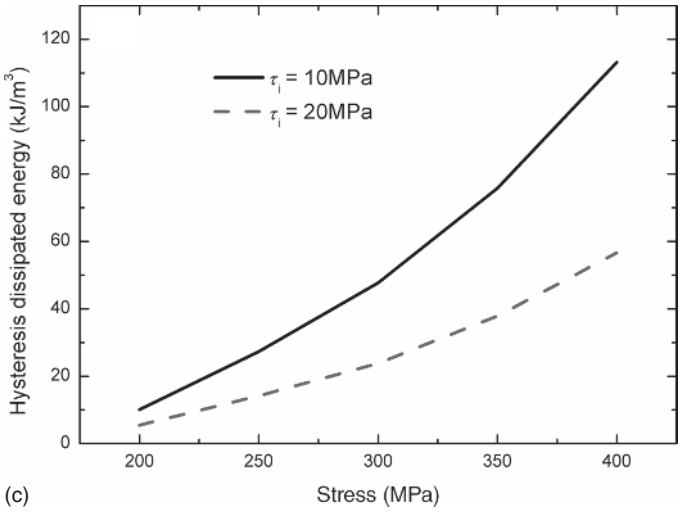

(c)

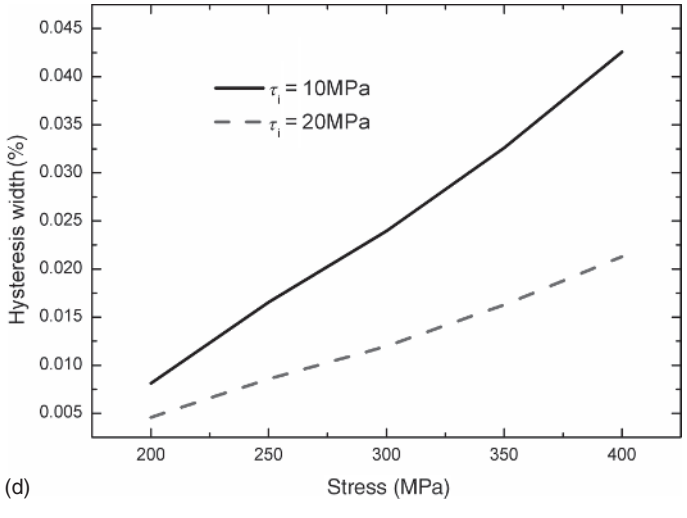

(d)

Figure 1.4 (*Continued*)

the fatigue peak stress of $\sigma_{max} = 200$ MPa to $U = 75.4$ kJ/m^3 at the fatigue peak stress of $\sigma_{max} = 400$ MPa; the fatigue hysteresis width increases with the fatigue peak stress, i.e., from $\Delta\varepsilon = 0.007\%$ at the fatigue peak stress of $\sigma_{max} = 200$ MPa to $\Delta\varepsilon = 0.028\%$ at the fatigue peak stress of $\sigma_{max} = 400$ MPa; and the fatigue hysteresis modulus decreases with the fatigue peak stress, i.e. from $E = 119$ GPa at the fatigue peak stress of $\sigma_{max} = 200$ MPa to $E = 109.7$ GPa at the fatigue peak stress of $\sigma_{max} = 400$ MPa.

When the interface debonded energy is $\xi_d = 1.0$ J/m^2, the fatigue hysteresis dissipated energy increases with the fatigue peak stress, i.e. from $U = 8.2$ kJ/m^3 at the fatigue peak stress of $\sigma_{max} = 250$ MPa to $U = 75.9$ kJ/m^3 at the fatigue peak stress of $\sigma_{max} = 400$ MPa; the fatigue hysteresis width increases with the fatigue

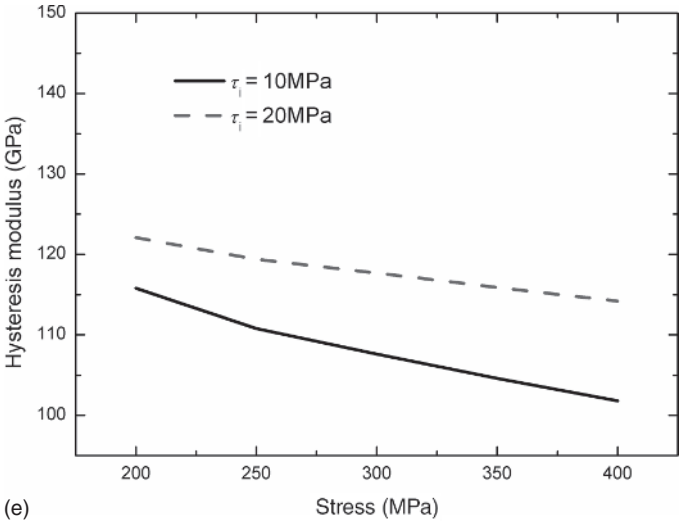

Figure 1.4 (*Continued*)

peak stress, i.e. from $\Delta\varepsilon = 0.004\%$ at the fatigue peak stress of $\sigma_{max} = 250$ MPa to $\Delta\varepsilon = 0.028\%$ at the fatigue peak stress of $\sigma_{max} = 400$ MPa; and the fatigue hysteresis modulus decreases with the fatigue peak stress, i.e. from $E = 126.9$ GPa at the fatigue peak stress of $\sigma_{max} = 200$ MPa to $E = 109.7$ GPa at the fatigue peak stress of $\sigma_{max} = 400$ MPa.

When the fiber/matrix interface debonded energy increases, the interface debonded length and interface slip length decrease, leading to the decrease of the fatigue hysteresis dissipated energy and fatigue hysteresis width and the increase of the fatigue hysteresis modulus.

1.2.3.5 Effect of Fiber Failure on Fatigue Hysteresis Loops and Fatigue Hysteresis-Based Damage Parameters

Under cyclic loading/unloading, broken fiber occurs with increasing applied stress, as shown in Figure 1.6a. The fatigue hysteresis loops, fatigue hysteresis dissipated energy, fatigue hysteresis width, and fatigue hysteresis modulus with and without considering fiber failure are shown in Figure 1.6.

When the fiber failure is not considered, the fatigue hysteresis dissipated energy increases from $U = 31.8\,kJ/m^3$ at the fatigue peak stress of $\sigma_{max} = 300$ MPa to $U = 75.4\,kJ/m^3$ at the fatigue peak stress of $\sigma_{max} = 400$ MPa; the fatigue hysteresis width increases from $\Delta\varepsilon = 0.015\%$ at the fatigue peak stress of $\sigma_{max} = 300$ MPa to $\Delta\varepsilon = 0.028\%$ at the fatigue peak stress of $\sigma_{max} = 400$ MPa; and the fatigue hysteresis modulus decreases from $E = 114.1$ GPa at the fatigue peak stress of $\sigma_{max} = 300$ MPa to $E = 109.7$ GPa at the fatigue peak stress of $\sigma_{max} = 400$ MPa.

When the fiber failure is considered, the fatigue hysteresis dissipated energy increases from $U = 34.8\,kJ/m^3$ at the fatigue peak stress of $\sigma_{max} = 300$ MPa to $U = 115.6\,kJ/m^3$ at the fatigue peak stress of $\sigma_{max} = 400$ MPa; the fatigue hysteresis width increases from $\Delta\varepsilon = 0.017\%$ at the fatigue peak stress of $\sigma_{max} = 300$ MPa to $\Delta\varepsilon = 0.043\%$ at the fatigue peak stress of $\sigma_{max} = 400$ MPa; and the fatigue

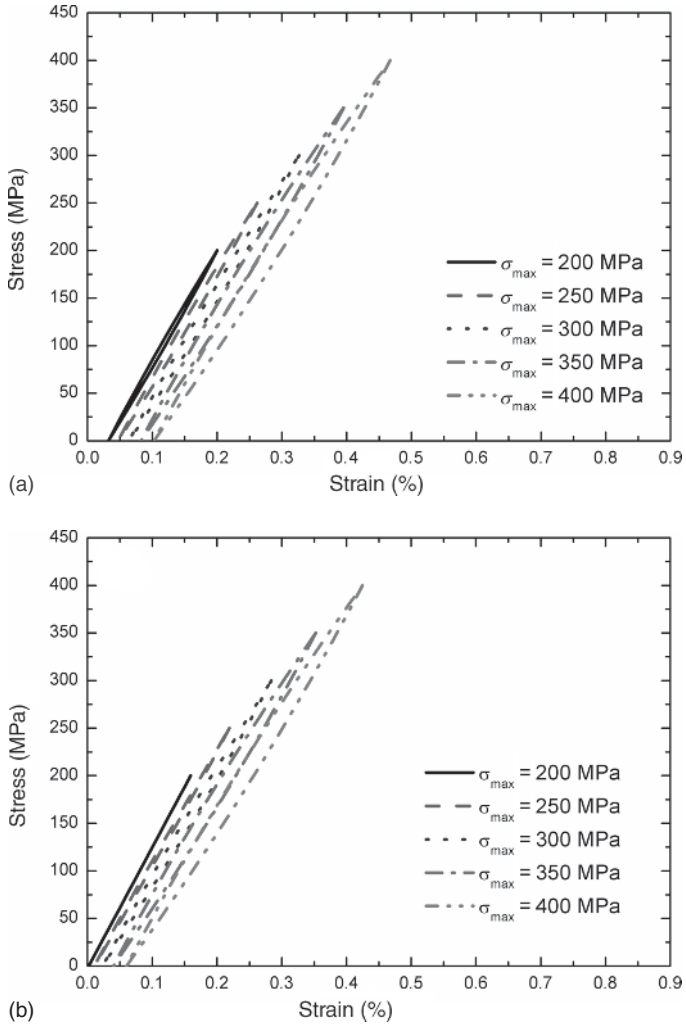

Figure 1.5 (a) The fatigue hysteresis loops at different fatigue peak stresses when the interface debonded energy is $\xi_d = 0.1$ J/m^2; (b) the fatigue hysteresis loops at different fatigue peak stresses when the interface debonded energy is $\xi_d = 1.0$ J/m^2; (c) the fatigue hysteresis dissipated energy at different fatigue peak stresses when the interface debonded energy is $\xi_d = 0.1$ and 1.0 J/m^2; (d) the fatigue hysteresis width at different fatigue peak stresses when the interface debonded energy is $\xi_d = 0.1$ and 1.0 J/m^2; and (e) the fatigue hysteresis modulus at different fatigue peak stresses when the interface debonded energy is $\xi_d = 0.1$ and 1.0 J/m^2.

hysteresis modulus decreases from $E = 113.7$ GPa at the fatigue peak stress of $\sigma_{max} = 300$ MPa to $E = 107.2$ GPa at the fatigue peak stress of $\sigma_{max} = 400$ MPa.

When the fiber failure is considered, the interface debonded length and interface slip length increase inside of the composite, leading to the increase of the fatigue hysteresis dissipated energy and fatigue hysteresis width and decrease of the fatigue hysteresis modulus.

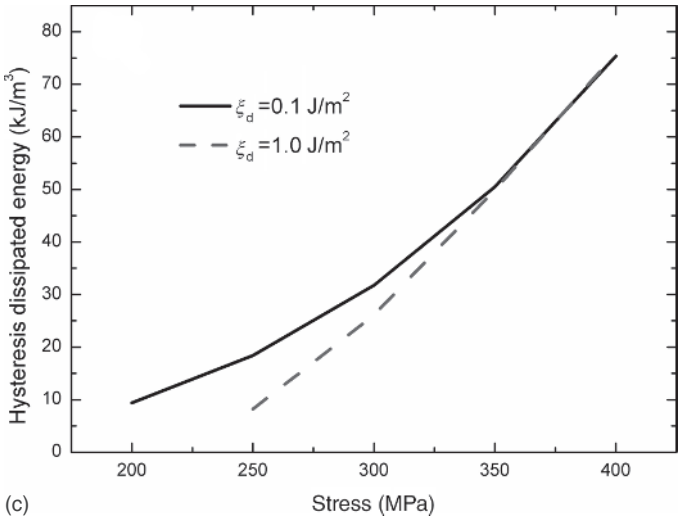

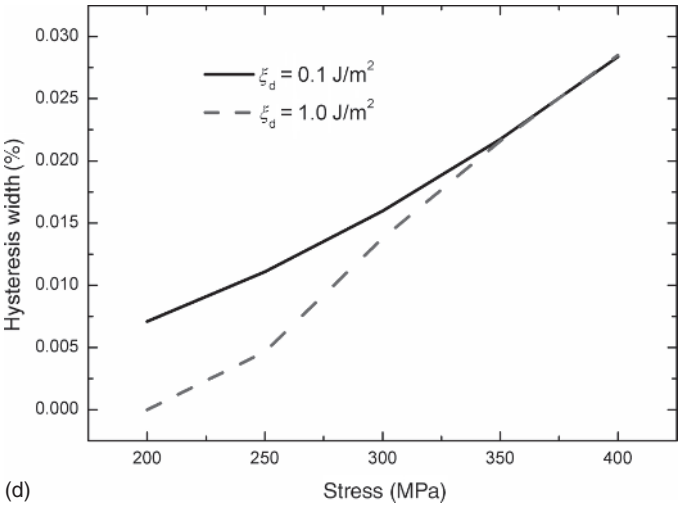

Figure 1.5 (*Continued*)

1.2.4 Experimental Comparisons

The cyclic loading/unloading tensile hysteresis loops of unidirectional C/SiC, C/Si_3N_4, SiC/Si_3N_4, SiC/CAS, and SiC/SiC composites are predicted.

1.2.4.1 C/SiC Composite

The cyclic loading/unloading tensile stress–strain curve of unidirectional C/SiC composite at room temperature is shown in Figure 1.7. The specimen was unloading and subsequent reloading at different peak stresses and failed at the stress of 265 MPa and the failure strain of 0.27%.

As there is a large mismatch of the axial thermal expansion coefficients between the carbon fibers and silicon carbide matrix, there are unavoidable

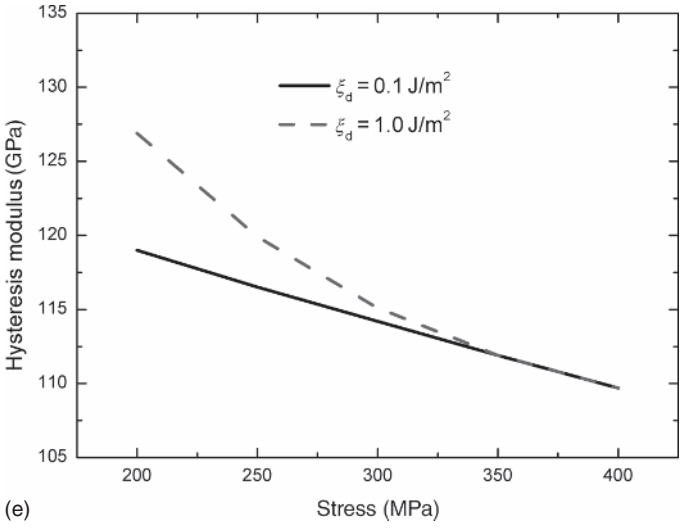

Figure 1.5 (*Continued*)

microcracks existed within the SiC matrix when the composites are cooled down from high process temperature to room temperature. These processing-induced microcracks propagated in conjunction with new microcracks during the process of loading/unloading. These microcracks joined together to form macrocracks, and some microcracks deflect along fiber/matrix interface, leading to the stress–strain hysteresis loops during unloading and subsequent reloading. The multiple matrix cracks on the side surface and fiber pullout at the fracture surface of the tensile failed specimen are shown in Figure 1.8. The material exhibited multiple matrix cracking and fiber pullout during tensile failure with distributed fiber failure.

The fiber/matrix interface shear stress can be estimated by the multiple fracture method using the average matrix crack spacing at saturation l_{sat} and given by the following equation (Curtin 1993):

$$\tau_i = 1.34\left[\frac{\xi_m r_f^2 E_m E_f V_m^2}{E_c V_f l_{sat}^3}\right]^{1/2} \tag{1.48}$$

where ξ_m denotes the matrix fracture energy and l_{sat} measured by optical microscope is 124 μm. The calculated τ_i value for unidirectional C/SiC with PyC/SiC interface phase is 5.7 MPa.

In the matrix statistics cracking model, the matrix cracking characteristic stress σ_R is derived as the Aveston–Cooper–Kelly (ACK) steady matrix cracking stress (Aveston et al. 1971):

$$\sigma_{cr}^{ACK} = \left(\frac{6V_f^2 E_f E_c^2 \tau_i \xi_m}{r_f V_m E_m^2}\right)^{1/3} - E_c(\alpha_c - \alpha_m)\Delta T \tag{1.49}$$

The matrix characteristic strength can be derived by Eq. (1.49) and given by $\sigma_R = 110$ MPa. The experimental and theoretical matrix cracking density versus

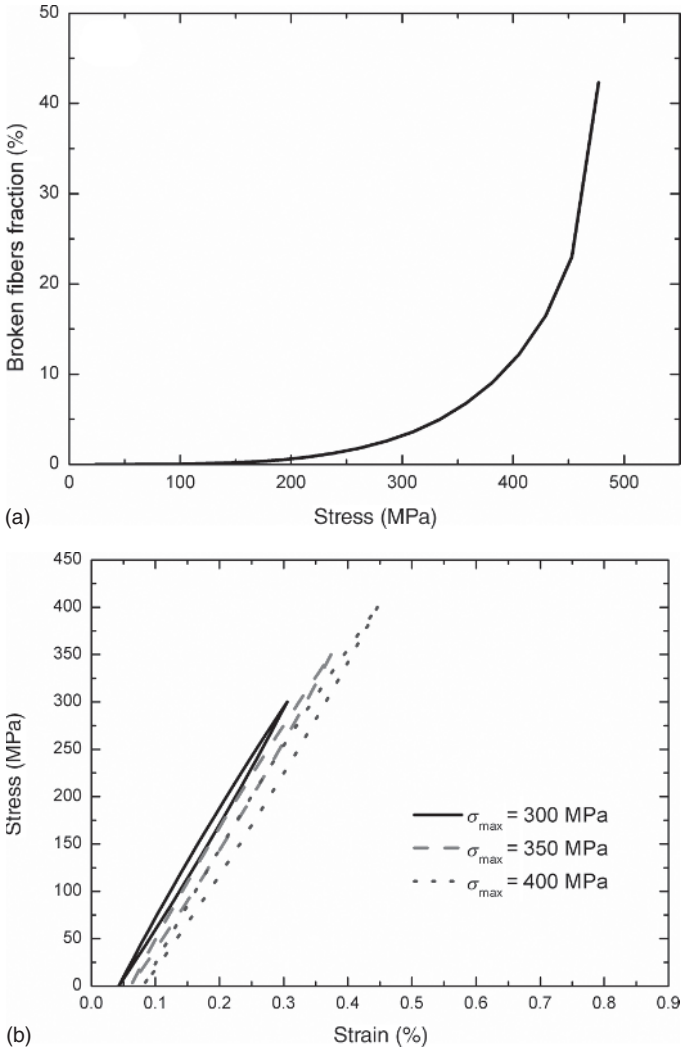

Figure 1.6 (a) The broken fibers fraction versus applied stress curve; (b) the fatigue hysteresis loops at different fatigue peak stresses without fiber failure; (c) the fatigue hysteresis loops at different fatigue peak stresses with fiber failure; (d) the fatigue hysteresis dissipated energy at different fatigue peak stresses with and without fiber failure; (e) the fatigue hysteresis width at different fatigue peak stresses with and without fiber failure; and (f) the fatigue hysteresis modulus at different fatigue peak stresses with and without fiber failure.

applied stress curves are shown in Figure 1.9, in which the matrix Weibull modulus m is given by 3. The matrix cracking density kept increasing as the applied stress increased and saturated at about 180–200 MPa.

Submitting σ_c = 4.9 GPa and m_f = 5 into Eq. (1.27), the predicted tensile strength of unidirectional C/SiC is 1431 MPa, which is much higher than experimentally observed tensile strength of 265 MPa. Curtin (1994) evaluated the *in situ* strength of fibers in ceramic composites using the fracture mirror

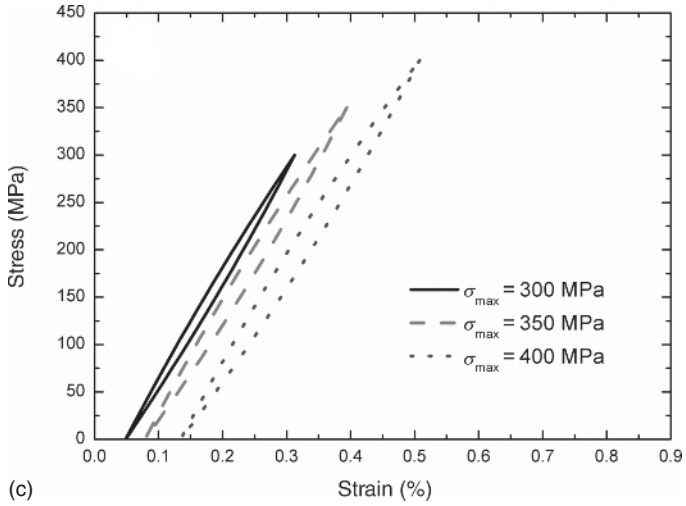

(c)

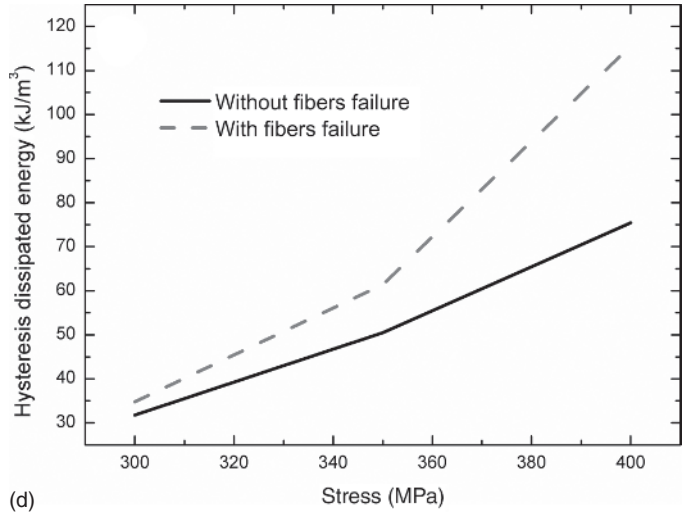

(d)

Figure 1.6 (*Continued*)

method. It was found that the fiber *in situ* strength was far lower than the original fiber strength. However, the fiber Weibull modulus remained unchanged. In the present analysis, the fiber strength (σ_c = 891 MPa) was calculated from the experimental tensile strength σ_{UTS} (265 MPa).

The experimental and theoretical fatigue hysteresis loops of unidirectional C/SiC composite with and without considering fiber failure when the fatigue peak stress is σ_{max} = 160 MPa are shown in Figure 1.10a. Under the fatigue peak stress of σ_{max} = 160 MPa, the interface partially debonds and the fiber failure volume is 0.62%. The peak and valley strains considering fiber failure are larger than those without considering fiber failure. The interface sliding ratio versus the applied stress curves with and without considering fiber failure are shown

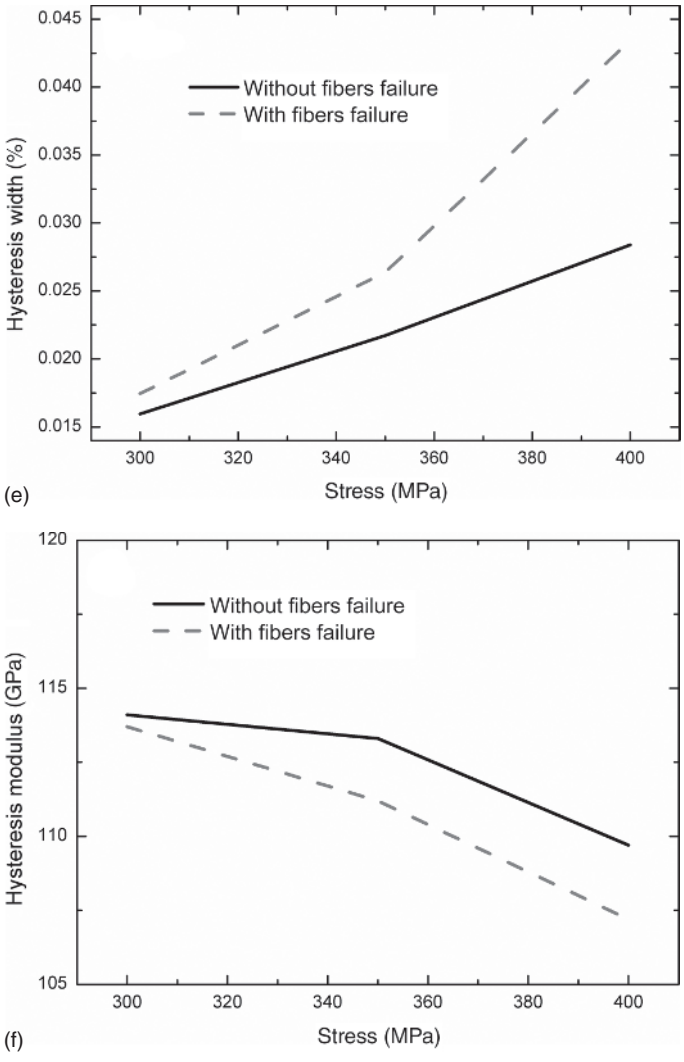

Figure 1.6 (*Continued*)

in Figure 1.10b. The unloading interface counter slip length increases with the decrease of the applied stress, and at the valley stress, the interface counter slip length is less than the interface debonded length of $y(\sigma_{\min}) < l_d$. The reloading interface new slip length increases with the increase in the applied stress, and at the peak stress, the interface new slip length is less than the interface debonded length of $z(\sigma_{\max}) < l_d$. The interface slip lengths upon unloading and reloading considering fiber failure are both larger than those without considering fiber failure. The fatigue hysteresis loops under the fatigue peak stress of $\sigma_{\max} = 160$ MPa correspond to the interface slip Case 2, i.e. the interface partially debonding and the fiber sliding partially in the interface debonded region.

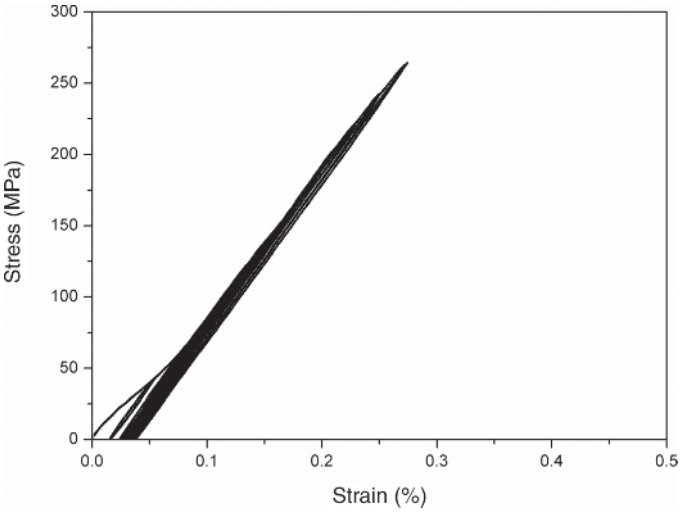

Figure 1.7 The cyclic loading/unloading tensile stress–strain curve of unidirectional C/SiC composite at room temperature.

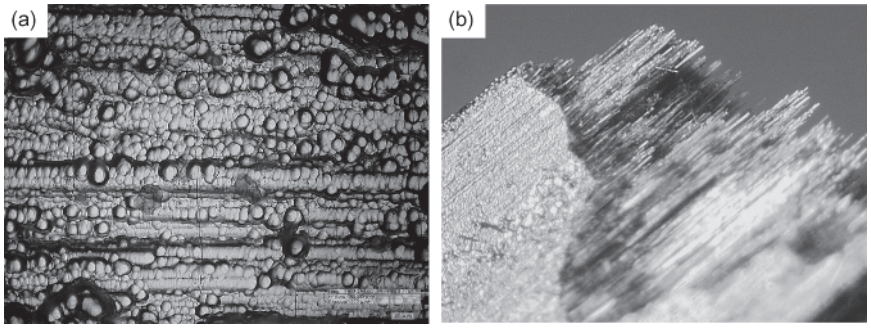

Figure 1.8 (a) The matrix multiple cracking on the side surface; and (b) the fiber pullout at the fracture surface for the failed tensile specimen of C/SiC composite. Source: Li et al. (2013). Reproduced with permission of Elsevier.

The experimental and theoretical predicted fatigue hysteresis loops of unidirectional C/SiC composite with and without considering fiber failure when the fatigue peak stress is $\sigma_{max} = 220$ MPa are shown in Figure 1.11a. Under the fatigue peak stress of $\sigma_{max} = 220$ MPa, the interface partially debonds and the fiber failure volume is 4.6%. The fatigue hysteresis loops under the fatigue peak stress of $\sigma_{max} = 220$ MPa correspond to the interface partially debonding and the fiber sliding partially relative to matrix in the interface debonded region. The interface slip lengths versus the applied stress with and without considering fiber failure are shown in Figure 1.11b. The interface counter slip length at the valley stress is less than the interface debonded length of $y(\sigma_{min}) < l_d$; and the interface new slip length at the peak stress is less than the interface debonded length of $z(\sigma_{max}) < l_d$. The interface slip lengths considering the fiber failure are larger than those without considering fiber failure.

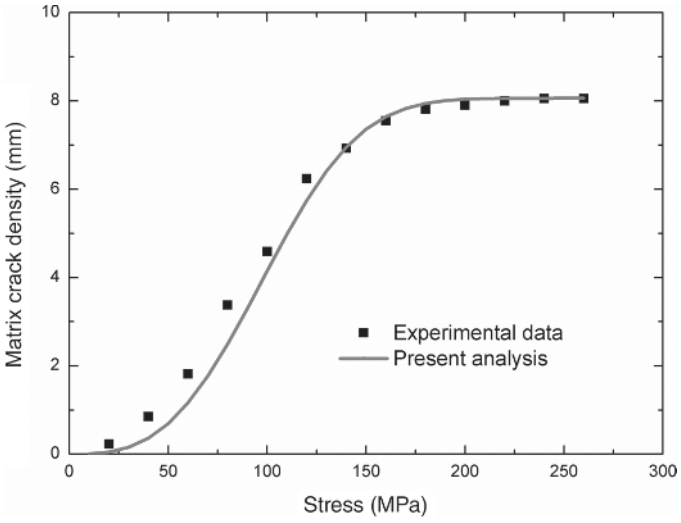

Figure 1.9 The experimental and theoretical matrix cracking density versus applied stress curves of C/SiC composite.

The experimental and theoretical hysteresis loops of unidirectional C/SiC composite with and without considering fiber failure when the fatigue peak stress is $\sigma_{max} = 260$ MPa are shown in Figure 1.12a. The interface completely debonds and the fiber failure volume is 18.7%. The fatigue hysteresis loops under the fatigue peak stress of $\sigma_{max} = 260$ MPa correspond to the interface completely debonding and the fiber sliding partially relative to matrix in the interface debonded region. The interface slip lengths versus the applied stress curves with and without considering fiber failure are shown in Figure 1.12b. The interface counter slip length at the valley stress is less than the matrix crack spacing of $y(\sigma_{min}) < l_c/2$; and the interface new slip length at the peak stress is less than the matrix crack spacing of $z(\sigma_{max}) < l_c/2$. The interface slip lengths considering fiber failure are larger than those without considering fiber failure.

1.2.4.2 C/Si_3N_4 Composite

The cyclic loading/unloading tensile curves of unidirectional C/Si_3N_4 composite at room temperature are shown in Figure 1.13a. The composite was unloading and subsequent reloading at different peak stresses of $\sigma_{max} = 117$, 122, 125, 142, 196, and 269 MPa and failed at the stress of $\sigma_{UTS} = 389$ MPa with the failure strain of $\varepsilon_f = 0.9\%$. The experimental fatigue hysteresis dissipated energy versus the peak stress curve is shown in Figure 1.13b. The fatigue hysteresis dissipated energy increases with the fatigue peak stress, i.e. from $U = 4.7$ kJ/m^3 at the fatigue peak stress of $\sigma_{max} = 117$ MPa to $U = 81.7$ kJ/m^3 at the fatigue peak stress of $\sigma_{max} = 269$ MPa. The experimental matrix cracking density versus the applied stress curve is shown in Figure 1.13c. The matrix cracking density increases with the applied stress, from the first matrix cracking stress of $\sigma_{mc} = 90$ MPa to the saturation matrix cracking stress of $\sigma_{sat} = 200$ MPa, with the saturation matrix crack spacing of $l_{sat} = 165$ μm.

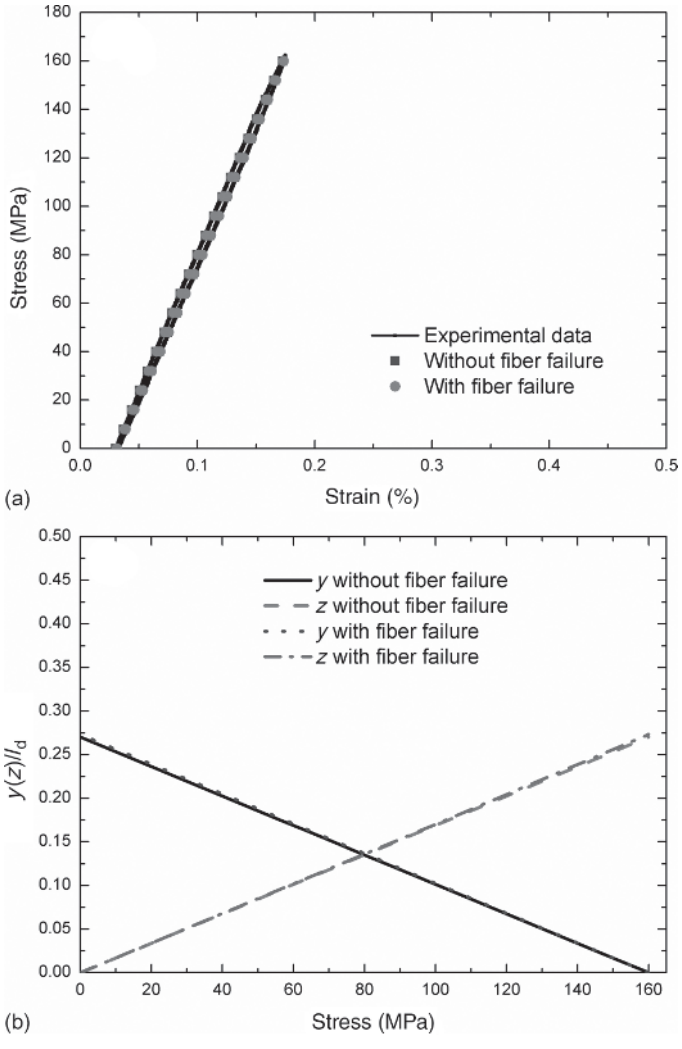

Figure 1.10 (a) The fatigue hysteresis loops; and (b) the interface slip lengths versus the applied stress of unidirectional C/SiC composite under the fatigue peak stress of $\sigma_{max} = 160$ MPa.

The experimental and theoretical predicted fatigue hysteresis loops and interface slip lengths versus the applied stress curves are shown in Figures 1.14–1.19. When the fatigue peak stress is $\sigma_{max} = 117$, 122, 125, 142, and 196 MPa, the interface partially debonding of $2l_d/l_c < 1$ and the fiber sliding partially relative to the matrix in the interface debonded region of $y/l_d < 1$. With increasing the fatigue peak stress from $\sigma_{max} = 117$ MPa to $\sigma_{max} = 196$ MPa, the interface counter slip length at the valley stress and the interface new slip length at the peak stress decrease from $y/l_d = 0.96$ at the fatigue peak stress of $\sigma_{max} = 117$ MPa to $y/l_d = 0.7$ at the fatigue peak stress of $\sigma_{max} = 196$ MPa. The fatigue hysteresis loops at the fatigue peak stresses of $\sigma_{max} = 117$, 122, 125, 142, and 196 MPa correspond to the

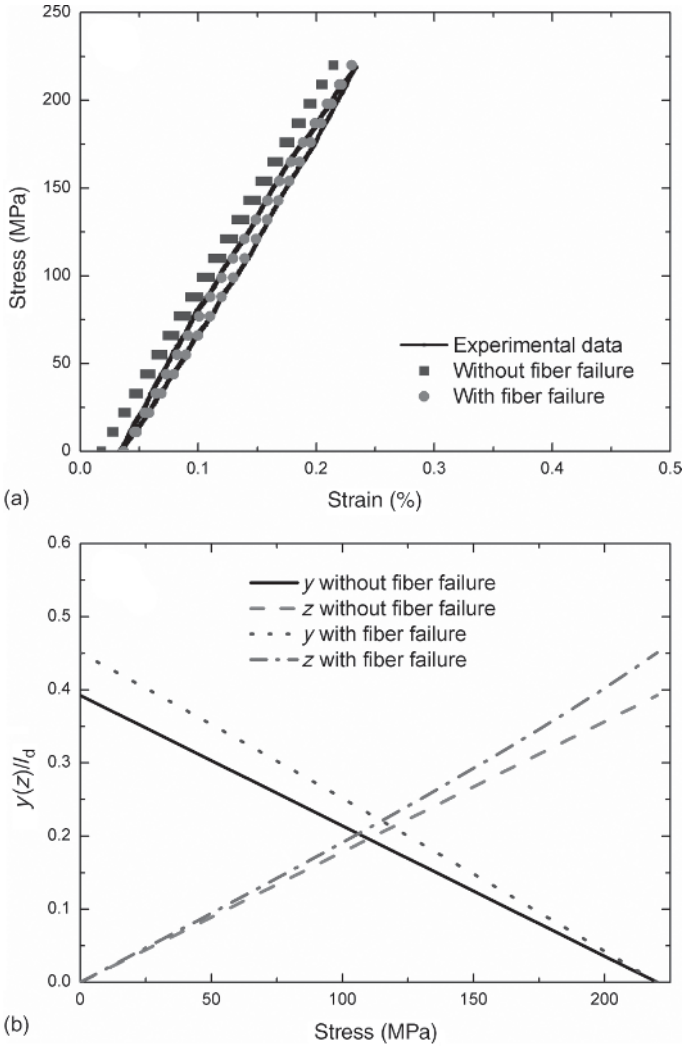

Figure 1.11 (a) The fatigue hysteresis loops; and (b) the fiber/matrix interface slip lengths versus the applied stress of C/SiC composite under the fatigue peak stress of $\sigma_{max} = 220$ MPa.

interface partially debonding and the fiber sliding partially relative to matrix in the interface debonded region. When the fatigue peak stress is $\sigma_{max} = 269$ MPa, the interface completely debonds of $2l_d/l_c = 1$, and the fiber partially slides relative to the matrix in the interface debonded region of $y/l_d < 1$. Upon completely unloading, the interface counter slip length occupies 74% of the matrix crack spacing of $2y/l_c = 74\%$. The fatigue hysteresis loops correspond to the interface slip Case 3, i.e. the interface completely debonding and the fiber sliding partially relative to matrix in the interface debonded region.

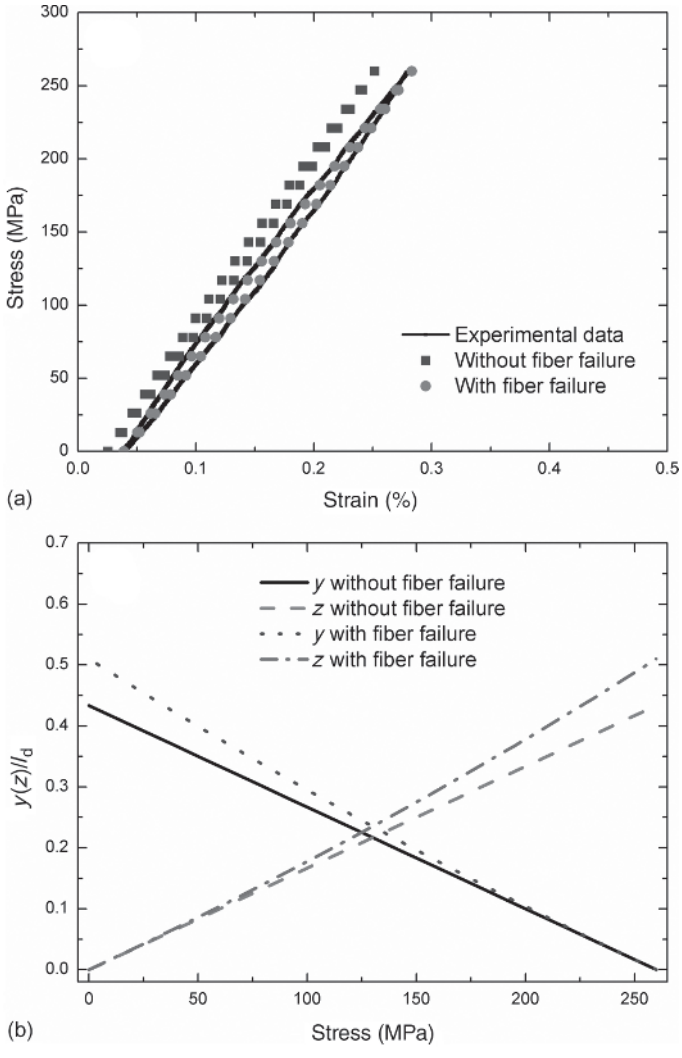

Figure 1.12 (a) The fatigue hysteresis loops; (b) the interface slip lengths versus the applied stress under the fatigue peak stress of $\sigma_{max} = 260$ MPa.

1.2.4.3 SiC/Si_3N_4 Composite

The cyclic loading/unloading tensile curves of type A SiC/Si_3N_4 with the strong interface bonding at room temperature are shown in Figure 1.20a. The composite was unloading and subsequent reloading at the fatigue peak stresses of σ_{max} = 380, 416, 456, 473, 485, 497, 525, 534, 558, 594, and 625 MPa and failed at $\sigma_{UTS} = 630$ MPa with the failure strain of $\varepsilon_f = 0.55\%$. The experimental fatigue hysteresis dissipated energy versus the fatigue peak stress curve is shown in Figure 1.20b. The fatigue hysteresis dissipated energy increases from $U = 9.5\,kJ/m^3$ at the fatigue peak stress of $\sigma_{max} = 381$ MPa to $U = 192.8\,kJ/m^3$ at the fatigue peak stress of $\sigma_{max} = 625$ MPa. The experimental matrix cracking

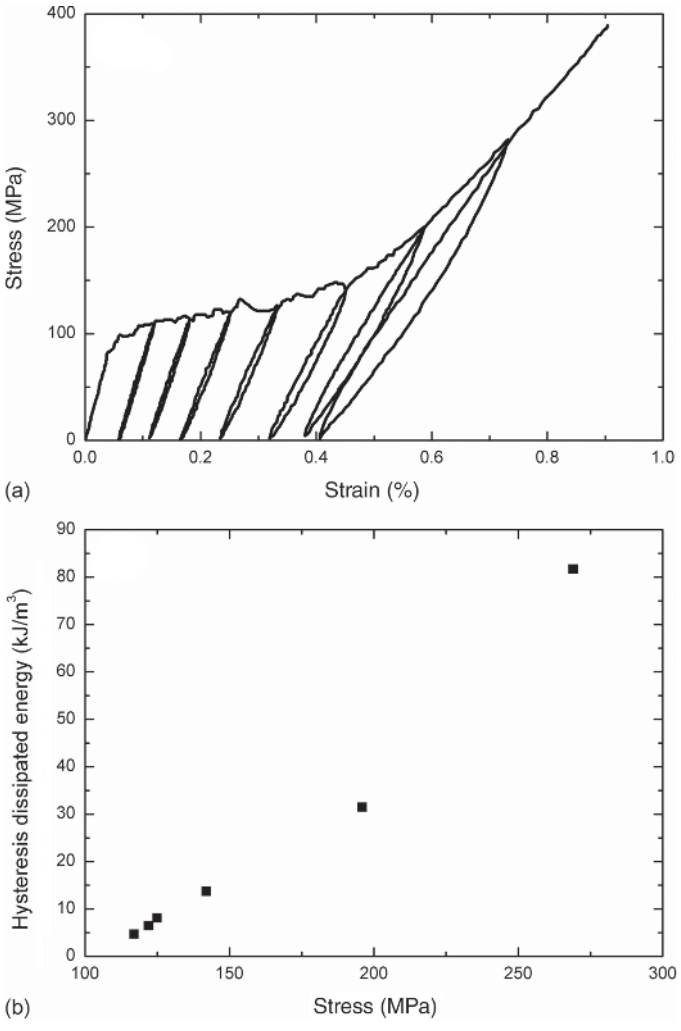

Figure 1.13 (a) The cyclic loading/unloading stress–strain curves; (b) the fatigue hysteresis dissipated energy versus the applied stress curve; and (c) the matrix cracking density versus the applied stress curve of unidirectional C/Si_3N_4 composite.

density versus the applied stress curve is shown in Figure 1.20c. The matrix cracking density increases from the first matrix cracking stress of $\sigma_{mc} = 350$ MPa to the saturation matrix cracking stress of $\sigma_{sat} = 550$ MPa with the saturation matrix crack spacing of $l_{sat} = 143$ μm.

The experimental and predicted fatigue hysteresis loops and the interface slip lengths at the fatigue peak stresses of $\sigma_{max} = 485$, 525, and 625 MPa are shown in Figures 1.21–1.23. When the fatigue peak stress is $\sigma_{max} = 485$ MPa, the interface partially debonds of $2l_d/l_c < 1$; the interface counter slip length approaches to the interface debonded length at the transition stress of $\sigma_{tr\_pu} = 145$ MPa of

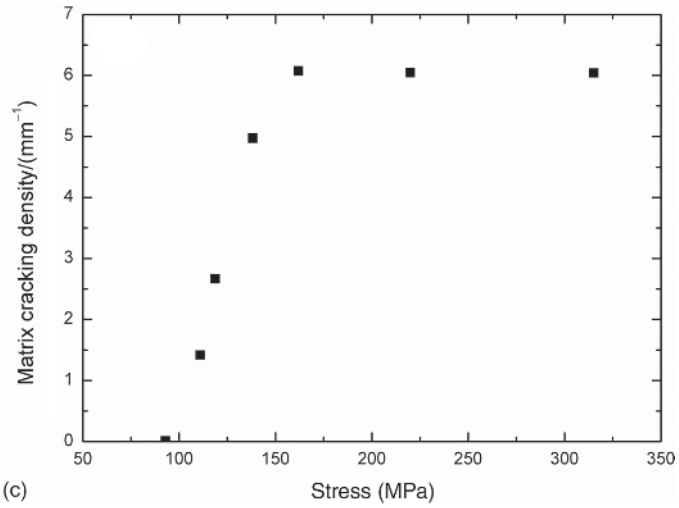

Figure 1.13 (*Continued*)

$y(\sigma_{tr\_pu})/l_d = 1$; and the interface new slip length approaches to the interface debonded length at the transition stress of $\sigma_{tr\_pr} = 340$ MPa of $z(\sigma_{tr\_pr})/l_d = 1$.

When the fatigue peak stress is $\sigma_{max} = 525$ MPa, the interface partially debonds of $2l_d/l_c < 1$; the interface counter slip length approaches to the interface debonded length at the transition stress of $\sigma_{tr\_pu} = 105$ MPa of $y(\sigma_{tr\_pu})/l_d = 1$; and the interface new slip length approaches to the interface debonded length at the transition stress of $\sigma_{tr\_pr} = 425$ MPa of $z(\sigma_{tr\_pr})/l_d = 1$.

When the fatigue peak stress is $\sigma_{max} = 625$ MPa, the interface partially debonds of $2l_d/l_c < 1$; the interface counter slip length approaches to the interface debonded length at the transition stress of $\sigma_{tr\_pu} = 0$ MPa of $y(\sigma_{tr\_pu})/l_d = 1$; and the interface new slip length approaches to the interface debonded length at the transition stress of $\sigma_{tr\_pr} = 625$ MPa of $z(\sigma_{tr\_pr})/l_d = 1$.

The fatigue hysteresis loops at the fatigue peak stress of $\sigma_{max} = 485$, 525, and 625 MPa correspond to the interface partially debonds and the fiber sliding completely relative to the matrix in the interface debonded region. With the increase of the fatigue peak stress, the unloading transition stress decreases, and the reloading transition stress increases under cyclic loading/unloading tensile.

The cyclic loading/unloading tensile curves of type B SiC/Si_3N_4 with the weak interface bonding at room temperature are shown in Figure 1.24a. The composite was unloading and subsequent reloading at the fatigue peak stresses of $\sigma_{max} = 430$, 460, 470, 495, 500, 510, 520, 555, and 610 MPa and failed at the stress of $\sigma_{UTS} = 637$ MPa with the failure strain of $\varepsilon_f = 0.75\%$. The experimental fatigue hysteresis dissipated energy versus the peak stress curve is shown in Figure 1.24b. The fatigue hysteresis dissipated energy increases from $U = 1.6$ kJ/m^3 at the fatigue peak stress of $\sigma_{max} = 430$ MPa to $U = 672.1$ kJ/m^3 at the fatigue peak stress of $\sigma_{max} = 610$ MPa. The experimental matrix crack density versus the applied stress curve is shown in Figure 1.24c. The matrix cracking density increases from the first matrix cracking stress of $\sigma_{mc} = 400$ MPa to the

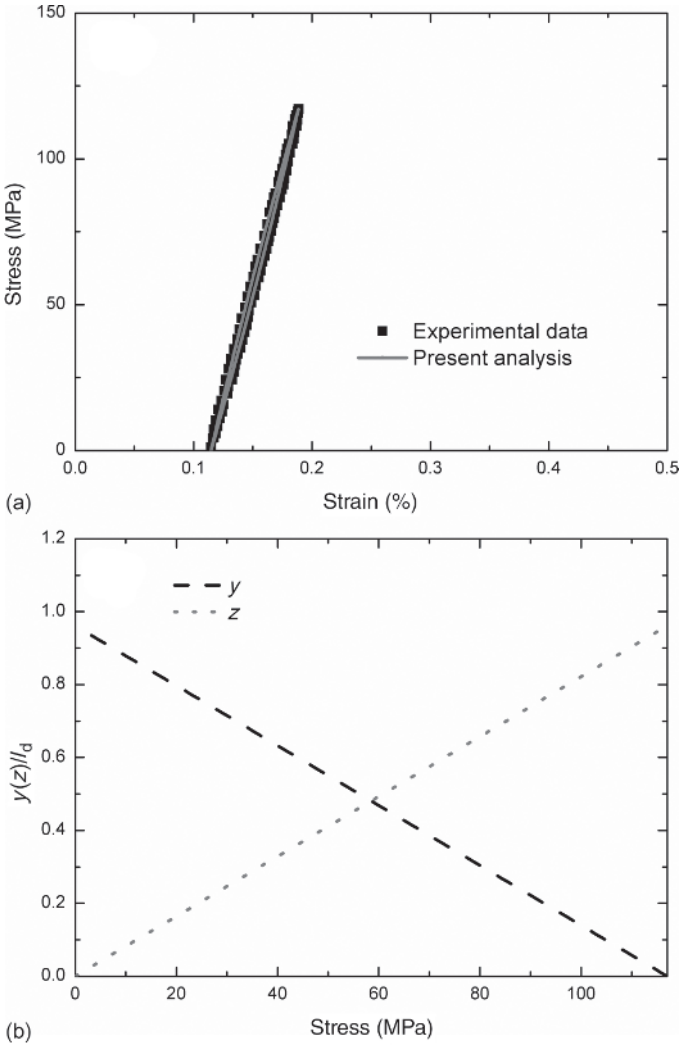

Figure 1.14 (a) The fatigue hysteresis loops; and (b) the interface slip lengths versus the applied stress curves of unidirectional C/Si_3N_4 composite under the fatigue peak stress of $\sigma_{max} = 117$ MPa.

saturation matrix cracking stress of $\sigma_{sat} = 530$ MPa with the saturation matrix crack spacing of $l_{sat} = 193$ μm.

The experimental and theoretical fatigue hysteresis loops and fiber/matrix interface slip lengths versus the applied stress curves are shown in Figures 1.25–1.28. When the fatigue peak stress is $\sigma_{max} = 495$ MPa, the interface partially debonds of $2l_d/l_c < 1$, and the interface counter slip length at the valley stress and the interface new slip length at the peak stress approach to 74% of the interface debonded length of $y/l_d = z/l_d = 74\%$. The fatigue hysteresis loops at the fatigue peak stress of $\sigma_{max} = 495$ MPa correspond to the interface slip Case 2, i.e. the

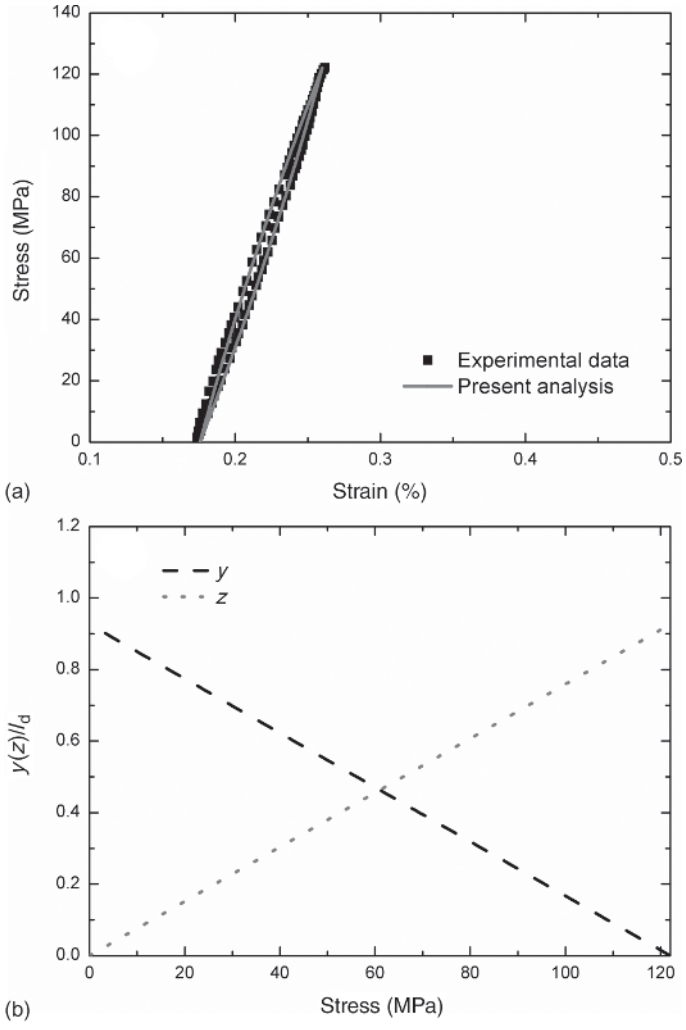

Figure 1.15 (a) The fatigue hysteresis loops; and (b) the interface slip lengths versus the applied stress curves of unidirectional C/Si_3N_4 composite under the fatigue peak stress of $\sigma_{max} = 122$ MPa.

interface partially debonding and the fiber sliding partially relative to matrix in the interface debonded region.

When the fatigue peak stresses are $\sigma_{max} = 545$, 555, and 610 MPa, the interface completely debonds of $2l_d/l_c = 1$, and the interface counter slip length at the valley stress and the interface new slip length at the peak stress approach to 84%, 86%, and 94% of the matrix crack spacing of $2y/l_c = 2z/l_c = 84\%$, 86%, and 94%. The fatigue hysteresis loops at the fatigue peak stresses of $\sigma_{max} = 545$, 555, and 610 MPa correspond to the interface slip Case 3, i.e. the interface completely debonding and the fiber sliding partially relative to matrix in the interface debonded region.

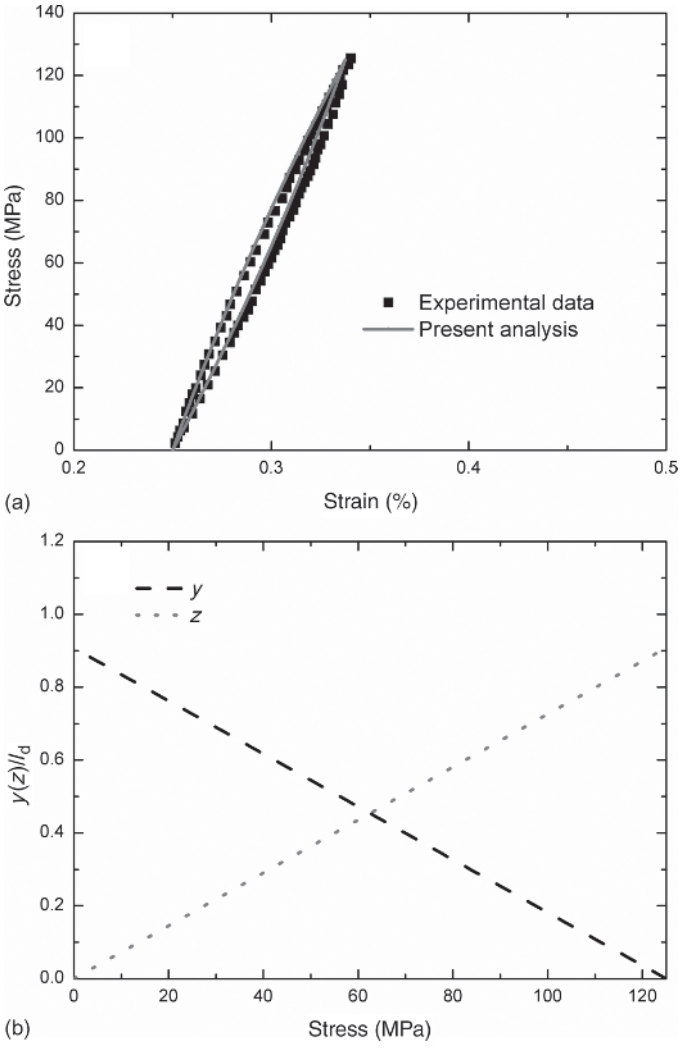

Figure 1.16 (a) The fatigue hysteresis loops; and (b) the interface slip lengths versus the applied stress curves of unidirectional C/Si_3N_4 composite under the fatigue peak stress of $\sigma_{max} = 125$ MPa.

1.2.4.4 SiC/CAS Composite

Pryce and Smith (1993) investigated the cyclic loading/unloading tensile behavior of unidirectional SiC/CAS composite at room temperature. The matrix cracking density as a function of the applied stress curves is shown in Figure 1.29a. The fiber/matrix interface debonding length versus the applied stress is shown in Figure 1.29b. When the fiber/matrix interface debonded length approaches to the half matrix crack space, the fiber/matrix interface completely debonds.

The fatigue hysteresis loops under the fatigue peak stress of $\sigma_{max} = 185$ MPa are shown in Figure 1.30a, and the fiber/matrix interface partially debonds.

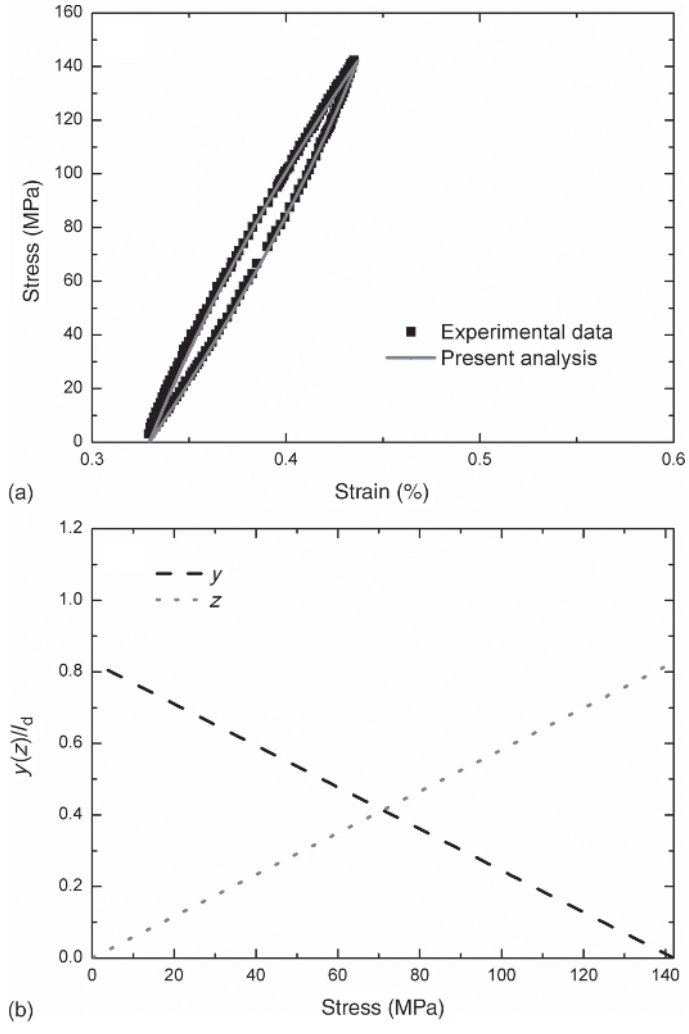

Figure 1.17 (a) The fatigue hysteresis loops; and (b) the interface slip lengths versus the applied stress curves of unidirectional C/Si_3N_4 composite under the fatigue peak stress of $\sigma_{max} = 142$ MPa.

The interface slip lengths as a function of applied stress curves are shown in Figure 1.30b. The interface counter slip length at the unloading transition stress of σ_{tr_pu} approaches to the interface debonded length of $y(\sigma_{tr\_pu}) = l_d$; and the interface new slip length at the reloading transition stress of σ_{tr_pr} approaches to the interface debonded length of $z(\sigma_{tr\_pr}) = l_d$. The fatigue hysteresis loops at the fatigue peak stress of $\sigma_{max} = 185$ MPa correspond to the interface slip Case 1, i.e. the interface partially debonding and the fiber sliding completely relative to matrix in the interface debonded region.

The fatigue hysteresis loops under the fatigue peak stress of $\sigma_{max} = 242$ MPa are shown in Figure 1.31a, and the interface partially debonds. The interface slip

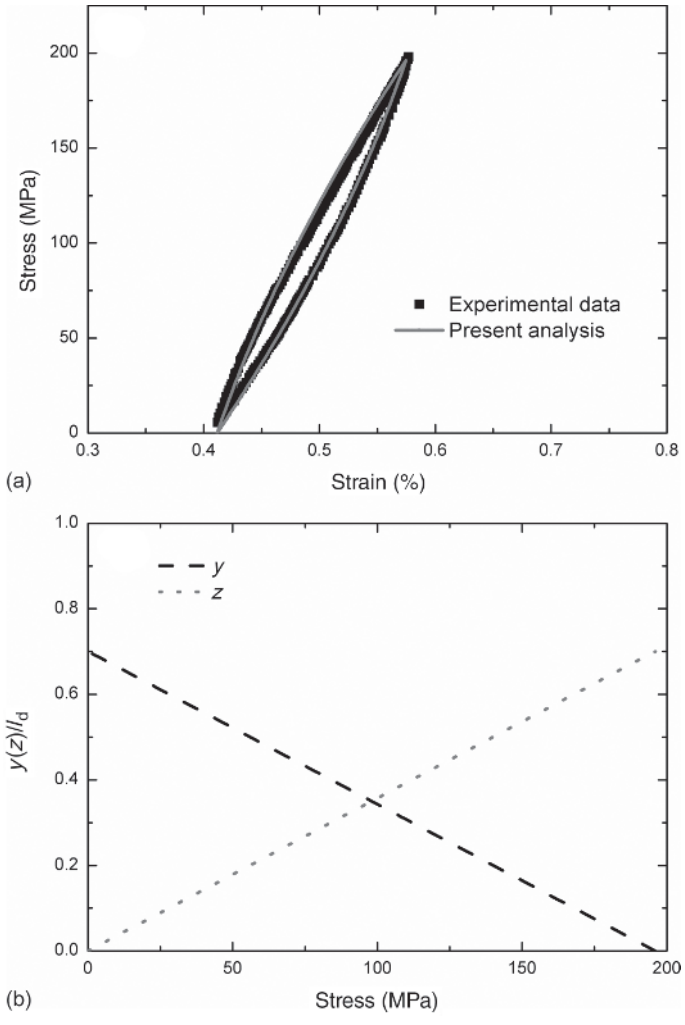

Figure 1.18 (a) The fatigue hysteresis loops; and (b) the interface slip lengths versus the applied stress curves of unidirectional C/Si_3N_4 composite under the fatigue peak stress of $\sigma_{max} = 196$ MPa.

lengths as a function of applied stress are shown in Figure 1.31b. The interface counter slip length at the valley stress of σ_{min} is less than the interface debonded length of $y(\sigma_{min}) < l_d$; and the interface new slip length at the peak stress of σ_{max} is less than the interface debonded length of $z(\sigma_{max}) < l_d$. The fatigue hysteresis loops under the fatigue peak stress of $\sigma_{max} = 242$ MPa correspond to the interface slip Case 2, i.e. the interface partially debonding and the fiber sliding partially relative to matrix in the interface debonded region.

The fatigue hysteresis loop at the fatigue peak stress of $\sigma_{max} = 330$ MPa is shown in Figure 1.32a, and the interface completely debonds. The interface slip lengths

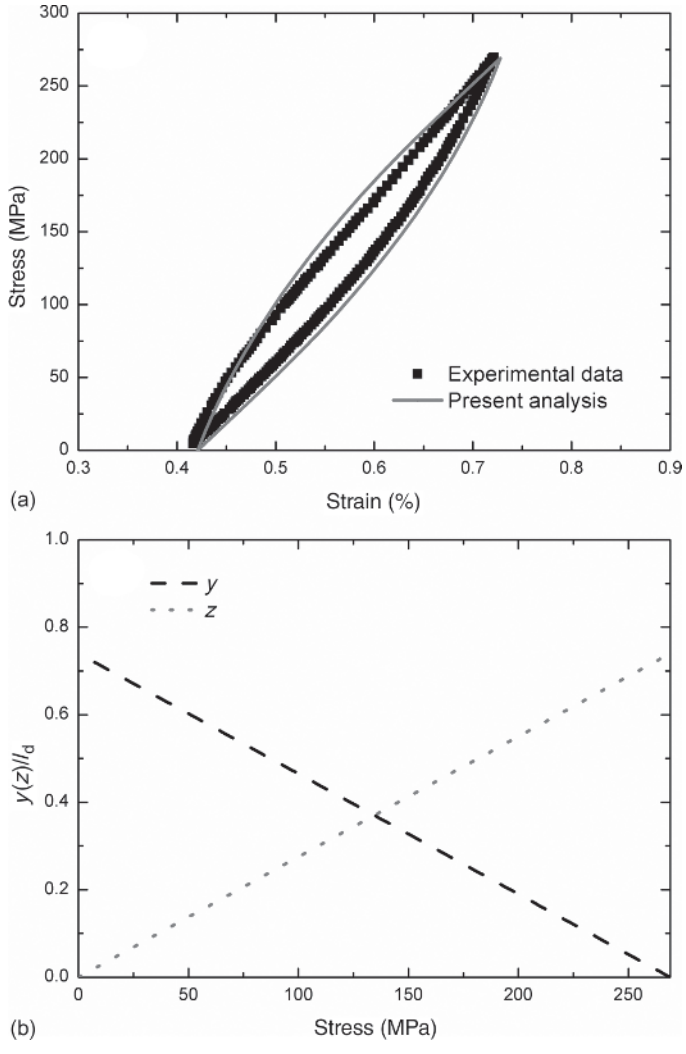

Figure 1.19 (a) The fatigue hysteresis loops; and (b) the interface slip lengths versus the applied stress curves of unidirectional C/Si_3N_4 composite under the fatigue peak stress of $\sigma_{max} = 269$ MPa.

versus the applied stress curves are shown in Figure 1.32b. The interface counter slip length at the valley stress of σ_{min} is less than the half matrix crack spacing of $y(\sigma_{min}) < l_c/2$; and the interface new slip length at the fatigue peak stress of σ_{max} is less than the half matrix crack spacing of $z(\sigma_{max}) < l_c/2$. The fatigue hysteresis loops under the fatigue peak stress of $\sigma_{max} = 330$ MPa correspond to the interface slip Case 3, i.e. the interface completely debonding and the fiber sliding partially relative to matrix in the interface debonded region.

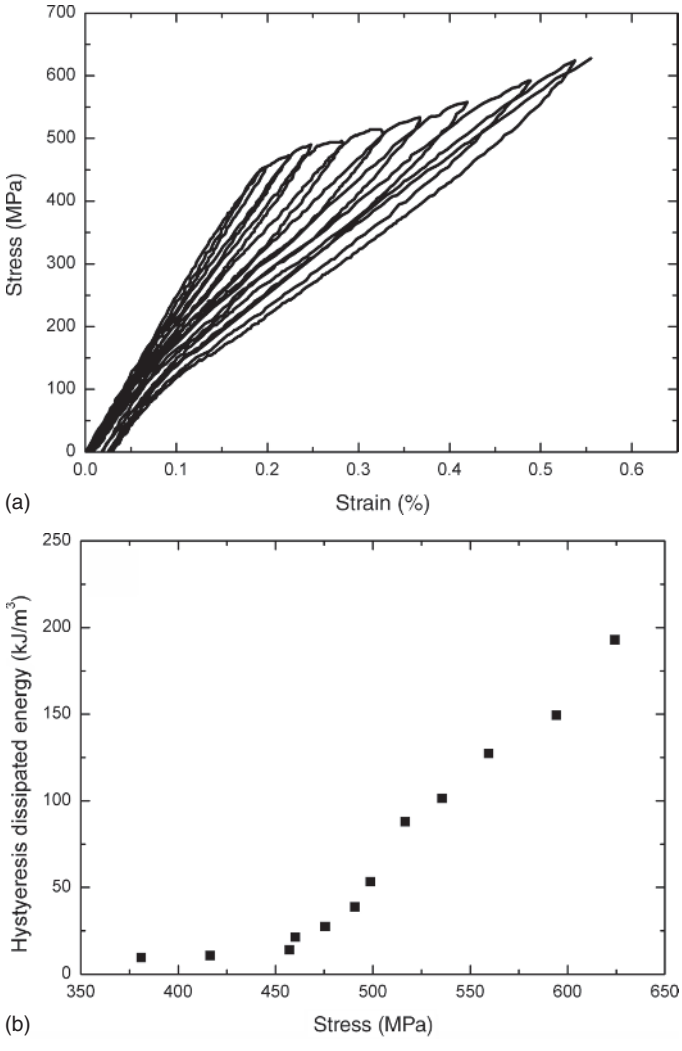

Figure 1.20 (a) The cyclic loading/unloading fatigue hysteresis loops; (b) the fatigue hysteresis dissipated energy versus the applied stress curve; and (c) the matrix cracking density versus the applied stress curve of unidirectional type A SiC/Si_3N_4 composite.

The fatigue hysteresis loop under the fatigue peak stress of $\sigma_{max} = 440$ MPa is shown in Figure 1.33a, and the interface completely debonds. The interface slip lengths as a function of applied stress are shown in Figure 1.33b. The interface counter slip length at the transition stress of σ_{tr_fu} approaches to the half matrix crack spacing of $y(\sigma_{tr\_fu}) = l_c/2$; and the interface new slip length at the transition stress of σ_{tr_fr} approaches to the half matrix crack spacing of $z(\sigma_{tr\_fr}) = l_c/2$. The fatigue hysteresis loops under the fatigue peak stress of $\sigma_{max} = 440$ MPa correspond to the interface slip Case 4, i.e. the interface completely debonding and the fiber sliding completely relative to matrix in the interface debonded region.

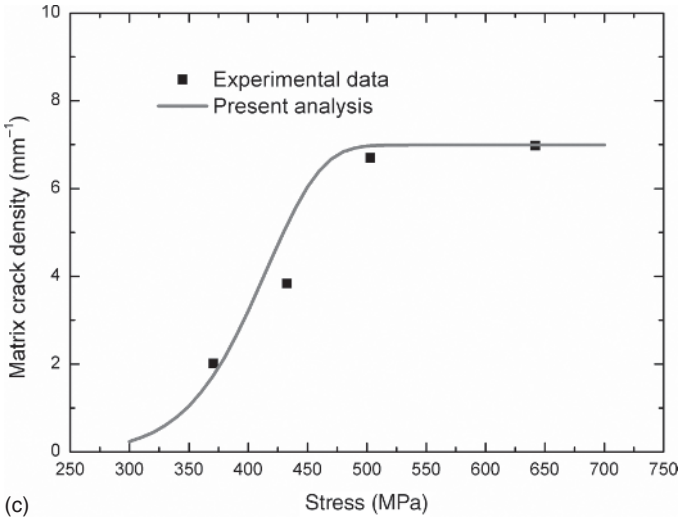

Figure 1.20 (*Continued*)

1.3 Cross-Ply and 2D Woven Ceramic-Matrix Composites

Kuo and Chou (1995) investigated the matrix cracking in [0/90] SiC/CAS composite and divided the cracking states of cross-ply CMCs into five different modes, including

(1) Matrix cracking mode 1, i.e. transverse cracking.
(2) Matrix cracking mode 2, i.e. transverse cracking and matrix cracking with perfect fiber/matrix interface bonding.
(3) Matrix cracking mode 3, i.e. transverse cracking and matrix cracking with fiber/matrix interface debonding.
(4) Matrix cracking mode 4, i.e. matrix cracking with perfect fiber/matrix interface bonding.
(5) Matrix cracking mode 5, i.e. matrix cracking with fiber/matrix interface debonding.

Takeda and Kiriyama (1999) investigated multiple crack evolution of cross-ply CMCs under tensile loading by scanning electron microscopy *in situ* observation. It was found that the matrix cracking mode 3 and mode 5 both existed during multiple crack evolution. Li and Song (2010b) investigated the unloading/reloading tensile and tensile–tensile fatigue behavior of cross-ply [0/90/0/90/0/90/0/90/0] C/SiC composite at room and elevated temperatures. The specimens were observed under optical microscope under tensile and tension–tension fatigue loading. It was also found that the matrix cracking mode 3 and mode 5 both existed during multiple crack evolution. Fantozzi et al. (2001), Fantozzi and Reynaud (2009) investigated the hysteresis behavior of bi- or multidirectional (cross-weave, cross-ply, 2.5D, $[0/+60/-60]_n$) with SiC or C long fibers reinforced SiC, MAS-L, Si-B-C, or C matrix at room and

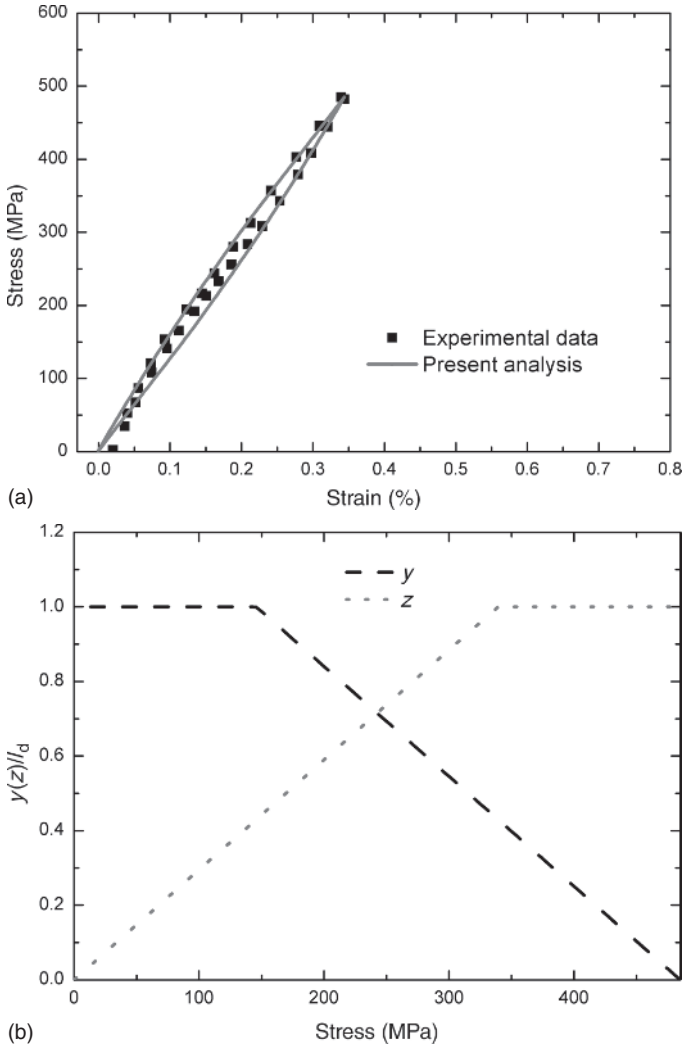

Figure 1.21 (a) The fatigue hysteresis loops; and (b) the interface slip lengths versus the applied stress curves of type A SiC/Si_3N_4 composite under the fatigue peak stress of $\sigma_{max} = 485$ MPa.

elevated temperatures in inert and oxidation atmosphere. By assuming that the mechanical behavior of the composite is mainly controlled by the mechanical behavior of the longitudinal yarns, the hysteresis loop shape variation of these composites under cyclic loading was analyzed. However, the matrix cracking modes affect the shape, area, and location of fatigue hysteresis loops upon unloading and subsequent reloading.

In this section, the effect of matrix cracking on the fatigue hysteresis behavior of cross-ply and 2D woven CMCs is investigated. The matrix cracking mode 3 and mode 5 both involve matrix cracking and fiber/matrix interface debonding in the

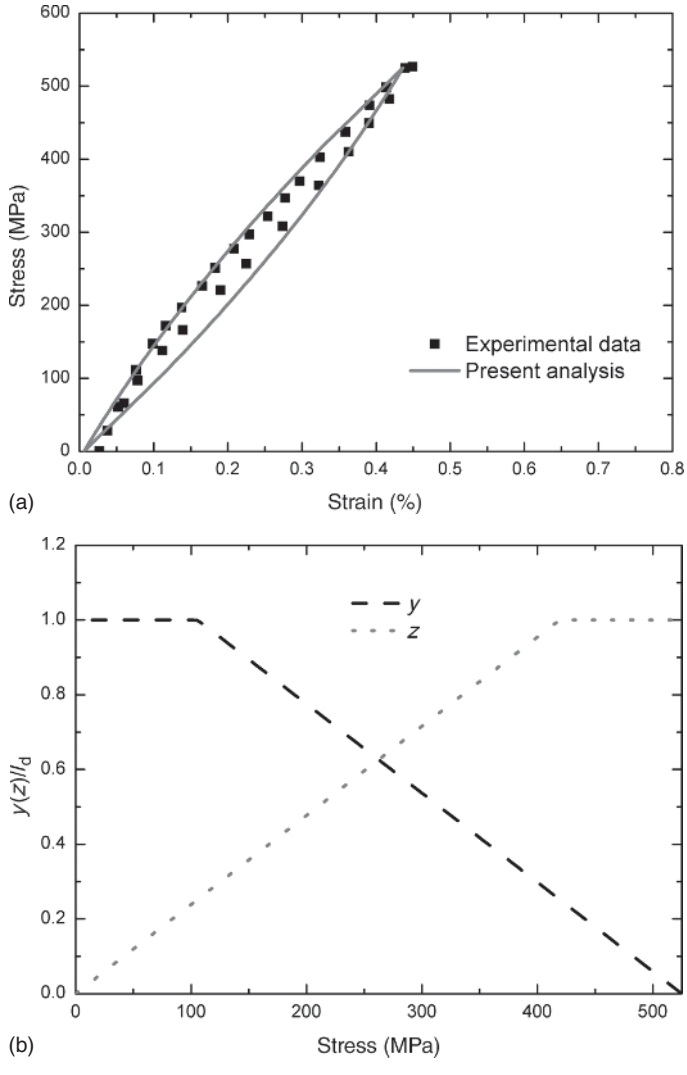

Figure 1.22 (a) The fatigue hysteresis loops; and (b) the interface slip lengths versus the applied stress curves of unidirectional type A SiC/Si_3N_4 composite under the fatigue peak stress of $\sigma_{max} = 525$ MPa.

0° ply or the longitudinal yarns. The matrix cracking statistical model and fracture mechanics fiber/matrix interface debonding criterion are adopted to determine the matrix crack space and fiber/matrix interface debonded length. Based on the damage mechanisms of fiber sliding relative to the matrix upon unloading and subsequent reloading, the unloading interface counter slip length and reloading interface new slip length of matrix cracking mode 3 and mode 5 are determined using the fracture mechanics approach. The fatigue hysteresis loops of four different interface slip cases of matrix cracking mode 3 and mode 5 are analyzed, including

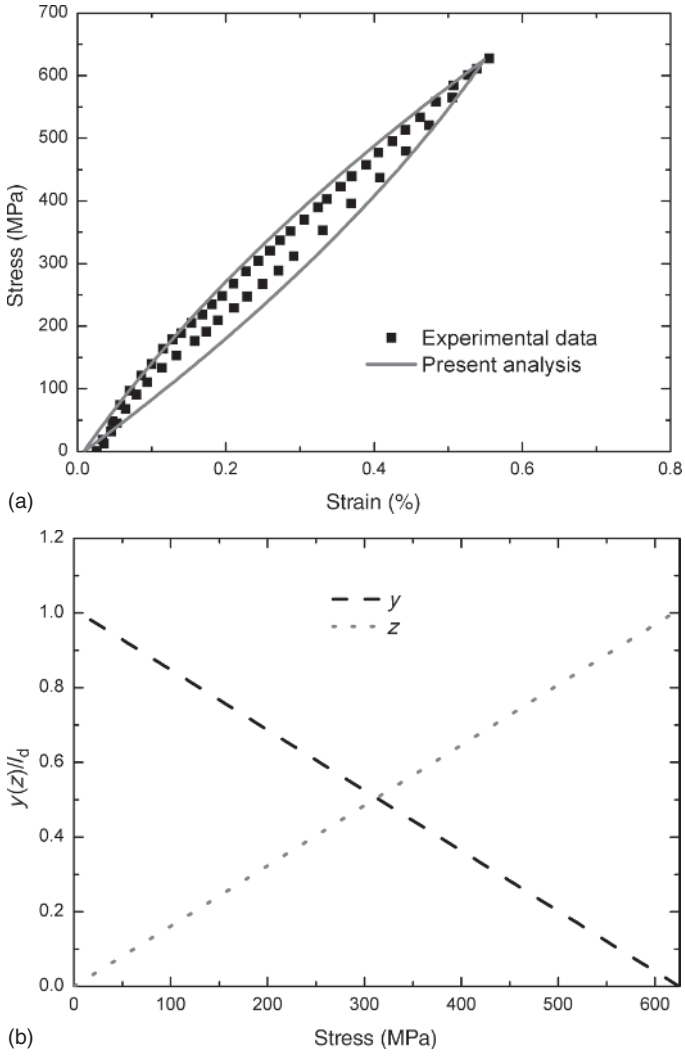

Figure 1.23 (a) The fatigue hysteresis loops; and (b) the interface slip lengths versus applied stress of type A SiC/Si_3N_4 composite under the fatigue peak stress of $\sigma_{max} = 625$ MPa.

(1) Case 1, the fiber/matrix interface partially debonding and the fiber sliding completely relative to matrix in the interface debonded region.
(2) Case 2, the fiber/matrix interface partially debonding and the fiber sliding partially relative to matrix in the interface debonded region.
(3) Case 3, the fiber/matrix interface completely debonding and the fiber sliding partially relative to matrix in the interface debonded region.
(4) Case 4, the fiber/matrix interface completely debonding and the fiber sliding completely relative to matrix in the interface debonded region.

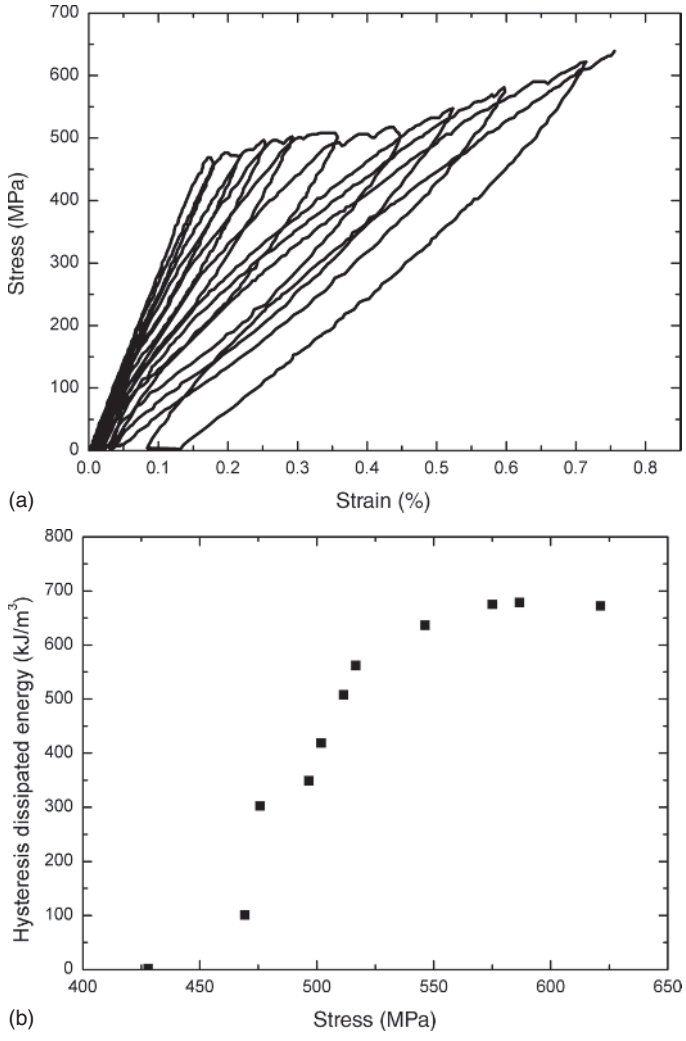

Figure 1.24 (a) The cyclic loading/unloading fatigue hysteresis curves; (b) the fatigue hysteresis dissipated energy versus the applied stress curve; and (c) the matrix cracking density versus the applied stress curve of unidirectional type B SiC/Si_3N_4 composite.

1.3.1 Materials and Experimental Procedures

1.3.1.1 C/SiC Composite

The cross-ply T-700™ C/SiC CMCs were manufactured by hot-pressing method, which offered the ability to fabricate dense composites via a liquid phase sintering method at a low temperature. The fibers have an average diameter of 7 μm and come on a spool as a tow of 12K fibers. The volume fraction of fibers was approximately 40%. Low pressure CVI was employed to deposit approximately 5–20 layers of PyC/SiC with the mean thickness of 0.2 μm in order to enhance the desired nonlinear/non-catastrophic tensile behavior. The dog-bone shaped

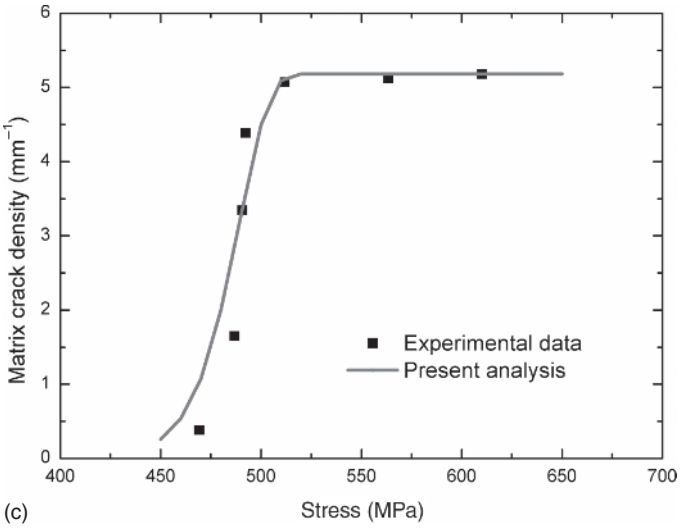

Figure 1.24 (*Continued*)

specimens, with 123 mm length, 3.8 mm thickness, and 10 mm width in the gage section for cross-ply composites, were cut from the 150 mm × 150 mm panels by water cutting. The specimens were further coated with SiC of about 20 μm thick by CVD to prevent oxidation at high temperature. These processing steps resulted in a material having bulk density of about 2.0 g/cm^3 and an open porosity below 5%.

The loading/unloading tensile experiments at room temperature were conducted on MTS Model 809 servo hydraulic load frame (MTS System Corp., Minneapolis, MN) equipped with edge-loaded grips, operated at the loading rate of 2.0 MPa/s. The gage-section strains were measured using a clip-on extensometer (Model No. 634.12F-24, MTS systems Corp., modified for a 25 mm gage-length). The direct observations of matrix cracking were made using HiROX optical microscope. The matrix crack density was determined by counting the number of the cracks in a length of about 15 mm.

1.3.1.2 SiC/SiC Composite

Silicon carbide fiber bundles were woven into fabrics and laminated to form prefabricates. The surface of the fibers was treated and PyC interfacial layer was deposited on the surface. SiC matrix was deposited by CVI process. Finally, a 2D SiC/SiC composite plate was made, and dog bone specimens were obtained by cutting. A chamfered stiffener is pasted at both ends of the specimen to prevent local crushing of the specimen. Tensile test was completed on Instron 5567 testing machine. The loading speed was 0.3 mm/min, and the tensile strain of the material was measured in real time by an extensometer with a distance of 25 mm. In addition, cyclic loading and unloading tests are carried out between 150 and 240 MPa and unloaded every 30 MPa.

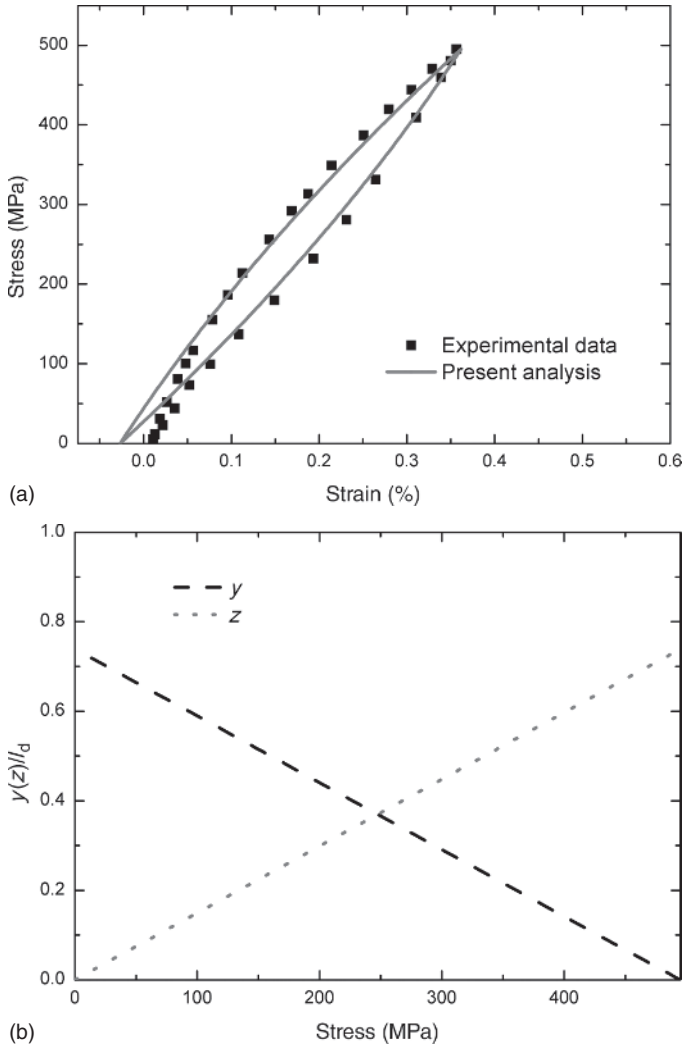

Figure 1.25 (a) The fatigue hysteresis loops; and (b) the interface slip lengths versus the applied stress of type B SiC/Si_3N_4 composite under the fatigue peak stress of $\sigma_{max} = 495$ MPa.

1.3.2 Theoretical Analysis

1.3.2.1 Stress Analysis

The stress distribution of the damaged composites upon first loading of the undamaged composites to the fatigue maximum stress is investigated in this section. In order to model the response of a cross-ply or 2D woven laminate using a one dimensional unit cell, a number of simplifying assumptions are required. The composite is considered to be composed of three entities, i.e. the 90° ply, the fiber in the 0° ply, and the matrix in the 0° ply. The total thickness of the 0° ply and 90° ply are $2b$ and $2d$, respectively. The fibers are assumed to be prismatic and uniformly spaced throughout the matrix of each ply. Upon first loading to

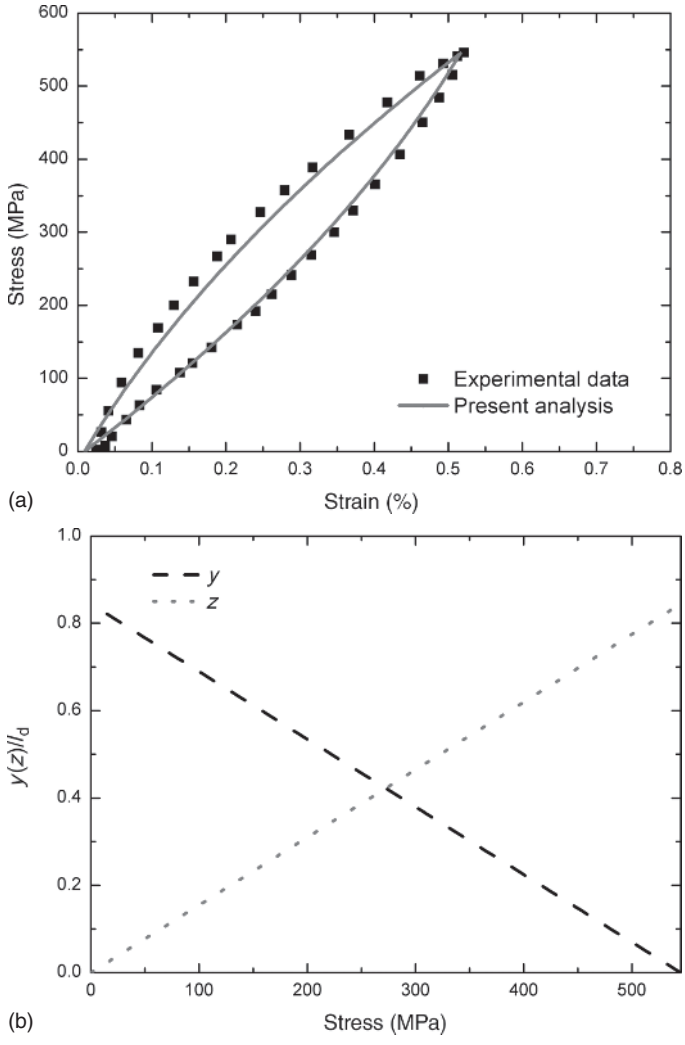

Figure 1.26 (a) The fatigue hysteresis loops; and (b) the interface slip lengths versus the applied stress curves of unidirectional type B SiC/Si_3N_4 composite under the fatigue peak stress of $\sigma_{max} = 545$ MPa.

the maximum stress σ_{max}, which is higher than the initial cracking stress of 90° ply and 0° ply, it is assumed that the transverse cracks and matrix cracks would extend throughout the entire laminate cross section. Kuo and Chou (1995) investigated the undamaged state and damaged state of the cross-ply laminate and classified the damaged state into five modes, as shown in Figure 1.34. It can be found that the fiber/matrix interface debonding only occurs in cracking mode 3 and mode 5. The stress analysis for mode 3 and mode 5 is given as follows.

1.3.2.1.1 Cracking Mode 3 The unit cell of the matrix cracking mode 3, which contains transverse crack and matrix crack at the same cross section and with

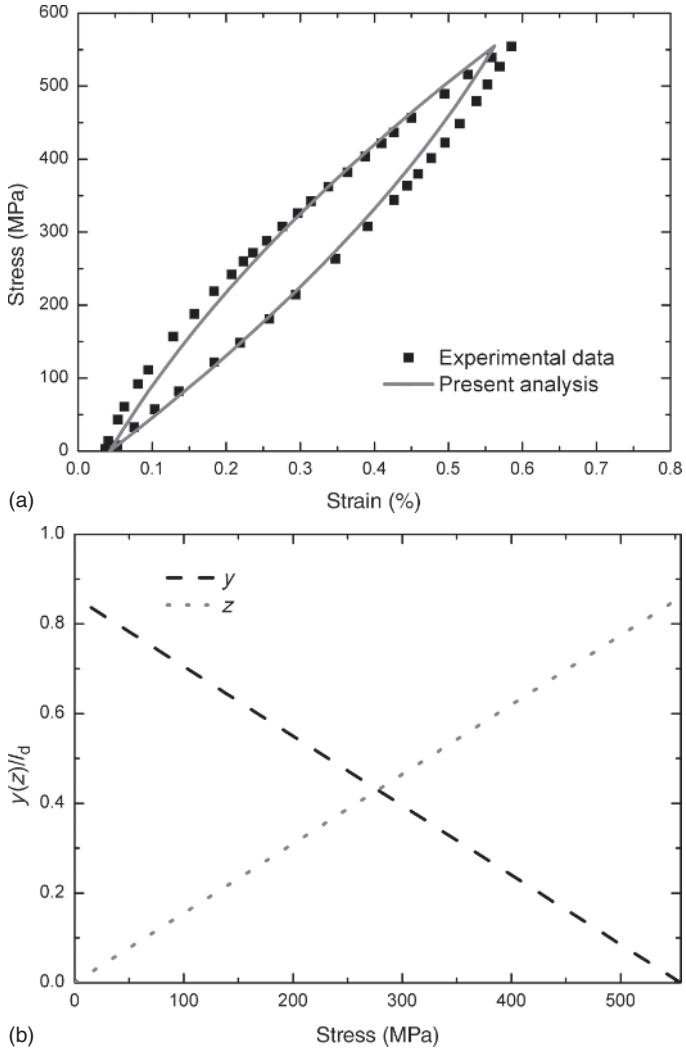

Figure 1.27 (a) The fatigue hysteresis loops; and (b) the interface slip lengths versus the applied stress curves of unidirectional type B SiC/Si_3N_4 composite under the fatigue peak stress of $\sigma_{max} = 555$ MPa.

fiber/matrix interface debonding, is illustrated in Figure 1.34d. The length of the unit cell is $l_c/2$, which is just the half matrix crack space. The interface debonded length is l_d. In the previous study (Kuo and Chou 1995), it is assumed that the stress in the 90° ply is not influenced by matrix cracks within the 0° plies. Hence, transverse cracks result in loads being transferred locally between plies, whereas matrix cracks produce a local redistribution of stresses between the constituents of the 0° ply. This same assumption is now made in the current analysis. The axial stress distributions of fiber (σ_f), matrix (σ_m), and 90° ply (σ_t) are given by the following equations, where σ referring to Figure 1.34a denotes the stress applied

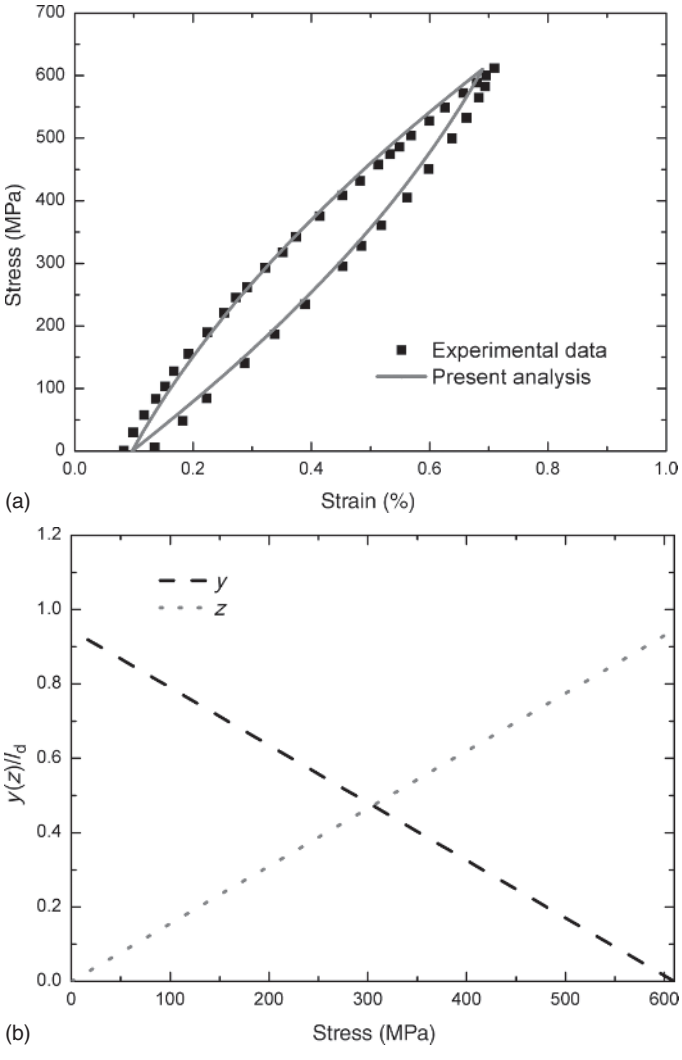

Figure 1.28 (a) The fatigue hysteresis loops; and (b) the interface slip lengths versus the applied stress curves of unidirectional type B SiC/Si_3N_4 composite under the fatigue peak stress of $\sigma_{max} = 610$ MPa.

on the composite:

$$\sigma_f(x) = \begin{cases} \frac{1}{V_f}\frac{b+d}{b}\sigma - \frac{2\tau_i}{r_f}x, & x \in (0, l_d) \\ \sigma_{fo} + \left(\frac{1}{V_f}\frac{b+d}{b}\sigma - \frac{2\tau_i}{r_f}l_d - \sigma_{fo}\right)\exp\left(-\rho\frac{x-l_d}{r_f}\right), & x \in (l_d, l_c/2) \end{cases} \tag{1.50}$$

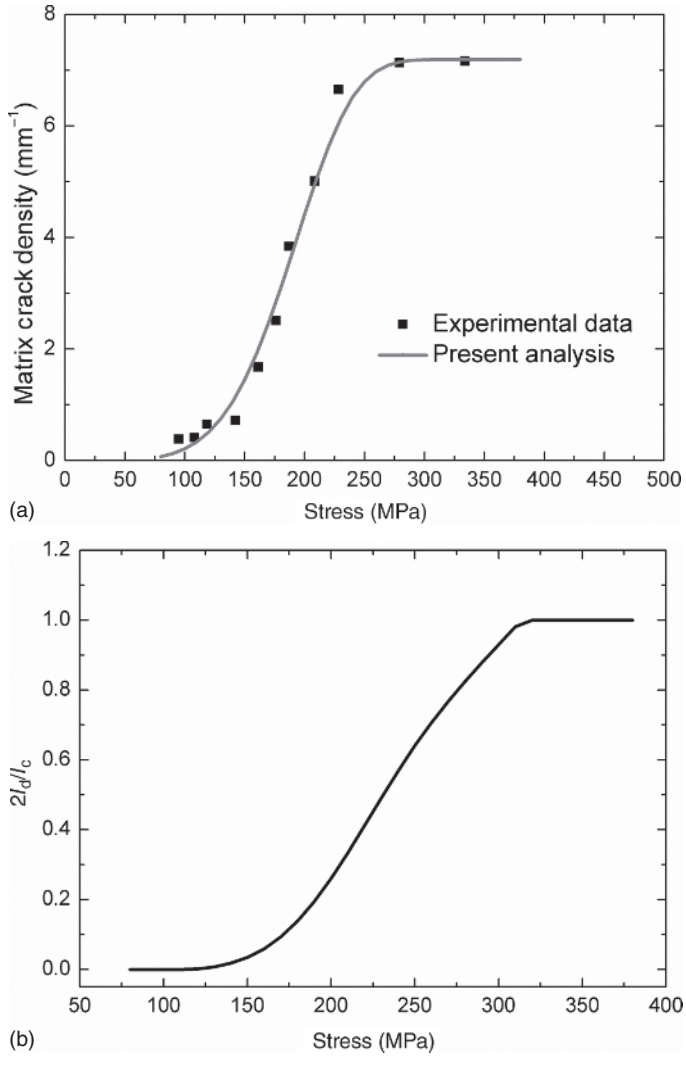

Figure 1.29 (a) The matrix cracking density versus the applied stress curves; and (b) the fiber/matrix interface debonding length versus the applied stress curves of unidirectional SiC/CAS composite.

$$\sigma_m(x) = \begin{cases} 2\tau_i \frac{V_f}{V_m} \frac{x}{r_f} - \frac{d}{b} \frac{\sigma_t(x)}{V_m}, & x \in (0, l_d) \\ \sigma_{mo} + \frac{d}{b} \frac{\sigma_{to} - \sigma_t(x)}{V_m} - \left(\sigma_{mo} + \frac{d}{b} \frac{\sigma_{to}}{V_m} - 2\tau_i \frac{V_f}{V_m} \frac{l_d}{r_f} \right) \\ \times \exp\left(-\rho \frac{x - l_d}{r_f} \right), & x \in (l_d, l_c/2) \end{cases} \tag{1.51}$$

$$\sigma_t(x) = \sigma_{to}(1 - \exp(-\lambda x)), \quad x \in (0, l_c/2) \tag{1.52}$$

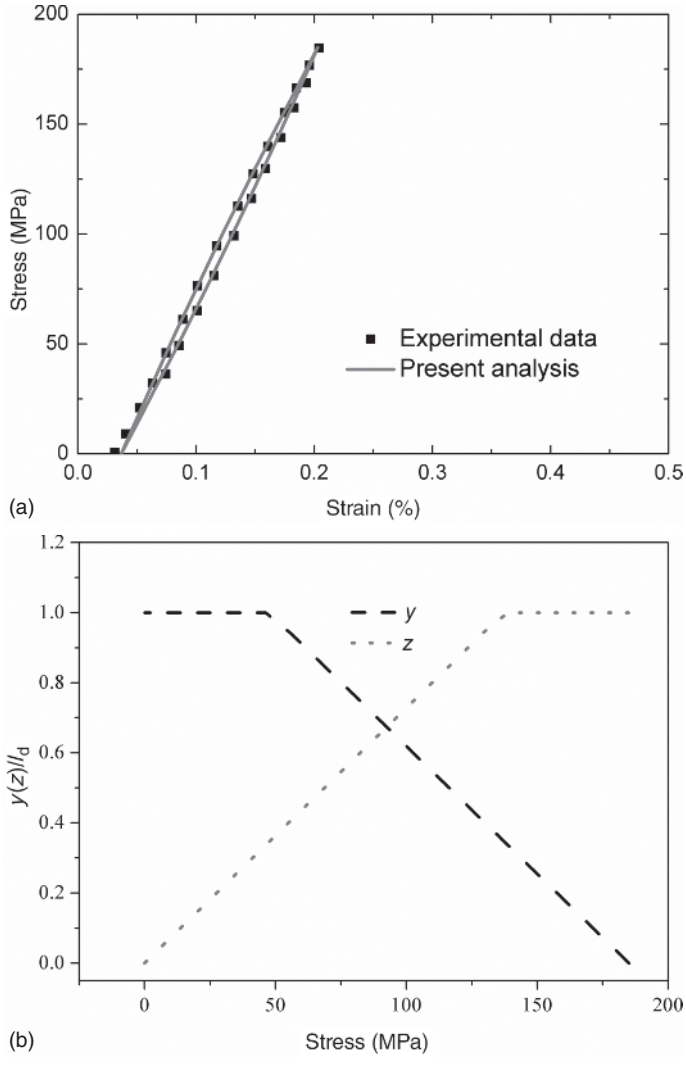

Figure 1.30 (a) The fatigue hysteresis loops; and (b) the interface slip lengths versus the applied stress of unidirectional SiC/CAS composite under the fatigue peak stress of $\sigma_{max} = 185$ MPa.

where r_f denotes fiber radius, V_f and V_m denote fiber and matrix volume fraction, τ_i denotes fiber/matrix interface shear stress, and ρ denotes the shear-lag parameter (Budiansky et al. 1986):

$$\rho^2 = \frac{4E_c G_m}{V_m E_m E_f \varphi} \tag{1.53}$$

where G_m denotes matrix shear modulus, and

$$\varphi = -\frac{2\ln V_f + V_m(3 - V_f)}{2V_m^2} \tag{1.54}$$

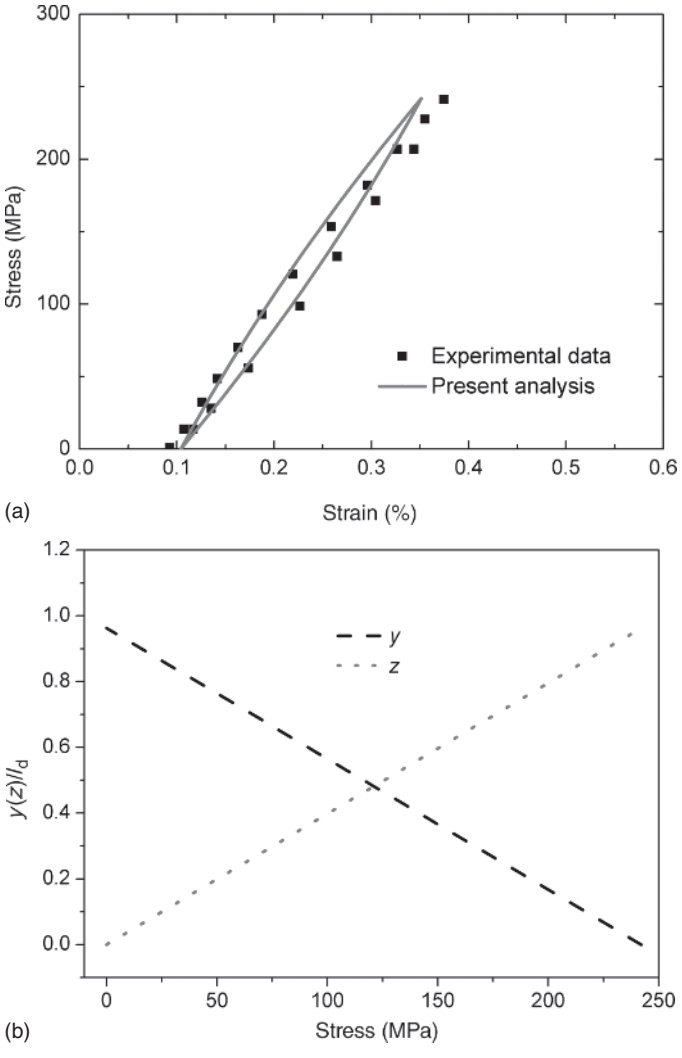

Figure 1.31 (a) The fatigue hysteresis loops; (b) the interface slip lengths versus the applied stress of unidirectional SiC/CAS composite under the fatigue peak stress of $\sigma_{max} = 242$ MPa.

where λ denotes the Lee–Daniel shear-lag parameter (Lee and Daniel 1990):

$$\lambda^2 = \frac{3G_{12}G_{23}}{bG_{23} + dG_{12}} \frac{bE_1 + dE_2}{bdE_1E_2} \tag{1.55}$$

where G_{13} and G_{23} denote the shear modulus of the composite and E_1 and E_2 denote the 0° ply and 90° ply elastic modulus, respectively. σ_{fo}, σ_{mo}, and σ_{to} denote fiber, matrix, and 90° ply axial stress in the interface bonded region, respectively.

$$\sigma_{fo} = \frac{E_f}{E_c}\sigma + E_f(\alpha_c - \alpha_f)\Delta T \tag{1.56}$$

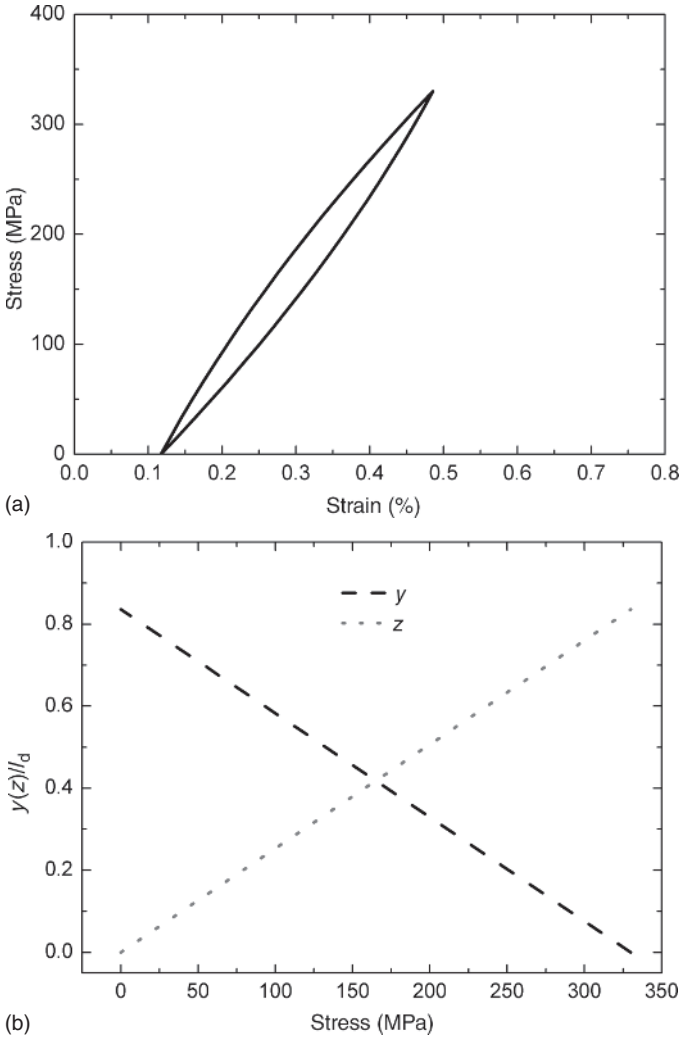

Figure 1.32 (a) The fatigue hysteresis loops; and (b) the interface slip lengths versus the applied stress of unidirectional SiC/CAS composite under the fatigue peak stress of $\sigma_{max} = 330$ MPa.

$$\sigma_{mo} = \frac{E_m}{E_c}\sigma + E_m(\alpha_c - \alpha_m)\Delta T \tag{1.57}$$

$$\sigma_{to} = \frac{E_2}{E_c}\sigma + E_2(\alpha_c - \alpha_2)\Delta T \tag{1.58}$$

where E_f, E_m, and E_c denote fiber, matrix, and composite elastic modulus, respectively. α_f, α_m, α_2, and α_c denote fiber, matrix, 90° ply, and composite thermal expansion coefficient, respectively. ΔT denotes the temperature difference between the fabricated temperature T_0 and testing temperature T_1 ($\Delta T = T_1 - T_0$). The axial elastic modulus of the composite is approximated by

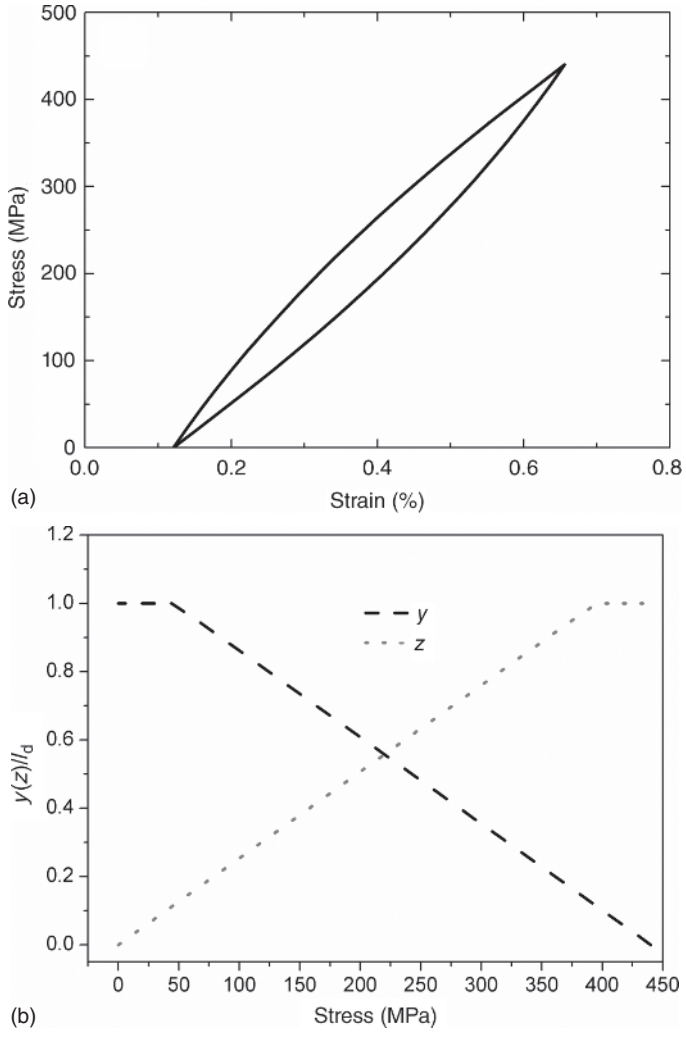

Figure 1.33 (a) The fatigue hysteresis loops; and (b) the interface slip lengths versus the applied stress of unidirectional SiC/CAS composite under the fatigue peak stress of $\sigma_{max} = 440$ MPa.

the rule of mixture:

$$E_c = \frac{bE_1 + dE_2}{b + d} \tag{1.59}$$

1.3.2.1.2 Cracking Mode 5 The unit cell of the cracking mode 5, which contains matrix crack with fiber/matrix interface debonding, is illustrated in Figure 1.34f. The length of the unit cell is $l_c/2$, which is the half matrix crack space. The fiber/matrix interface debonded length is l_d. The axial stress distribution of fiber,

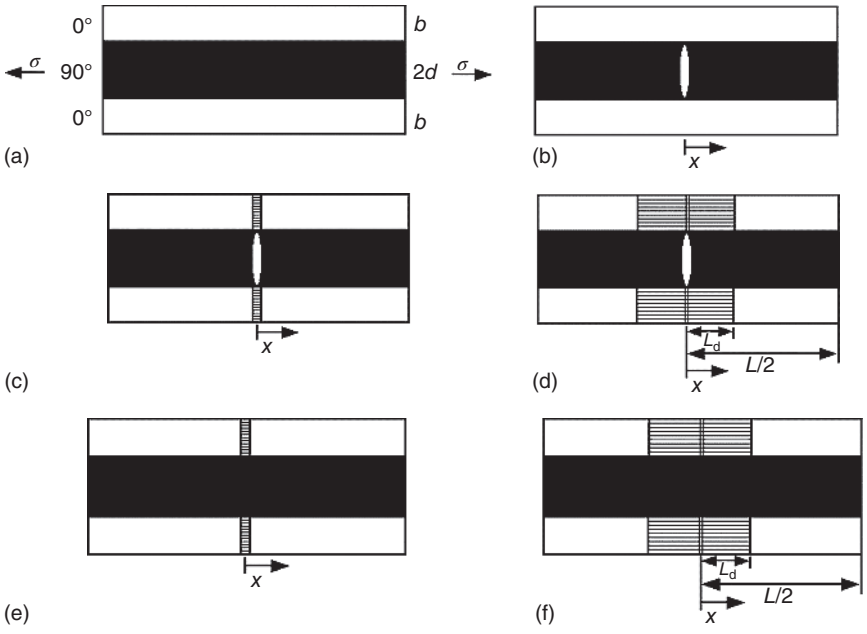

Figure 1.34 (a) Undamaged composite; (b) mode 1; (c) mode 2; (d) mode 3; (e) mode 4; and (f) mode 5 of cross-ply CMCs.

matrix, and 90° ply is given by the following equation:

$$\sigma_f(x)=\begin{cases}\frac{1}{V_f}\left(\frac{b+d}{b}\sigma-\frac{d}{b}\sigma_{to}\right)-\frac{2\tau_i}{r_f}x, & x\in(0,l_d)\\ \sigma_{fo}+\left[\frac{1}{V_f}\left(\frac{b+d}{b}\sigma-\frac{d}{b}\sigma_{to}\right)-\frac{2\tau_i}{r_f}l_d-\sigma_{fo}\right]\\ \quad\times\exp\left(-\rho\frac{x-l_d}{r_f}\right), & x\in(l_d,l_c/2)\end{cases} \tag{1.60}$$

$$\sigma_m(x)=\begin{cases}2\tau_i\frac{V_f}{V_m}\frac{x}{r_f}, & x\in(0,l_d)\\ \sigma_{mo}-\left(\sigma_{mo}-2\tau_i\frac{V_f}{V_m}\frac{l_d}{r_f}\right)\exp\left(-\rho\frac{x-l_d}{r_f}\right), & x\in(l_d,l_c/2)\end{cases} \tag{1.61}$$

$$\sigma_t(x)=\sigma_{to},\quad x\in(0,l_c/2) \tag{1.62}$$

where σ_{fo}, σ_{mo}, and σ_{to} are given in Eq. (1.56)–(1.58).

1.3.2.2 Transverse and Matrix Cracking

When cross-ply ceramic laminates are subjected to tensile loading, transverse cracking and matrix cracking occur in 90° ply and 0° ply, respectively. Kuo and Chou (1995) investigated the initial transverse cracking stress (damage mode 1 in Figure 1.34b) using the energy balance approach:

$$\sigma_{cr90}=\left(\frac{2}{3}\frac{\lambda bE_1E_c\xi_t}{(b+d)E_2}\right)^{1/2}-E_c(\alpha_c-\alpha_2)\Delta T \tag{1.63}$$

where ξ_t denotes the transverse fracture energy. As the increasing of the applied stress, the transverse crack would propagate and approach saturation. There are

three methods to the problem of the evolution of transverse cracking, namely, the maximum stress criterion, fracture mechanics approach, and stochastic approach. The maximum stress criterion (Garrett and Bailey 1977) assumes single-valued strength in 90° ply. When the local stress in the 90° ply reaches the failure strength, transverse cracking occurs. The fracture mechanics approach assumes that when the critical energy release rate reaches transverse fracture energy, transverse cracking occurs (Laws and Dvorak 1988). The stochastic approach considers the distribution of flaws sizes and locations (Fukunaga et al. 1984).

During propagation of transverse cracks, some transverse cracks would enter the 0° ply forming the major crack (damage mode 3 in Figure 1.34d). The matrix crack space decreases as stress above the initial matrix cracking stress increases and may eventually attain saturation. There are four dominant failure criterions presented in the literature for modeling matrix crack evolution: maximum stress criterion, energy balance approach, critical matrix strain energy criterion, and statistical failure approach. The maximum stress criterion (Daniel and Lee 1993) assumes that a new matrix crack would form whenever the matrix stress exceeds the matrix strength, which is assumed to be single-valued and a known material property. The energy balance failure criterion involves calculation of the energy balance relationship before and after the formation of a single dominant crack as originally proposed by Aveston et al. (1971). The progression of matrix cracking as determined by the energy criterion is dependent on matrix strain energy release rate. The energy criterion is represented by Zok and Spearing (1992) and Zhu and Weitsman (1994). The concept of a critical matrix strain energy criterion presupposes the existence of an ultimate or critical strain energy limit beyond which the matrix fails (Solti et al. 1995). Beyond this, as more energy is placed into the composite, the matrix, unable to support the additional load, continues to fail. As more energy is placed into the system, the matrix fails such that all the additional energy is transferred to the fibers. Failure may be due to the formation of matrix cracks, the propagation of existing cracks or fiber/matrix interface debonding, or the 90°/0° plies interface debonding is not considered in the present analysis. Statistical failure approach assumes matrix cracking is governed by statistical relations, which relate to the size and spatial distribution of matrix flaws to their relative propagation stress (Curtin 1993). The brittle nature of the matrix material and the possible formation of initial cracks distribution throughout the microstructure suggest that a statistical approach to matrix crack evolution is warranted in CMCs. The tensile strength of the brittle matrix is assumed to be described by the two-parameter Weibull distribution where the probability of the matrix failure, P_m, is given by the following equation (Curtin 1993):

$$P_m = 1 - \exp\left[-\left(\frac{\sigma_m}{\sigma_R}\right)^m\right] \tag{1.64}$$

where σ_m denotes the tensile stress in the matrix and σ_R and m denote the matrix characteristic strength and matrix Weibull modulus, respectively. To estimate the instantaneous matrix crack space with increasing applied stress, P_m is given by the following equation:

$$P_m = l_{sat}/l_c \tag{1.65}$$

where l_c denotes the instantaneous matrix crack space and l_{sat} denotes the saturation matrix crack space. Using Eqs. (1.64) and (1.65), the instantaneous matrix crack space is given by the following equation:

$$l_c = l_{sat}\left\{1 - \exp\left[-\left(\frac{\sigma_m}{\sigma_R}\right)^m\right]\right\}^{-1} \tag{1.66}$$

1.3.2.3 Interface Debonding

The fracture mechanics approach is adopted in the present analysis. The interface debonding criterion is given by the following equation (Gao et al. 1988):

$$\xi_d = \frac{F}{4\pi r_f}\frac{\partial w_f(0)}{\partial l_d} - \frac{1}{2}\int_0^{l_d}\tau_i\frac{\partial v(x)}{\partial l_d}dx \tag{1.67}$$

where $F = \pi r_f^2\sigma/V_f$ is the fiber load at the matrix crack plane. $w_f(0)$ denotes the fiber axial displacement at the matrix crack plane. $v(x)$ denotes the relative displacement between the fiber and matrix.

1.3.2.3.1 Cracking Mode 3 For the matrix cracking mode 3, the axial displacement of fiber and matrix, $w_f(x)$ and $w_m(x)$, are given by the following equation:

$$\begin{aligned} w_f(x) &= \frac{1}{E_f}\int_x^{l_c/2}\sigma_f(x)dx = \frac{1}{V_f E_f}\frac{b+d}{b}\sigma(l_d - x) - \frac{\tau_i}{r_f E_f}(l_d^2 - x^2) \\ &\quad + \frac{\sigma}{E_c}(l_c/2 - l_d) + \frac{r_f}{\rho V_f E_f}\frac{b+d}{b}\sigma - \frac{r_f}{\rho E_c}\sigma - \frac{2\tau_i}{\rho E_f}l_d \end{aligned} \tag{1.68}$$

$$\begin{aligned} w_m(x) &= \frac{1}{E_m}\int_x^{l_c/2}\sigma_m(x)dx = \frac{1}{V_m E_m}\left(\frac{b+d}{b}\sigma - \frac{d}{b}\sigma_{to}\right)(l_c/2 - x) \\ &\quad + \frac{1}{\lambda V_m E_m}\frac{d}{b}\sigma_{to}\exp(-\lambda x) \\ &\quad - \frac{1}{V_m E_m}\frac{b+d}{b}\sigma(l_d - x) + \frac{V_f\tau_i}{r_f V_m E_m}(l_d^2 - x^2) \\ &\quad - \frac{V_f E_f\sigma}{V_m E_m E_c}(l_c/2 - l_d) \\ &\quad - \frac{r_f}{\rho V_m E_m}\frac{b+d}{b}\sigma + \frac{r_f V_f E_f}{\rho V_m E_m E_c}\sigma + \frac{2V_f\tau_i}{\rho V_m E_m}l_d \end{aligned} \tag{1.69}$$

Using Eqs. (1.68) and (1.69), the relative displacement between the fiber and matrix can be described using the following equation:

$$\begin{aligned} v(x) = |w_f(x) - w_m(x)| &= \frac{(b+d)E_1}{bV_f V_m E_f E_m}\sigma(l_d - x) - \frac{E_1\tau_i}{r_f V_m E_f E_m}(l_d^2 - x^2) \\ &\quad + \frac{E_1}{V_m E_m E_c}(l_c/2 - l_d)\sigma + \frac{r_f(b+d)E_1\sigma}{\rho b V_f V_m E_f E_m} - \frac{r_f E_1\sigma}{\rho V_m E_m E_c} - \frac{2E_1\tau_i}{\rho V_m E_f E_m}l_d \\ &\quad - \frac{1}{V_m E_m}\left(\frac{b+d}{b}\sigma - \frac{d}{b}\sigma_{to}\right)(l_c/2 - x) - \frac{1}{\lambda V_m E_m}\frac{d}{b}\sigma_{to}\exp(-\lambda x) \end{aligned} \tag{1.70}$$

Substituting $w_f(x=0)$ and $v(x)$ into Eq. (1.67), it leads to the form of the following equation:

$$l_d = \frac{r_f}{2}\left[\frac{V_m E_m}{V_f E_c \tau_i}\sigma\left(1+\frac{1}{2}\frac{d}{b}\frac{E_2}{V_m E_m}+\frac{1}{2}\frac{d}{b}\frac{E_2}{E_1}\right)-\frac{1}{\rho}\right] - \sqrt{\frac{1}{4}\left(\frac{1}{2}r_f\frac{E_f E_2}{E_1 E_c}\frac{d}{b}\frac{\sigma}{\tau_i}-\frac{r_f}{\rho}\right)^2+\frac{r_f V_m E_f E_m}{E_1\tau_i^2}\xi_d} \tag{1.71}$$

The initial interface debonding stress is obtained by substituting $l_d = 0$ into Eq. (1.71):

$$\sigma_d = \frac{bV_f E_c \tau_i}{\rho(bV_m E_m + dE_2)}\left[1+\sqrt{1+4\frac{(bV_m E_m + dE_2)E_f}{(b+d)r_f E_c}\frac{\rho^2}{\tau_i^2}\xi_d}\right] \tag{1.72}$$

The interface completely debonding stress is obtained by substituting $l_d = l_c/2$ into Eq. (1.71):

$$\sigma_b = \frac{bV_f E_c \tau_i}{\rho(bV_m E_m + dE_2)}\left[1+\frac{\rho L}{2r_f}+\frac{1}{2}\frac{bV_m E_m + dE_2}{bE_1 + dE_2}\frac{\rho E_1 l_c}{r_f V_m E_m} + \sqrt{\left(\frac{1}{2}\frac{d}{b+d}\frac{V_f E_f}{V_m E_m}\frac{E_2}{E_c}\frac{\rho l_c}{r_f}-1\right)^2+4\frac{(bV_m E_m + dE_2)E_f}{r_f(b+d)E_c}\frac{\rho^2}{\tau_i^2}\xi_d}\right] \tag{1.73}$$

1.3.2.3.2 Cracking Mode 5 For the matrix cracking mode 5, the axial displacement of fiber and matrix, $w_f(x)$ and $w_m(x)$, can be described using the following equations:

$$\begin{aligned} w_f(x) = \frac{1}{E_f}\int_x^{l_c/2}\sigma_f(x)\mathrm{d}x &= \frac{1}{V_f E_f}\left(\frac{b+d}{b}\sigma-\frac{d}{b}\sigma_{to}\right) \\ &\times(l_d - x) - \frac{\tau_i}{r_f E_f}(l_d^2 - x^2) + \frac{\sigma_{fo}}{E_c}(l_c/2 - l_d) \\ &+\frac{2\tau_i}{\rho E_f}l_d + \frac{r_f}{\rho V_f E_f}\left(\frac{b+d}{b}\sigma-\frac{d}{b}\sigma_{to}\right)+\frac{r_f\sigma_{fo}}{\rho E_c} \end{aligned} \tag{1.74}$$

$$\begin{aligned} w_m(x) = \frac{1}{E_m}\int_x^{l_d}\sigma_m(x)\mathrm{d}x &= \frac{V_f}{V_m}\frac{\tau_i}{r_f E_m}(l_d^2 - x^2) - \frac{V_f E_f \sigma_{fo}}{V_m E_m E_c}(l_c/2 - l_d) \\ &-2\frac{V_f\tau_i}{\rho V_m E_m}l_d - \frac{r_f}{\rho V_m E_m}\left(\frac{b+d}{b}\sigma-\frac{d}{b}\sigma_{to}\right)-\frac{r_f V_f E_f\sigma_{fo}}{\rho V_m E_m E_c} \end{aligned} \tag{1.75}$$

Using Eqs. (1.74) and (1.75), the relative displacement between the fiber and matrix is given by the following equation:

$$\begin{aligned} v(x) = |w_f(x) - w_m(x)| &= \frac{1}{V_f E_f}\left(\frac{b+d}{b}\sigma-\frac{d}{b}\sigma_{to}\right) \\ &\times(l_d - x) - \frac{E_1\tau_i}{r_f V_m E_f E_m}(l_d^2 - x^2) \\ &+\frac{E_1\sigma_{fo}}{V_m E_m E_c}\left(\frac{l_c}{2}-l_d\right)+\frac{r_f E_1}{\rho V_f V_m E_f E_m}\left(\frac{b+d}{b}\sigma-\frac{d}{b}\sigma_{to}\right) \\ &+\frac{2E_1\tau_i}{\rho V_m E_m E_f}l_d + \frac{r_f E_1\sigma_{fo}}{\rho V_m E_m E_c} \end{aligned} \tag{1.76}$$

Substituting $w_f(x=0)$ and $v(x)$ into Eq. (1.67), it leads to the form of the following equation:

$$l_d = \frac{r_f}{2}\left(\frac{V_m E_m \sigma}{V_f E_c \tau_i} - \frac{1}{\rho}\right) - \sqrt{\left(\frac{r_f}{2\rho}\right)^2 + \frac{r_f V_m E_f E_m}{E_c \tau_i^2}\xi_d} \tag{1.77}$$

The initial interface debonding stress is obtained by substituting $l_d = 0$ into Eq. (1.77):

$$\sigma_d = \frac{V_f E_c \tau_i}{\rho V_m E_m}\left[1 + \sqrt{1 + 4\frac{V_m E_m E_f}{r_f E_c}\frac{\rho^2}{\tau_i^2}\xi_d}\right] \tag{1.78}$$

The interface completely debonding stress is obtained by substituting $l_d = l_c/2$ into Eq. (1.77):

$$\sigma_b = \frac{V_f E_c \tau_i}{\rho V_m E_m}\left[1 + \rho\frac{l_c}{r_f} + \sqrt{1 + 4\frac{V_m E_f E_m}{r_f E_c}\frac{\rho^2}{\tau_i^2}\xi_d}\right] \tag{1.79}$$

It can be found from Eq. (1.79) that the interface completely debonding stress depends upon the matrix cracking space l_c, the interface shear stress τ_i, and the interface debonded energy ξ_d. During the evolution of multiple matrix cracking and fiber/matrix interface debonding, the interface completely debonded when the interface debonded length occupied the entire matrix cracking space l_c. When $l_d(\sigma = \sigma_b) > l_{sat}/2$, the interface completely debonding stress σ_b is less than the matrix-cracking-saturation stress σ_{sat}; when $l_d(\sigma = \sigma_b) < l_{sat}/2$, the interface completely debonding stress σ_b is more than the matrix-cracking-saturation stress σ_{sat}.

1.3.2.4 Hysteresis Theories

After first loading to the fatigue maximum stress σ_{max}, the stress applied on the composite σ oscillates between fatigue maximum stress σ_{max} and fatigue minimum stress σ_{min} ($\sigma_{min} \le \sigma \le \sigma_{max}$, $\sigma_{min} > 0$). If matrix cracking and fiber/matrix interface debonding are present upon first loading, the stress–strain hysteresis loops would develop as a result of energy dissipation through frictional sliding between fiber and matrix during unloading and subsequent reloading. The shape, size, and location of the hysteresis loops depend on the interface debonding and sliding.

1.3.2.4.1 Cracking Mode 3 When $\sigma_d < \sigma_{max} < \sigma_b$, the interface partially debonds. The maximum stress σ_k at which the interface completely slides upon unloading and subsequent reloading is given by the following equation:

$$\begin{aligned}\frac{V_m E_m}{V_f E_c \tau_i}(\sigma_k + \sigma_{min})\left(1 + \frac{1}{2}\frac{d}{b}\frac{E_2}{V_m E_m} + \frac{1}{2}\frac{d}{b}\frac{E_2}{E_1}\right) - \frac{2}{\rho} \\ = \sqrt{\left(\frac{1}{2}\frac{E_f E_2}{E_1 E_c}\frac{d}{b}\frac{\sigma_k}{\tau_i} - \frac{1}{\rho}\right)^2 + \frac{V_m E_f E_m}{r_f E_1 \tau_i^2}\xi_d} \\ + \sqrt{\left(\frac{1}{2}\frac{E_2 E_f}{E_1 E_c}\frac{d}{b}\frac{\sigma_{min}}{\tau_i} - \frac{1}{\rho}\right)^2 + \frac{V_m E_f E_m}{r_f E_1 \tau_i^2}\xi_d}\end{aligned} \tag{1.80}$$

When $\sigma_{max} < \sigma_k$, interface counter slip length y upon unloading is affected by the interface debonding. The interface counter slip length y, upon completely unloading, is equal to the interface debonded length l_d. The fiber slides completely relative to the matrix within the interface debonded region upon unloading and subsequent reloading. When $\sigma_k < \sigma_{max} < \sigma_b$, the interface counter slip length y, upon completely unloading, is less than the interface debonded length l_d. The fiber slides partially relative to matrix within interface debonded region upon unloading and subsequent reloading.

When $\sigma_b < \sigma_{max}$, the interface debonds completely. The maximum stress σ_p, at which the interface completely slips upon unloading and subsequent reloading, can be described using the following equation:

$$\sigma_p = 2\frac{bV_f E_c}{bV_m E_m + dE_2}\frac{l_c}{r_f}\tau_i + \sigma_{min} \tag{1.81}$$

When $\sigma_b < \sigma_{max} < \sigma_p$, the interface counter slip length y upon completely unloading, is less than the half matrix crack space, $l_c/2$. The fiber slides partially relative to matrix within the interface debonded region upon unloading and subsequent reloading. When $\sigma_p < \sigma_{max}$, the interface counter slip length y upon completely unloading, is equal to the half matrix crack space, $l_c/2$. The fiber slides completely relative to matrix within interface debonded region during unloading and subsequent reloading.

Interface Slip Case 1 Upon unloading to σ ($\sigma_{min} < \sigma < \sigma_{max}$), the 0° ply of the unit cell can be divided into the interface debonded region and interface bonded region. The interface debonded region can be divided into the interface counter slip region ($x \in [0, y]$) and the interface slip region ($x \in [y, l_d]$). Upon unloading to the transition stress of σ_{tr_pu} ($\sigma_{tr\_pu} > \sigma_{min}$), the interface counter slip length y reaches the interface debonded length, l_d, i.e. $y(\sigma_{tr\_pu}) = l_d$:

$$\begin{aligned}
&\left(1+\frac{d}{b}\frac{E_2}{V_m E_m}\right)\left(1+\frac{d}{b}\frac{E_2}{E_1}\right)\left(\frac{V_m E_m}{V_f E_c \tau_i}\right)^2 (\sigma_{tr_pu})^2 \\
&\quad -2\frac{V_m E_m}{\rho V_f E_c \tau_i}\left(1+\frac{d}{b}\frac{E_2}{E_1}\right)\sigma_{tr_pu} \\
&\quad +4\frac{V_m E_m}{V_f E_c \tau_i}\frac{l_d}{r_f}\left(1+\frac{1}{2}\frac{d}{b}\frac{E_2}{V_m E_m}+\frac{1}{2}\frac{d}{b}\frac{E_2}{E_1}\right)\sigma_{tr_pu} \\
&\quad +4\left(\frac{l_d}{r_f}\right)^2 - 4\frac{l_d}{\rho r_f} - 4\frac{V_m E_f E_m}{r_f E_1 \tau_i^2}\xi_d = 0
\end{aligned} \tag{1.82}$$

When $\sigma > \sigma_{tr\_pu}$, the fiber axial stress distribution upon unloading, can be described using the following equation:

$$\begin{cases}
\sigma_f(x) = \frac{1}{V_f}\frac{b+d}{b}\sigma + \frac{2\tau_i}{r_f}x, & x \in (0, y) \\
\sigma_f(x) = \frac{1}{V_f}\frac{b+d}{b}\sigma + \frac{2\tau_i}{r_f}(2y - x), & x \in (y, l_d) \\
\sigma_f(x) = \sigma_{fo} + \left[\frac{1}{V_f}\frac{b+d}{b}\sigma + \frac{2\tau_i}{r_f}(2y - l_d) - \sigma_{fo}\right] & \\
\qquad \times \exp\left(-\rho\frac{x - l_d}{r_f}\right), & x \in (l_d, l_c/2)
\end{cases} \tag{1.83}$$

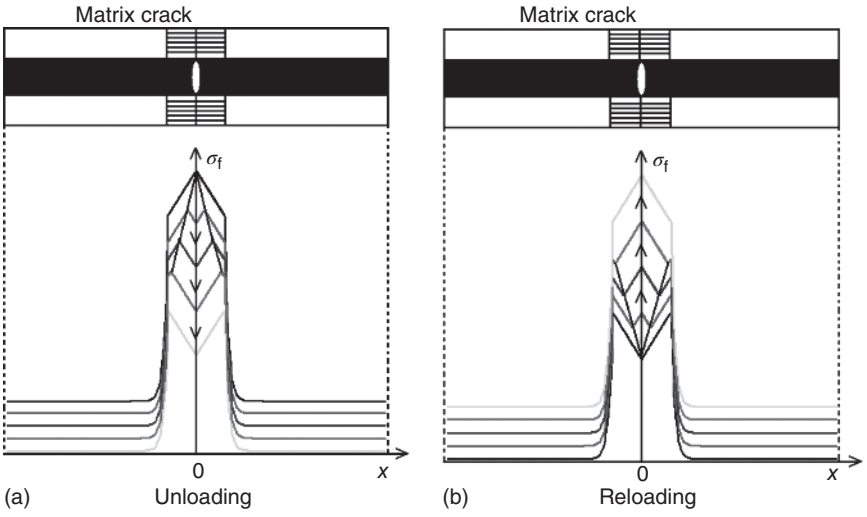

Figure 1.35 The fiber axial stress distribution for the interface slip Case 1 of matrix cracking mode 3 upon (a) unloading; and (b) reloading.

where

$$y=\frac{1}{2}\left\{l_d-\left[\frac{r_f}{2}\left(\frac{V_mE_m}{V_fE_c\tau_i}\sigma\left(1+\frac{1}{2}\frac{d}{b}\frac{E_2}{V_mE_m}+\frac{1}{2}\frac{d}{b}\frac{E_2}{E_1}\right)-\frac{1}{\rho}\right)\right.\right.$$
$$\left.\left.-\sqrt{\frac{1}{4}\left(\frac{1}{2}r_f\frac{E_2E_f}{E_1E_c}\frac{d}{b}\frac{\sigma}{\tau_i}-\frac{r_f}{\rho}\right)^2+\frac{r_fV_mE_fE_m}{E_1\tau_i^2}\xi_d}\right]\right\} \tag{1.84}$$

When $\sigma_{min}<\sigma<\sigma_{tr\_pu}$, the counter slip occurs over the entire interface debonded region, and the stress within the fiber are given by Eq. (1.83) by setting $y=l_d$. The fiber axial stress distribution upon unloading for this case is shown in Figure 1.35.

Upon reloading to σ ($\sigma_{min}<\sigma<\sigma_{max}$), fiber/matrix interface slip again occurs near the matrix crack plane over a distance of z, which denotes the interface new slip region. The interface debonded region can be divided into new slip region ($x\in[0,z]$), counter slip region ($x\in[z,y]$), and slip region ($x\in[y,l_d]$). Upon reloading to the transition stress of σ_{tr_pr} ($\sigma_{tr\_pr}<\sigma_{max}$), the interface new slip length of z reaches the interface debonded length l_d, i.e. $z(\sigma_{tr\_pr})=l_d$:

$$\left(1+\frac{d}{b}\frac{E_2}{V_mE_m}\right)\left(1+\frac{d}{b}\frac{E_2}{E_1}\right)\left(\frac{V_mE_m}{V_fE_c\tau_i}\right)^2(\sigma_{tr\_pr})^2$$
$$-2\frac{V_mE_m}{\rho V_fE_c\tau_i}\left(1+\frac{d}{b}\frac{E_2}{E_1}\right)\sigma_{tr\_pr}$$
$$-4\frac{V_mE_m}{V_fE_c\tau_i}\frac{l_d}{r_f}\left(1+\frac{1}{2}\frac{d}{b}\frac{E_2}{V_mE_m}+\frac{1}{2}\frac{d}{b}\frac{E_2}{E_1}\right)\sigma_{tr\_pr}$$
$$+4\left(\frac{l_d}{r_f}\right)^2+4\frac{l_d}{\rho r_f}-4\frac{V_mE_fE_m}{r_fE_1\tau_i^2}\xi_d=0 \tag{1.85}$$

When $\sigma < \sigma_{tr\_pr}$, the fiber axial stress distribution upon reloading can be described using the following equation:

$$\begin{cases} \sigma_f(x) = \frac{1}{V_f}\frac{b+d}{b}\sigma - \frac{2\tau_i}{r_f}x, & x \in (0, z) \\ \sigma_f(x) = \frac{1}{V_f}\frac{b+d}{b}\sigma + \frac{2\tau_i}{r_f}(x - 2z), & x \in (z, y) \\ \sigma_f(x) = \frac{1}{V_f}\frac{b+d}{b}\sigma - \frac{2\tau_i}{r_f}(x - 2y + 2z), & x \in (y, l_d) \\ \sigma_f(x) = \sigma_{fo} + \left[\frac{1}{V_f}\frac{b+d}{b}\sigma - \frac{2\tau_i}{r_f}(l_d - 2y + 2z) - \sigma_{fo}\right] & \\ \qquad \times \exp\left(-\rho\frac{x - l_d}{r_f}\right), & x \in (l_d, l_c/2) \end{cases} \tag{1.86}$$

where

$$z = y(\sigma_{min}) - \frac{1}{2}\left\{l_d - \left[\frac{r_f}{2}\left(\frac{V_m E_m \sigma}{V_f E_c \tau_i}\left(1 + \frac{1}{2}\frac{d}{b}\frac{E_2}{V_m E_m} + \frac{1}{2}\frac{d}{b}\frac{E_2}{E_1}\right) - \frac{1}{\rho}\right) - \sqrt{\frac{1}{4}\left(\frac{1}{2}\frac{r_f E_f E_2}{E_1 E_c}\frac{d}{b}\frac{\sigma}{\tau_i} - \frac{r_f}{\rho}\right)^2 + \frac{r_f V_m E_f E_m}{E_1 \tau_i^2}\xi_d}\right]\right\} \tag{1.87}$$

When $\sigma_{tr\_pr} < \sigma < \sigma_{max}$, new slip occurs over the entire interface debonded region, and the stress within the fiber are given by Eq. (1.86) by setting $z = l_d$. The fiber axial stress distribution upon reloading for this case is illustrated in Figure 1.35.

Interface Slip Case 2 When $\sigma_k < \sigma_{max} < \sigma_b$, the interface counter slip length y upon completely unloading is less than the interface debonded length l_d, i.e. $y(\sigma_{min}) < l_d$. The fiber axial stress distribution is given by Eq. (1.83), and the unloading interface counter slip length y is given by Eq. (1.84). The fiber axial stress distribution upon unloading for this case is illustrated in Figure 1.36. Upon reloading to σ_{max}, the interface new slip length of z is less than the interface debonded length l_d, $z(\sigma_{max}) < l_d$. The fiber axial stress distribution is given by Eq. (1.86), and the interface new slip length z is given by Eq. (1.87). The fiber axial stress distribution upon reloading for this case is illustrated in Figure 1.36.

Interface Slip Case 3 When $\sigma_b < \sigma_{max} < \sigma_p$, the fiber/matrix interface completely debonds. Upon completely unloading, the interface counter slip length y is less than the half matrix crack space $l_c/2$, i.e. $y(\sigma_{min}) < l_c/2$.

The fiber axial stress distribution upon unloading can be described using the following equation:

$$\begin{cases} \sigma_f(x) = \frac{1}{V_f}\frac{b+d}{b}\sigma + \frac{2\tau_i}{r_f}x, & x \in (0, y) \\ \sigma_f(x) = \frac{1}{V_f}\frac{b+d}{b}\sigma + \frac{2\tau_i}{r_f}(2y - x), & x \in (y, l_c/2) \end{cases} \tag{1.88}$$

where

$$y = \frac{r_f}{4\tau_i}\frac{V_m E_m}{V_f E_c}\left(1 + \frac{d}{b}\frac{E_2}{V_m E_m}\right)(\sigma_{max} - \sigma) \tag{1.89}$$

The fiber axial stress distribution upon unloading for this case is illustrated in Figure 1.37.

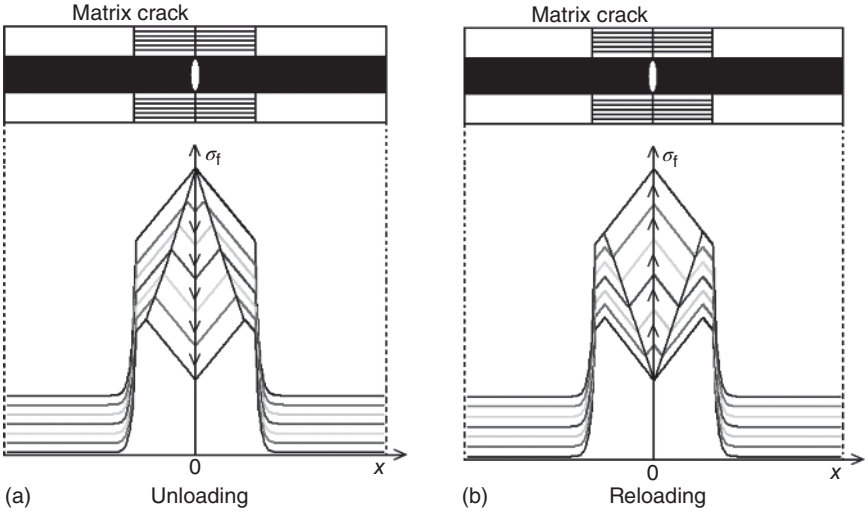

Figure 1.36 The fiber axial stress distribution for the interface slip Case 2 of matrix cracking mode 3 upon (a) unloading; and (b) reloading.

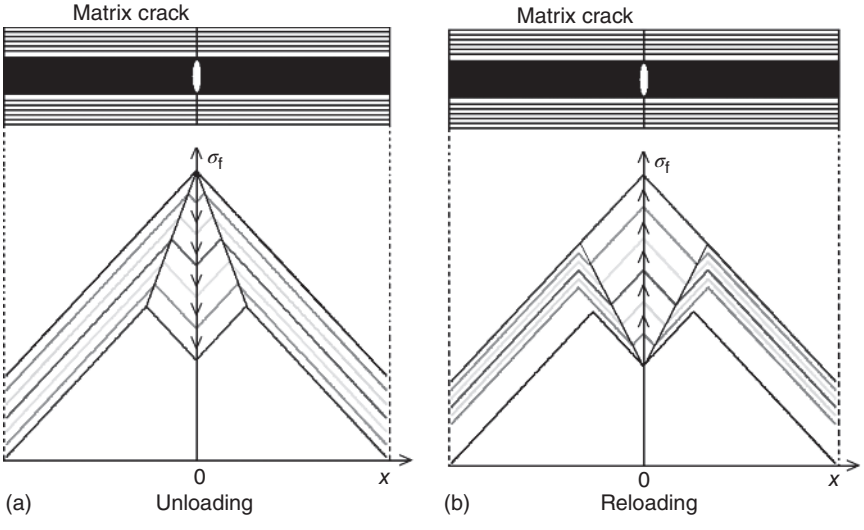

Figure 1.37 The fiber axial stress distribution for the interface slip Case 3 of matrix cracking mode 3 upon (a) unloading; and (b) reloading.

Upon reloading to σ_{max}, the interface new slip length z is less than the half matrix crack space $l_c/2$, i.e. $z(\sigma_{min}) < l_c/2$. The fiber axial stress distribution during reloading can be described using the following equation:

$$\begin{cases} \sigma_f(x) = \frac{1}{V_f}\frac{b+d}{b}\sigma - \frac{2\tau_i}{r_f}x, & x \in (0,z) \\ \sigma_f(x) = \frac{1}{V_f}\frac{b+d}{b}\sigma + \frac{2\tau_i}{r_f}(x-2z), & x \in (z,y) \\ \sigma_f(x) = \frac{1}{V_f}\frac{b+d}{b}\sigma - \frac{2\tau_i}{r_f}(x-2y+2z), & x \in (y,l_c/2) \end{cases} \tag{1.90}$$

where

$$z = y(\sigma_{\min}) - \frac{r_f}{4\tau_i}\frac{V_m E_m}{V_f E_c}\left(1 + \frac{d}{b}\frac{E_2}{V_m E_m}\right)(\sigma_{\max} - \sigma) \tag{1.91}$$

The fiber axial stress distribution upon reloading for this case is illustrated in Figure 1.37.

Interface Slip Case 4 When $\sigma_{\max} > \sigma_p$, the fiber/matrix interface completely debonds. Upon unloading to the transition stress of σ_{tr_fu} ($\sigma_{tr\_fu} > \sigma_{\min}$), the interface counter slip length y reaches the half matrix crack space of $l_c/2$:

$$\sigma_{tr\_pu} = \sigma_{\max} - 2\frac{bV_f E_c}{bV_m E_m + dE_2}\frac{l_c}{r_f}\tau_i \tag{1.92}$$

When $\sigma > \sigma_{tr\_fu}$, the unloading interface counter slip length y is less than the half matrix crack space $l_c/2$. The fiber axial stress distribution is given by Eq. (1.88), and the unloading interface counter slip length y is given by Eq. (1.89). When $\sigma_{\min} < \sigma < \sigma_{tr\_fu}$, the counter slip occurs over the entire matrix crack space, and the fiber axial stress distribution is given by Eq. (1.89) by setting $y = l_c/2$.

The fiber axial stress distribution upon unloading for this case is illustrated in Figure 1.38.

Upon reloading to the transition stress of σ_{tr_fr} ($\sigma_{tr\_fr} < \sigma_{\max}$), new slip length z reaches the half matrix crack space of $l_c/2$:

$$\sigma_{tr\_fr} = \sigma_{\min} + 2\frac{bV_f E_c}{bV_m E_m + dE_2}\frac{l_c}{r_f}\tau_i \tag{1.93}$$

When $\sigma < \sigma_{tr\_fr}$, the reloading interface new slip length z is less than the half matrix crack space $l_c/2$. The fiber axial stress distribution is given by Eq. (1.90),

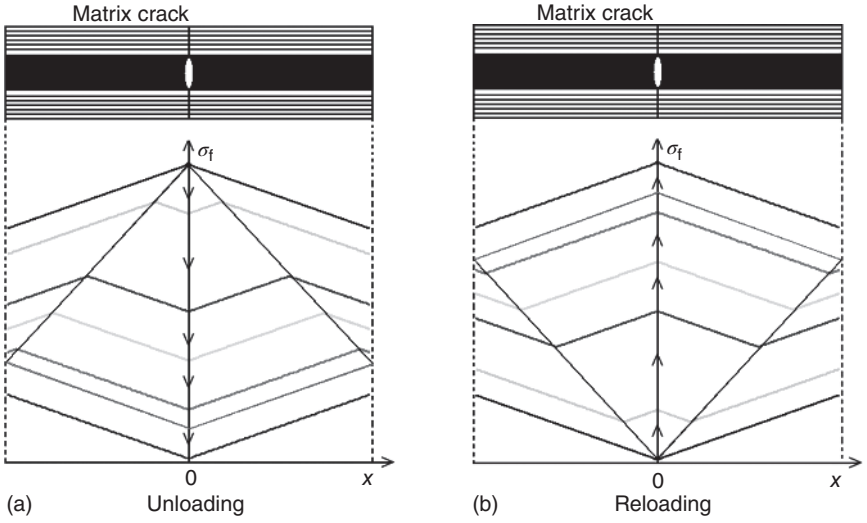

Figure 1.38 The fiber axial stress distribution for the interface slip Case 4 of matrix cracking mode 3 upon (a) unloading; and (b) reloading.

and the new slip length z is given by Eq. (1.91). When $\sigma_{tr\_fr} < \sigma < \sigma_{max}$, new slip length occurs over the entire matrix crack space, and the fiber axial stress distribution is given by Eq. (1.90) by setting $z = l_c/2$.

The fiber axial stress distribution upon reloading for this case is illustrated in Figure 1.38.

Stress–Strain Hysteresis Relationship When damage forms within the composite, the composite strain is determined from Eq. (1.94), which assumes that the composite strain is equivalent to the average strain in an undamaged fiber. The undamaged fiber is bridging a matrix crack.

$$\varepsilon_c = \frac{2}{E_f l_c}\int_{l_c/2}\sigma_f(x)\mathrm{d}x - (\alpha_c - \alpha_f)\Delta T \tag{1.94}$$

Substituting Eq. (1.83) into Eq. (1.94), the unloading stress–strain relationship for the interface partially debonding and fiber sliding partially relative to matrix can be described using the following equation:

$$\varepsilon_c = \frac{b+d}{b}\frac{\sigma}{V_f E_f} + 4\frac{\tau_i}{E_f}\frac{y^2}{r_f L} - 2\frac{\tau_i}{E_f}\frac{(2y - l_d)(2y - l_c + l_d)}{r_f l_c} - (\alpha_c - \alpha_f)\Delta T \tag{1.95}$$

Substituting Eq. (1.86) into Eq. (1.94), the reloading stress–strain relationship for the interface partially debonding and fiber sliding partially relative to matrix can be described using the following equation:

$$\begin{aligned}\varepsilon_c = {} & \frac{b+d}{b}\frac{\sigma}{V_f E_f} - 4\frac{\tau_i}{E_f}\frac{z^2}{r_f l_c} + \frac{4\tau_i}{E_f}\frac{(y-2z)^2}{r_f l_c} \\ & + 2\frac{\tau_i}{E_f}\frac{(l_d - 2y + 2z)(l_d + 2y - 2z - l_c)}{r_f l_c} - (\alpha_c - \alpha_f)\Delta T\end{aligned} \tag{1.96}$$

When the fiber completely slides relative to matrix upon unloading and subsequent reloading, the unloading stress–strain relationship is divided into two parts. When $\sigma > \sigma_{tr\_pu}$, the unloading strain is given by Eq. (1.95); when $\sigma < \sigma_{tr\_pu}$, the unloading strain is given by Eq. (1.95) by setting $y = l_d$. The reloading stress–strain relationship is divided into two parts too. When $\sigma < \sigma_{tr\_pr}$, the reloading strain is given by Eq. (1.96); when $\sigma > \sigma_{tr\_pr}$, the reloading strain is given by Eq. (1.96) by setting $z = l_d$.

Substituting Eq. (1.88) into Eq. (1.94), the unloading stress–strain relationship for the interface completely debonding and fiber partially sliding relative to matrix can be described using the following equation:

$$\varepsilon_c = \frac{b+d}{b}\frac{\sigma}{V_f E_f} + 4\frac{\tau_i}{E_f}\frac{y^2}{r_f l_c} - 2\frac{\tau_i}{E_f}\frac{(2y - l_c/2)^2}{r_f l_c} - (\alpha_c - \alpha_f)\Delta T \tag{1.97}$$

Substituting Eq. (1.90) into Eq. (1.94), the reloading stress–strain relationship for the interface complete debonding and fiber partially sliding relative to matrix

can be described using the following equation:

$$\varepsilon_c = \frac{b+d}{b}\frac{\sigma}{V_f E_f} - 4\frac{\tau_i}{E_f}\frac{z^2}{r_f l_c} + 4\frac{\tau_i}{E_f}\frac{(y-2z)^2}{r_f l_c} - 2\frac{\tau_i}{E_f}\frac{(l_c/2-2y+2z)^2}{r_f l_c} - (\alpha_c-\alpha_f)\Delta T \tag{1.98}$$

When the fiber completely slides relative to matrix upon unloading and subsequent reloading, the unloading stress–strain relationship is divided into two parts. When $\sigma > \sigma_{tr\_fu}$, the unloading strain is given by Eq. (1.98); when $\sigma < \sigma_{tr\_fu}$, the unloading strain is given by Eq. (1.98) by setting $y = l_c/2$. The reloading stress–strain relationship is divided into two parts too. When $\sigma < \sigma_{tr\_fr}$, the reloading strain is given by Eq. (1.99); when $\sigma > \sigma_{tr\_fr}$, the reloading strain is given by Eq. (1.99) by setting $z = l_c/2$.

1.3.2.4.2 Cracking Mode 5 For the cracking mode 5, the maximum stress σ_k at which the interface partially debonds and the fiber slides completely relative to matrix upon unloading and subsequent reloading can be described using the following equation:

$$\sigma_k = 2\frac{V_f E_c \tau_i}{\rho V_m E_m}\left[1+\sqrt{1+4\frac{V_m E_m E_f}{r_f E_c}\frac{\rho^2}{\tau_i^2}\xi_d}\right] - \sigma_{min} \tag{1.99}$$

The maximum stress σ_p at which interface completely debonds and the fiber slides completely relative to matrix upon unloading and can subsequent reloading be described using the following equation:

$$\sigma_p = 2\frac{V_f E_c}{V_m E_m}\frac{l_c}{r_f}\tau_i + \sigma_{min} \tag{1.100}$$

Interface Slip Case 1 When $\sigma_d < \sigma_{max} < \sigma_k$, upon unloading to the transition stress of σ_{tr_pu} ($\sigma_{tr\_pu} > \sigma_{min}$), the interface counter slip length y reaches the interface debonded length of l_d, i.e. $y(\sigma_{tr\_pu}) = l_d$:

$$\sigma_{tr\_fu} = 2\frac{V_f E_c \tau_i}{\rho V_m E_m}\left[1+\sqrt{1+4\frac{V_m E_m E_f}{r_f E_c}\frac{\rho^2}{\tau_i^2}\xi_d}\right] - \sigma_{max} \tag{1.101}$$

When $\sigma > \sigma_{tr\_pu}$, the fiber axial stress distribution upon unloading can be described using the following equation:

$$\begin{cases} \sigma_f(x) = \frac{1}{V_f}\left(\frac{b+d}{b}\sigma - \frac{d}{b}\sigma_{to}\right) + \frac{2\tau_i}{r_f}x, & x \in (0, y) \\ \sigma_f(x) = \frac{1}{V_f}\left(\frac{b+d}{b}\sigma - \frac{d}{b}\sigma_{to}\right) + \frac{2\tau_i}{r_f}(2y-x), & x \in (y, l_d) \\ \sigma_f(x) = \sigma_{fo} + \left[\frac{1}{V_f}\left(\frac{b+d}{b}\sigma - \frac{d}{b}\sigma_{to}\right) + \frac{2\tau_i}{r_f}(2y-l_d) - \sigma_{fo}\right] \\ \qquad \times \exp\left(-\rho\frac{x-l_d}{r_f}\right), & x \in (l_d, l_c/2) \end{cases} \tag{1.102}$$

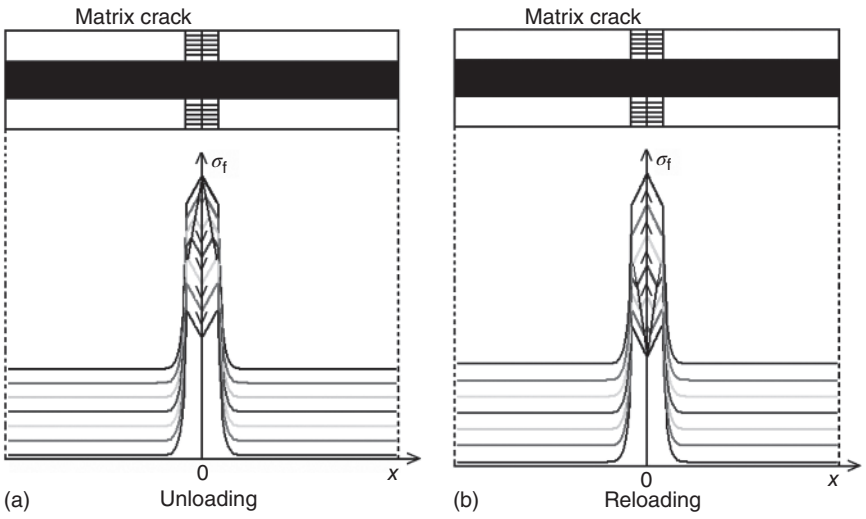

Figure 1.39 The fiber axial stress distribution for the interface slip Case 1 of matrix cracking mode 5 upon (a) unloading; and (b) reloading.

where

$$y=\frac{1}{2}\left\{l_{\mathrm{d}}-\left[\frac{r_{\mathrm{f}}}{2}\left(\frac{V_{\mathrm{m}}E_{\mathrm{m}}\sigma}{V_{\mathrm{f}}E_{\mathrm{c}}\tau_{\mathrm{i}}}-\frac{1}{\rho}\right)-\sqrt{\left(\frac{r_{\mathrm{f}}}{2\rho}\right)^{2}+\frac{r_{\mathrm{f}}V_{\mathrm{m}}E_{\mathrm{m}}E_{\mathrm{f}}}{E_{\mathrm{c}}\tau_{\mathrm{i}}^{2}}\xi_{\mathrm{d}}}\right]\right\} \tag{1.103}$$

When $\sigma_{\min}<\sigma<\sigma_{\mathrm{tr\_pu}}$, the unloading interface counter slip occurs over the entire interface debonded region, and the stress within the fiber are given by Eq. (1.102) by setting $y=l_{\mathrm{d}}$. The fiber axial stress distribution upon unloading for this case is illustrated in Figure 1.39.

When reloading to the transition stress of $\sigma_{\mathrm{tr\_pr}}(\sigma_{\mathrm{tr\_pr}}<\sigma_{\max})$, the interface new slip length z reaches the interface debonded length l_{d}, i.e. $z(\sigma_{\mathrm{tr\_pr}})=l_{\mathrm{d}}$:

$$\sigma_{\mathrm{tr\_pr}}=2\sigma_{\max}+\sigma_{\min}-2\frac{V_{\mathrm{f}}E_{\mathrm{c}}\tau_{\mathrm{i}}}{\rho V_{\mathrm{m}}E_{\mathrm{m}}}\left[1+\sqrt{1+4\frac{V_{\mathrm{m}}E_{\mathrm{m}}E_{\mathrm{f}}}{r_{\mathrm{f}}E_{\mathrm{c}}}\frac{\rho^{2}}{\tau_{\mathrm{i}}^{2}}\xi_{\mathrm{d}}}\right] \tag{1.104}$$

When $\sigma<\sigma_{\mathrm{tr\_pr}}$, the fiber axial stress distribution during reloading can be described using the following equation:

$$\begin{cases}\sigma_{\mathrm{f}}(x)=\frac{1}{V_{\mathrm{f}}}\left(\frac{b+d}{b}\sigma-\frac{d}{b}\sigma_{\mathrm{to}}\right)-\frac{2\tau_{\mathrm{i}}}{r_{\mathrm{f}}}x, & x\in(0,z)\\ \sigma_{\mathrm{f}}(x)=\frac{1}{V_{\mathrm{f}}}\left(\frac{b+d}{b}\sigma-\frac{d}{b}\sigma_{\mathrm{to}}\right)+\frac{2\tau_{\mathrm{i}}}{r_{\mathrm{f}}}(x-2z), & x\in(z,y)\\ \sigma_{\mathrm{f}}(x)=\frac{1}{V_{\mathrm{f}}}\left(\frac{b+d}{b}\sigma-\frac{d}{b}\sigma_{\mathrm{to}}\right)-\frac{2\tau_{\mathrm{i}}}{r_{\mathrm{f}}}(x-2y+2z), & x\in(y,l_{\mathrm{d}})\\ \sigma_{\mathrm{f}}(x)=\sigma_{\mathrm{fo}}+\left[\frac{1}{V_{\mathrm{f}}}\left(\frac{b+d}{b}\sigma-\frac{d}{b}\sigma_{\mathrm{to}}\right)-\frac{2\tau_{\mathrm{i}}}{r_{\mathrm{f}}}(l_{\mathrm{d}}-2y+2z)-\sigma_{\mathrm{fo}}\right]\\ \qquad\times\exp\left(-\rho\frac{x-l_{\mathrm{d}}}{r_{\mathrm{f}}}\right), & x\in\left(l_{\mathrm{d}},\frac{l_{\mathrm{c}}}{2}\right)\end{cases} \tag{1.105}$$

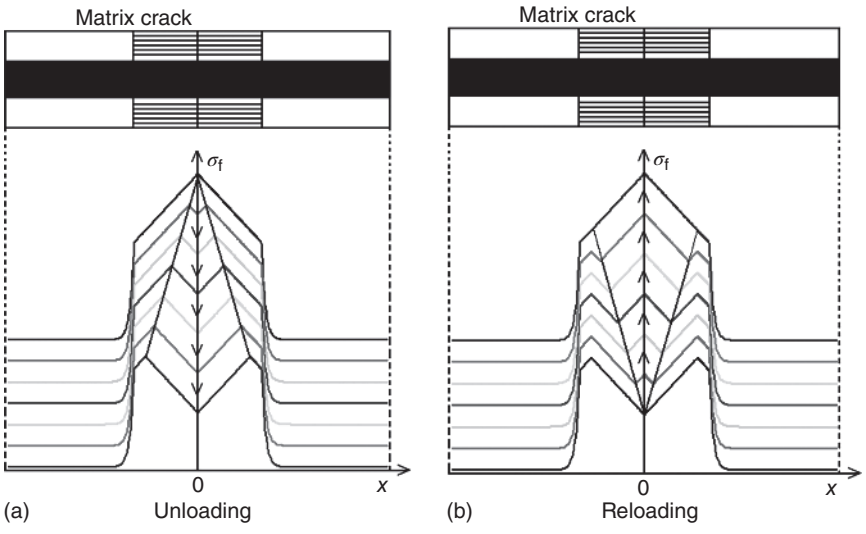

Figure 1.40 The fiber axial stress distribution for the interface slip Case 2 of matrix cracking mode 5 upon (a) unloading; and (b) reloading.

where

$$z = y - \frac{1}{2}\left\{ l_d - \left[\frac{r_f}{2}\left(\frac{V_m E_m \sigma}{V_f E_c \tau_i} - \frac{1}{\rho} \right) - \sqrt{\left(\frac{r_f}{2\rho} \right)^2 + \frac{r_f V_m E_m E_f}{E_c \tau_i^2} \xi_d} \right] \right\} \tag{1.106}$$

When $\sigma_{tr\_pr} < \sigma < \sigma_{max}$, the interface new slip length occupies over the entire interface debonded length, and the stress within the fiber are given by Eq. (1.105) by setting $z = l_d$. The fiber axial stress distribution upon reloading for this case is illustrated in Figure 1.39.

Case 2 When $\sigma_k < \sigma_{max} < \sigma_b$, the interface counter slip length y upon completely unloading is less than the interface debonded length l_d, $y(\sigma_{min}) < l_d$. The fiber axial stress distribution is given by Eq. (1.102), and the unloading interface counter slip length y is given by Eq. (1.103). The fiber axial stress distribution upon unloading for this case is illustrated in Figure 1.40. Upon reloading to σ_{max}, the interface new slip length z is less than the interface debonded length l_d, i.e. $z(\sigma_{max}) < l_d$. The fiber axial stress distribution is given by Eq. (1.105), and the interface new slip length z is given by Eq. (1.106). The fiber axial stress distribution upon reloading for this case is illustrated in Figure 1.40.

Case 3 When $\sigma_b < \sigma_{max} < \sigma_p$, the interface completely debonds. Upon completely unloading, the interface counter slip length y is less than the half matrix space $l_c/2$, i.e. $y(\sigma_{min}) < l_c/2$.

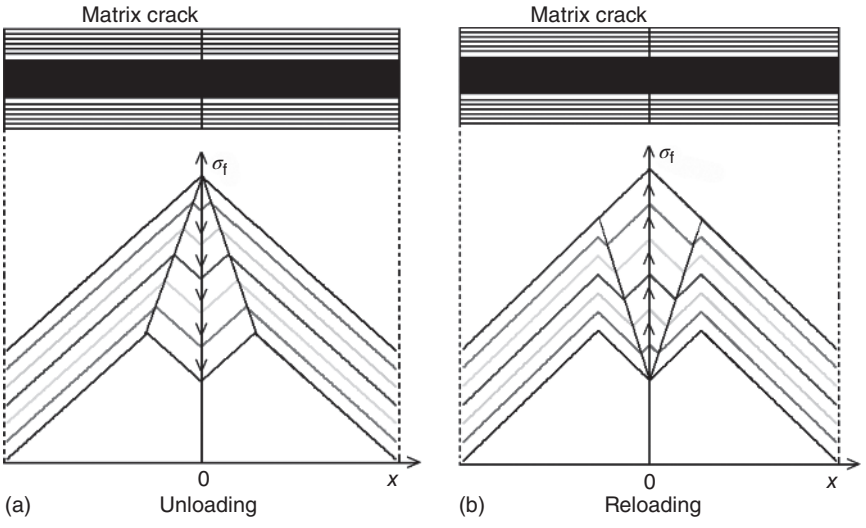

Figure 1.41 The fiber axial stress distribution for the interface slip Case 3 of matrix cracking mode 5 upon (a) unloading; and (b) reloading.

The fiber axial stress distribution upon unloading can be described using the following equation:

$$\begin{cases} \sigma_f(x) = \frac{1}{V_f}\left(\frac{b+d}{b}\sigma - \frac{d}{b}\sigma_{to}\right) + \frac{2\tau_i}{r_f}x, & x \in (0, y) \\ \sigma_f(x) = \frac{1}{V_f}\left(\frac{b+d}{b}\sigma - \frac{d}{b}\sigma_{to}\right) + \frac{2\tau_i}{r_f}(2y - x), & x \in (y, l_c/2) \end{cases} \tag{1.107}$$

where

$$y = \frac{r_f}{4\tau_i}\frac{V_m E_m}{V_f E_c}(\sigma_{max} - \sigma) \tag{1.108}$$

The fiber axial stress distribution upon unloading for this case is illustrated in Figure 1.41.

Upon reloading to σ_{max}, the interface new slip length z is less than the half matrix crack space $l_c/2$, $z(\sigma_{min}) < l_c/2$. The fiber axial stress distribution upon reloading can be described using the following equation:

$$\begin{cases} \sigma_f(x) = \frac{1}{V_f}\left(\frac{b+d}{b}\sigma - \frac{d}{b}\sigma_{to}\right) - \frac{2\tau_i}{r_f}x, & x \in (0, z) \\ \sigma_f(x) = \frac{1}{V_f}\left(\frac{b+d}{b}\sigma - \frac{d}{b}\sigma_{to}\right) + \frac{2\tau_i}{r_f}(x - 2z), & x \in (z, y) \\ \sigma_f(x) = \frac{1}{V_f}\left(\frac{b+d}{b}\sigma - \frac{d}{b}\sigma_{to}\right) - \frac{2\tau_i}{r_f}(x - 2y + 2z), & x \in (y, l_c/2) \end{cases} \tag{1.109}$$

where

$$z = y(\sigma_{min}) - \frac{r_f}{4\tau_i}\frac{V_m E_m}{V_f E_c}(\sigma_{max} - \sigma) \tag{1.110}$$

The fiber axial stress distribution upon reloading for this case is illustrated in Figure 1.41.

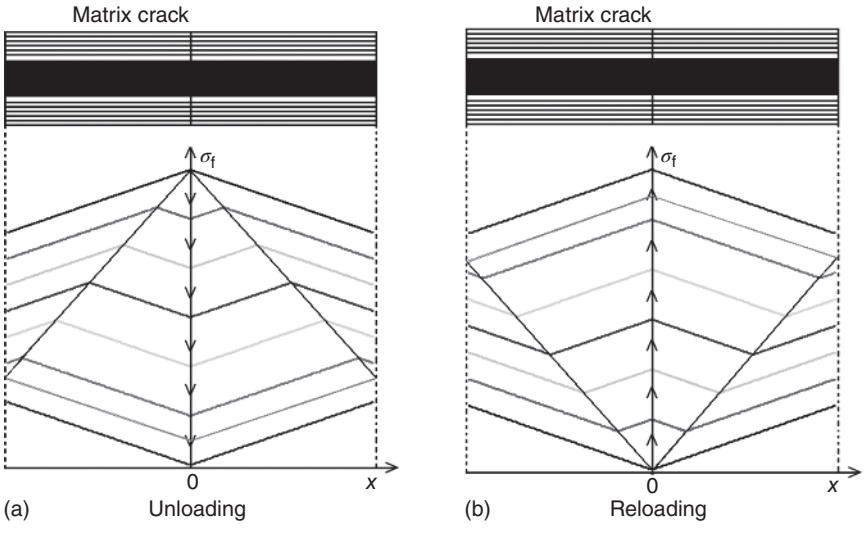

Figure 1.42 The fiber axial stress distribution for the interface slip Case 4 of matrix cracking mode 5 upon (a) unloading; and (b) reloading.

Case 4 When $\sigma_{max} > \sigma_p$, the interface completely debonds. Upon unloading to the transition stress of $\sigma_{tr\_fu}(\sigma_{tr\_fu} > \sigma_{min})$, the interface counter slip length y reaches the half matrix crack space $l_c/2$:

$$\sigma_{tr\_fu} = \sigma_{max} - 2\frac{V_f E_c}{V_m E_m}\frac{l_c}{r_f}\tau_i \tag{1.111}$$

When $\sigma > \sigma_{tr\_fu}$, the interface counter slip length y is less than the half matrix crack space $l_c/2$. The fiber axial stress distribution is given by Eq. (1.107), and the interface counter slip length y is given by Eq. (1.108). When $\sigma_{min} < \sigma < \sigma_{tr\_fu}$, the counter slip occurs over the entire matrix crack space, and the fiber axial stress distribution is given by Eq. (1.108) by setting $y = l_c/2$. The fiber axial stress distribution upon unloading for this case is illustrated in Figure 1.42.

Upon reloading to the transition stress of $\sigma_{tr\_fr}(\sigma_{tr\_fr} < \sigma_{max})$, new slip length z reaches the half matrix crack space $l_c/2$:

$$\sigma_{tr\_fr} = \sigma_{min} + 2\frac{V_f E_c}{V_m E_m}\frac{l_c}{r_f}\tau_i \tag{1.112}$$

When $\sigma < \sigma_{tr\_fr}$, new slip length z is less than the half matrix crack space $l_c/2$. The fiber axial stress distribution is given by Eq. (1.109), and the new slip length z is given by Eq. (1.110). When $\sigma_{tr\_fr} < \sigma < \sigma_{max}$, new slip length occurs over the entire matrix crack space, and the fiber axial stress distribution is given by Eq. (1.109) by setting $z = l_c/2$. The axial stress distribution during reloading for this case is illustrated in Figure 1.42.

Stress–Strain Hysteresis Relationship Substituting Eq. (1.102) into Eq. (1.94), the unloading stress–strain relationship for the interface partially debonding and

fiber sliding partially relative to matrix can be described using the following equation:

$$\varepsilon_c = \frac{b+d}{b}\frac{1}{V_f E_f}\left(\sigma - \frac{d}{b+d}\sigma_{to}\right) + 4\frac{\tau_i}{E_f}\frac{y^2}{r_f l_c} - 2\frac{\tau_i}{E_f}\frac{(2y-l_d)(2y+l_d-l_c)}{r_f l_c} - (\alpha_c - \alpha_f)\Delta T \quad (1.113)$$

Substituting Eq. (1.105) into Eq. (1.94), the reloading stress–strain relationship for the interface partially debonding and fiber sliding partially relative to matrix can be described using the following equation:

$$\varepsilon_c = \frac{b+d}{b}\frac{1}{V_f E_f}\left(\sigma - \frac{d}{b+d}\sigma_{to}\right) - 4\frac{\tau_i}{E_f}\frac{z^2}{r_f l_c} + \frac{4\tau_i}{E_f} + 2\frac{\tau_i}{E_f}\frac{(l_d-2y+2z)(l_d+2y-2z-l_c)}{r_f l_c} - (\alpha_c - \alpha_f)\Delta T \quad (1.114)$$

When the fiber completely slides relative to matrix upon unloading/reloading, the unloading stress–strain relationship is divided into two parts. When $\sigma > \sigma_{tr\_pu}$, the unloading strain is given by Eq. (1.113); when $\sigma < \sigma_{tr\_pu}$, the unloading strain is given by Eq. (1.113) by setting $y = l_d$. The reloading stress–strain relationship is divided into two parts too. When $\sigma < \sigma_{tr\_pr}$, the reloading strain is given by Eq. (1.114); when $\sigma > \sigma_{tr\_pr}$, the reloading strain is given by Eq. (1.114) by setting $z = l_d$.

Substituting Eq. (1.107) into Eq. (1.94), the unloading stress–strain relationship for the interface completely debonding and fiber partially sliding relative to matrix can be described using the following equation:

$$\varepsilon_c = \frac{b+d}{b}\frac{1}{V_f E_f}\left(\sigma - \frac{d}{b+d}\sigma_{to}\right) + 4\frac{\tau_i}{E_f}\frac{y^2}{r_f l_c} - 2\frac{\tau_i}{E_f}\frac{(2y-l_c/2)^2}{r_f l_c} - (\alpha_c - \alpha_f)\Delta T \quad (1.115)$$

Substituting Eq. (1.109) into Eq. (1.94), the reloading stress–strain relationship for interface completely debonding and fiber partially sliding relative to matrix can be described using the following equation:

$$\varepsilon_c = \frac{b+d}{b}\frac{1}{V_f E_f}\left(\sigma - \frac{d}{b+d}\sigma_{to}\right) - 4\frac{\tau_i}{E_f}\frac{z^2}{r_f l_c} + 4\frac{\tau_i}{E_f}\frac{(y-2z)^2}{r_f l_c} - 2\frac{\tau_i}{E_f}\frac{(l_c/2-2y+2z)^2}{r_f l_c} - (\alpha_c - \alpha_f)\Delta T \quad (1.116)$$

When the fiber completely slides relative to matrix upon unloading and subsequent reloading, the unloading stress–strain relationship is divided into two parts. When $\sigma > \sigma_{tr\_fu}$, the unloading strain is given by Eq. (1.115); when $\sigma < \sigma_{tr\_fu}$, the unloading strain is given by Eq. (1.115) by setting $y = l_c/2$. The reloading stress–strain relationship is divided into two parts too. When $\sigma < \sigma_{tr\_fr}$, the reloading strain is given by Eq. (1.116); when $\sigma > \sigma_{tr\_fr}$, the reloading strain is given by Eq. (1.116) by setting $z = l_c/2$.

1.3.3 Results and Discussions

Considering the effect of multiple matrix cracking modes on hysteresis loops of 2D CMCs, the unloading and reloading strains of the composite are presented in Eqs. (1.117a) and (1.117b):

$$(\varepsilon_u)_c = \eta(\varepsilon_{cu})_3 + (1-\eta)(\varepsilon_{cu})_5 \tag{1.117a}$$

$$(\varepsilon_r)_c = \eta(\varepsilon_{cr})_3 + (1-\eta)(\varepsilon_{cr})_5 \tag{1.117b}$$

where $(\varepsilon_u)_c$ and $(\varepsilon_r)_c$ denote the unloading and reloading strain of the composite, respectively; $(\varepsilon_{cu})_3$ and $(\varepsilon_{cr})_3$ denote the unloading and reloading strain of the matrix cracking mode 3, respectively; $(\varepsilon_{cu})_5$ and $(\varepsilon_{cr})_5$ denote the unloading and reloading strain of the matrix cracking mode 5, respectively; and η is the damage parameter determined by the composite's damage condition, i.e. the proportion of matrix cracking mode 3 in the entire of matrix cracking modes of the composite, $\eta \in [0,1]$.

Under cyclic loading and unloading, the material properties, i.e. fiber volume content, peak stress; damage state, i.e. matrix crack spacing and matrix cracking mode proportion, interface properties; i.e. interface shear stress and interface debonded energy; and interface wear, would affect the shape, location, and area of the hysteresis loops of cross-ply and 2D woven CMCs. The effect of these factors on interface slip and hysteresis loops of matrix cracking mode 3 and mode 5 and 2D SiC/SiC composite are analyzed.

1.3.3.1 Effect of Fiber Volume Fraction on the Interface Sliding and Fatigue Hysteresis Loops

The effect of fiber volume content, i.e. $V_f = 30\%$ and 40%, on the fatigue hysteresis loops and interface slip of matrix cracking mode 3 and mode 5 is shown in Figure 1.43.

For the matrix cracking mode 3, when the fiber volume fraction is $V_f = 30\%$, the fatigue hysteresis loops correspond to the interface slip Case 4, i.e. the interface completely debonding and the fiber sliding completely relative to the matrix in the interface debonded region. Upon unloading, the interface counter slip length approaches to the matrix crack spacing at the unloading transition stress of $\sigma_{tr\_fu} = 36\,\text{MPa}$, i.e. $2y(\sigma_{tr\_fu} = 36\,\text{MPa})/l_c = 1$; and upon reloading to the transition stress of $\sigma_{tr\_fr} = 144\,\text{MPa}$, the interface new slip length approaches to the matrix crack spacing, i.e. $2z(\sigma_{tr\_fr} = 144\,\text{MPa})/l_c = 1$, as shown in Figure 1.43b. When the fiber volume fraction is $V_f = 40\%$, the fatigue hysteresis loops correspond to the interface slip Case 2, i.e. the interface partially debonding and the fiber sliding partially relative to the matrix in the interface debonded region. Upon completely unloading, the interface counter slip length approaches to 81.8% of the interface debonded length, i.e. $y(\sigma_{min})/l_d = 81.8\%$. Upon reloading to the peak stress, the interface new slip length approaches to 81.8% of the interface debonded length, i.e. $z(\sigma_{max})/l_d = 81.8\%$, as shown in Figure 1.43b.

For the matrix cracking mode 5, when the fiber volume fraction is $V_f = 30\%$, the fatigue hysteresis loops correspond to the interface slip Case 1, i.e. the

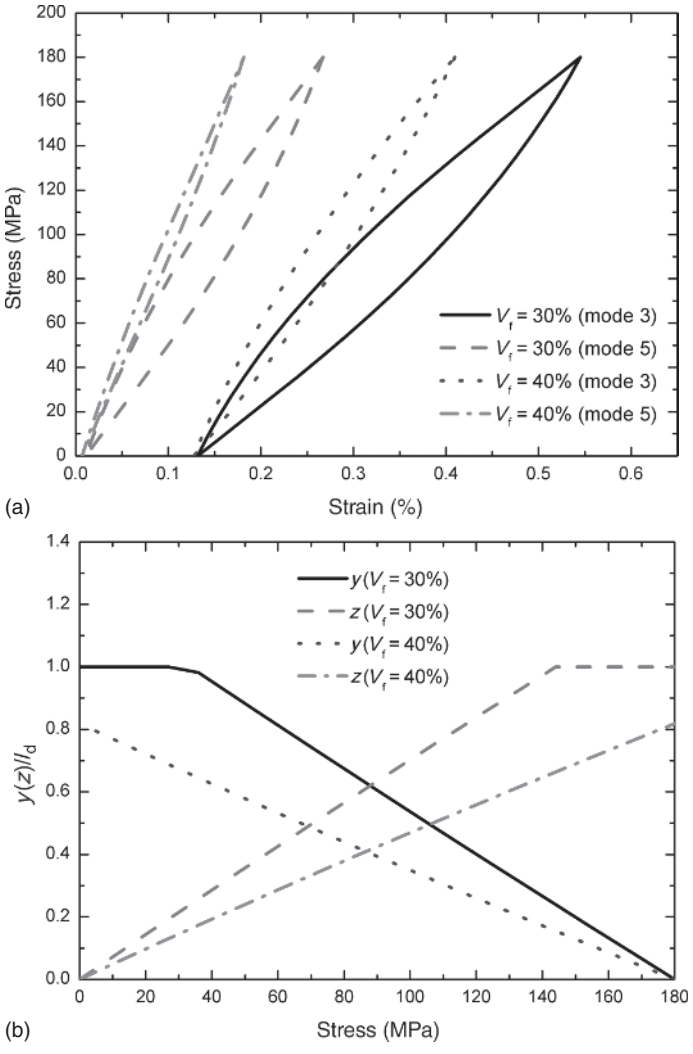

Figure 1.43 (a) The fatigue hysteresis loops of matrix cracking mode 3 and mode 5; (b) the interface slip lengths, i.e. y/l_d and z/l_d, of matrix cracking mode 3; and (c) the interface slip lengths, i.e. y/l_d and z/l_d, of matrix cracking mode 5 for different fiber volume fraction.

interface partially debonding and the fiber sliding completely relative to the matrix in the interface debonded region. Upon unloading, the interface counter slip length approaches to the interface debonded length at the transition stress of $\sigma_{tr\_pu} = 27\,\text{MPa}$, i.e. $y(\sigma_{tr\_pu} = 27\,\text{MPa})/l_d = 1$; and upon reloading to the transition stress of $\sigma_{tr\_pr} = 153\,\text{MPa}$, the interface new slip length approaches to the interface debonded length, i.e. $z(\sigma_{tr\_pr} = 153\,\text{MPa})/l_d = 1$, as shown in Figure 1.43c. When the fiber volume fraction is $V_f = 40\%$, the fatigue hysteresis loops correspond to the interface slip Case 1, i.e. the interface partially debonding and the fiber sliding completely relative to the matrix in the interface

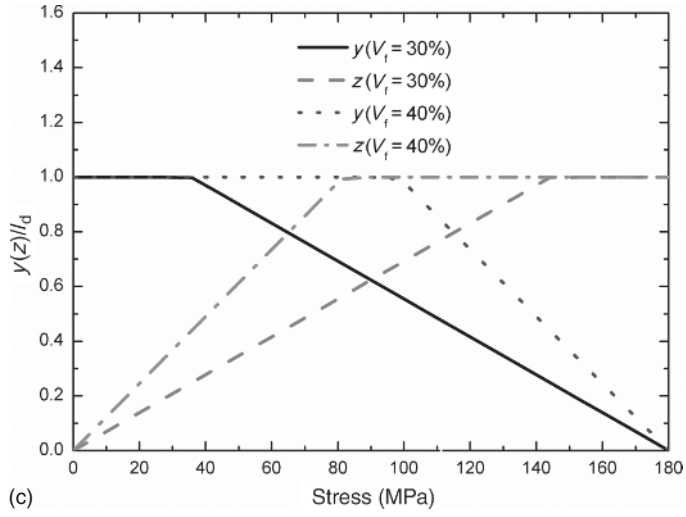

Figure 1.43 (*Continued*)

debonded region. Upon unloading, the interface counter slip length approaches to the interface debonded length at the transition stress of $\sigma_{tr\_pu} = 90$ MPa, i.e. $y(\sigma_{tr\_pu})/l_d = 1$; and upon reloading to the transition stress of $\sigma_{tr\_pr} = 90$ MPa, the interface new slip length approaches to the interface debonded length, i.e. $z(\sigma_{tr\_pr})/l_d = 1$, as shown in Figure 1.43c.

With increasing fiber volume fraction, the peak strain, residual strain, and hysteresis loops area decrease, and the hysteresis modulus increases, as shown in Figure 1.43a.

1.3.3.2 Effect of Fatigue Peak Stress on the Interface Sliding and Fatigue Hysteresis Loops

The effect of fatigue peak stress, i.e. $\sigma_{max} = 180$ and 200 MPa, on the fatigue hysteresis loops and the interface slip of matrix cracking mode 3 and mode 5 is shown in Figure 1.44.

For the matrix cracking mode 3, when the fatigue peak stress is $\sigma_{max} = 180$ MPa, the fatigue hysteresis loops correspond to the interface slip Case 2, i.e. the interface partially debonding and the fiber sliding partially relative to the matrix in the interface debonded region. Upon completely unloading, the interface counter slip length approaches to 82% of the interface debonded length, i.e. $y(\sigma_{min})/l_d = 83.2\%$; and upon reloading to the peak stress, the interface new slip length approaches to 83.2% of the interface debonded length, i.e. $z(\sigma_{max})/l_d = 83.2\%$, as shown in Figure 1.44b. When the fatigue peak stress is $\sigma_{max} = 200$ MPa, the fatigue hysteresis loops correspond to the interface slip Case 2, i.e. the interface partially debonding and the fiber sliding partially relative to the matrix in the interface debonded region. Upon completely unloading, the interface counter slip length approaches to 92% of the interface debonded length, i.e. $y(\sigma_{min})/l_d = 92\%$. Upon reloading to peak stress, the interface new slip length approaches to 92% of the interface debonded length, i.e. $z(\sigma_{max})/l_d = 92\%$, as shown in Figure 1.44b.

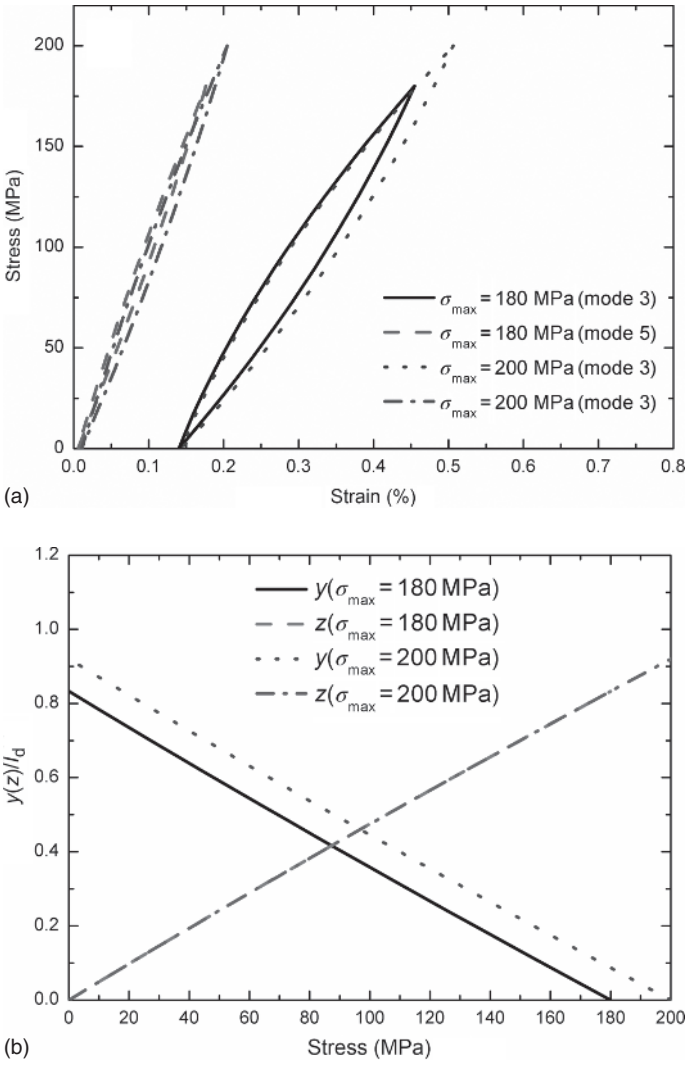

Figure 1.44 (a) The fatigue hysteresis loops of matrix cracking mode 3 and mode 5; (b) the interface slip lengths, i.e. y/l_d and z/l_d, of matrix cracking mode 3; and (c) the interface slip lengths, i.e. y/l_d and z/l_d, of matrix cracking mode 5 for different fatigue peak stresses.

For the matrix cracking mode 5, when the fatigue peak stress is $\sigma_{max} = 180$ MPa, the fatigue hysteresis loops correspond to the interface slip Case 1, i.e. the interface partially debonding and the fiber sliding completely relative to the matrix in the interface debonded region. Upon unloading, the interface counter slip length approaches to the interface debonded length at the transition stress of $\sigma_{tr\_pu} = 54$ MPa, i.e. $y(\sigma_{tr\_pu})/l_d = 1$; and upon reloading to the transition stress of $\sigma_{tr\_pr} = 126$ MPa, the interface new slip length approaches to the interface debonded length, i.e. $z(\sigma_{tr\_pr})/l_d = 1$, as shown in Figure 1.44c. When the fatigue peak stress is $\sigma_{max} = 200$ MPa, the fatigue hysteresis loops correspond

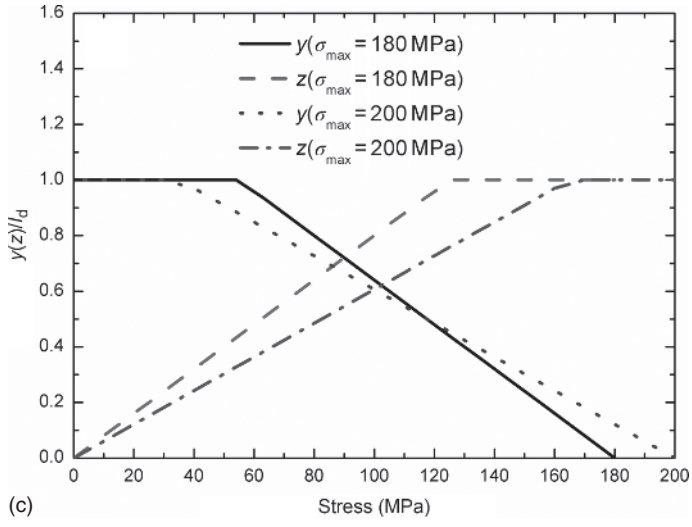

Figure 1.44 (*Continued*)

to the interface slip Case 1, i.e. the interface partially debonding and the fiber sliding completely relative to the matrix in the interface debonded region. Upon unloading, the interface counter slip length approaches to the interface debonded length at the transition stress of $\sigma_{tr\_pu} = 30$ MPa, i.e. $y(\sigma_{tr\_pu})/l_d = 1$; and upon reloading to the transition stress of $\sigma_{tr\_pr} = 170$ MPa, the interface new slip length approaches to the interface debonded length, i.e. $z(\sigma_{tr\_pr})/l_d = 1$, as shown in Figure 1.44c.

With increasing peak stress, the fatigue peak strain, residual strain, and fatigue hysteresis loops area increase, and the fatigue hysteresis modulus decreases, as shown in Figure 1.44a.

1.3.3.3 Effect of Matrix Crack Spacing on the Interface Sliding and Fatigue Hysteresis Loops

The effect of matrix crack spacing, i.e. $l_c = 20r_f$ and $30r_f$, on the fatigue hysteresis loops and the interface slip of matrix cracking mode 3 and mode 5 is shown in Figure 1.45.

For the matrix cracking mode 3, when the matrix crack spacing is $l_c = 20r_f$, the fatigue hysteresis loops correspond to the interface slip Case 2, i.e. the interface partially debonding and the fiber sliding partially relative to the matrix in the interface debonded region. Upon completely unloading, the interface counter slip length approaches to 83.2% of the matrix crack spacing of $2y(\sigma_{min})/l_c = 83.2\%$; and upon reloading to peak stress, the interface new slip length also approaches to 83.2% of the matrix crack spacing of $2z(\sigma_{max})/l_c = 83.2\%$, as shown in Figure 1.45b. When the matrix crack spacing is $l_c = 30r_f$, the fatigue hysteresis loops correspond to the interface slip Case 2, i.e. the interface partially debonding and the fiber sliding partially relative to the matrix in the interface debonded region. Upon completely unloading, the interface counter slip length approaches to 67.3% of the matrix crack spacing, i.e. $2y(\sigma_{min})/l_c = 67.3\%$; and upon reloading

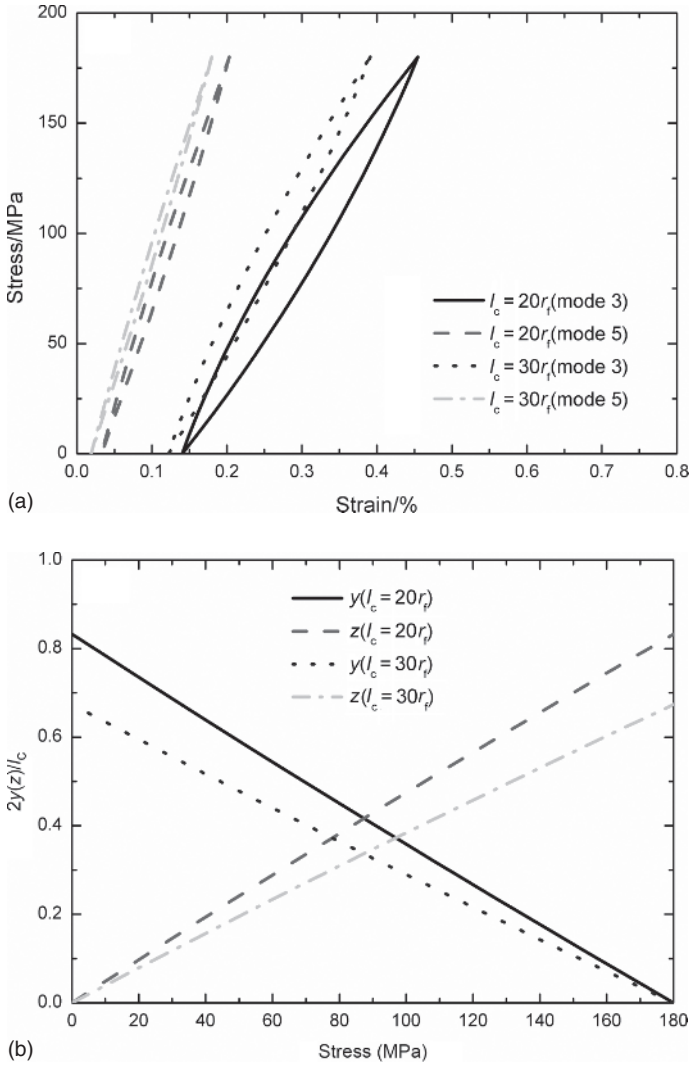

Figure 1.45 (a) The fatigue hysteresis loops of matrix cracking mode 3 and mode 5; (b) the interface slip lengths, i.e. y/l_d and z/l_d, of matrix cracking mode 3; and (c) the interface slip lengths, i.e. y/l_d and z/l_d, of matrix cracking mode 5 for different matrix crack spacing.

to peak stress, the interface new slip length also approaches to 67.3% of the matrix crack spacing, i.e. $2z(\sigma_{max})/l_c = 67.3\%$, as shown in Figure 1.45b.

For the matrix cracking mode 5, when the matrix crack spacing is $l_c = 20r_f$, the hysteresis loops correspond to the interface slip Case 3, i.e. the interface completely debonding and the fiber sliding partially relative to the matrix in the interface debonded region. Upon completely unloading, the interface counter slip length approaches to 67.3% of the matrix crack spacing, i.e. $2y(\sigma_{min})/l_c = 67.3\%$; and upon reloading to peak stress, the interface new slip length approaches to 67.3% of the matrix crack spacing, i.e. $2z(\sigma_{max})/l_c = 67.3\%$,

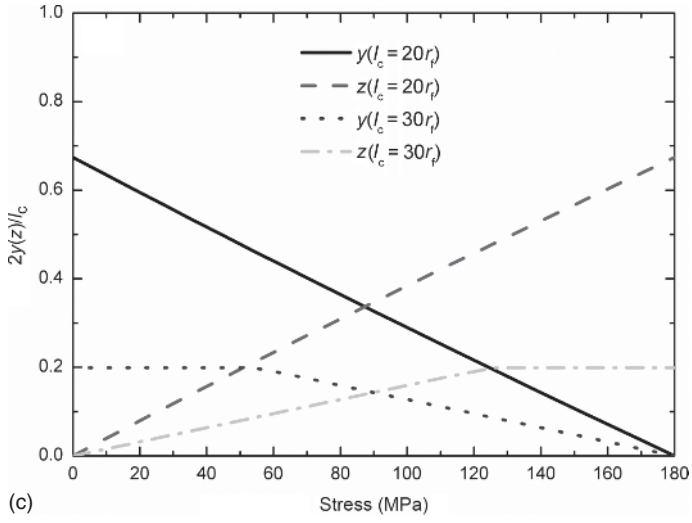

Figure 1.45 (*Continued*)

as shown in Figure 1.45c. When the matrix crack spacing is $l_c = 30r_f$, the hysteresis loops correspond to the interface slip Case 1, i.e. the interface partially debonding and the fiber sliding completely relative to the matrix in the interface debonded region. Upon unloading, the interface counter slip length approaches to the interface debonded length at the transition stress of $\sigma_{tr\_pu} = 54$ MPa, i.e. $2y(\sigma_{tr\_pu})/l_c = 19.8\%$; and upon reloading to the transition stress of $\sigma_{tr\_pr} = 126$ MPa, the interface new slip length approaches to the interface debonded length, i.e. $2z(\sigma_{tr\_pr})/l_c = 19.8\%$, as shown in Figure 1.45c.

With the increase in the matrix crack spacing, the fatigue peak strain, residual strain, and fatigue hysteresis loops area decrease, and the fatigue hysteresis modulus increases, as shown in Figure 1.45a.

1.3.3.4 Effect of Interface Properties on the Interface Sliding and Fatigue Hysteresis Loops

The effect of interface shear stress, i.e. $\tau_i = 15$ and 20 MPa, on the fatigue hysteresis loops and the interface slip of matrix cracking mode 3 and mode 5 is shown in Figure 1.46.

For the matrix cracking mode 3, when the interface shear stress is $\tau_i = 15$ MPa, the fatigue hysteresis loops correspond to the interface slip Case 2, i.e. the interface partially debonding and the fiber sliding partially relative to the matrix in the interface debonded region. Upon completely unloading, the interface counter slip length approaches to 83.2% of the interface debonded length, i.e. $y(\sigma_{min})/l_d = 83.2\%$; and upon reloading to fatigue peak stress, the interface new slip length approaches to 83.2% of the interface debonded length, i.e. $z(\sigma_{max})/l_d = 83.2\%$, as shown in Figure 1.46b. When the interface shear stress is $\tau_i = 20$ MPa, the fatigue hysteresis loops correspond to the interface slip Case 2, i.e. the interface partially debonding and the fiber sliding partially relative to the matrix in the interface debonded region. Upon completely unloading, the

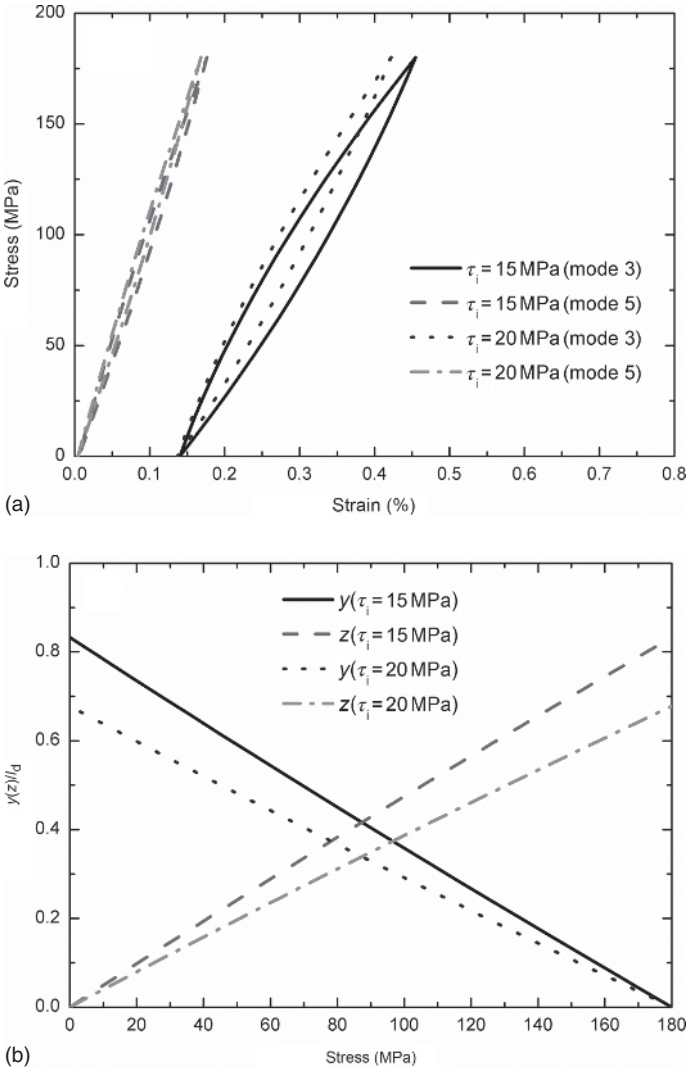

Figure 1.46 (a) The fatigue hysteresis loops of matrix cracking mode 3 and mode 5; (b) the interface slip lengths, i.e. y/l_d and z/l_d, of matrix cracking mode 3; and (c) the interface slip lengths, i.e. y/l_d and z/l_d, of matrix cracking mode 5 for different interface shear stress.

interface counter slip length approaches to 67.8% of the interface debonded length, i.e. $y(\sigma_{min})/l_d = 67.8\%$; and upon reloading to peak stress, the interface new slip length approaches to 67.8% of the interface debonded length, i.e. $z(\sigma_{max})/l_d = 67.8\%$, as shown in Figure 1.46b.

For the matrix cracking mode 5, when the interface shear stress is $\tau_i = 15$ MPa, the fatigue hysteresis loops correspond to the interface slip Case 1, i.e. the interface partially debonding and the fiber sliding completely relative to the matrix in the interface debonded region. Upon unloading, the interface counter slip length approaches to the interface debonded length at the transition stress

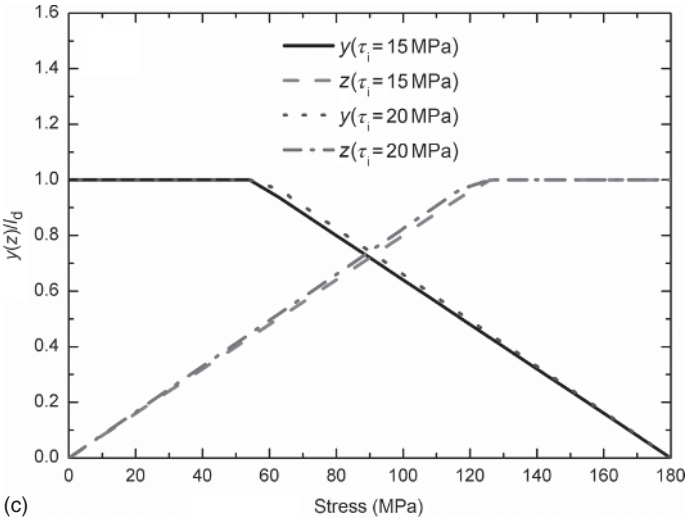

Figure 1.46 (*Continued*)

of $\sigma_{tr\_pu} = 54$ MPa, i.e. $y(\sigma_{tr\_pu})/l_d = 1$; and upon reloading to the transition stress of $\sigma_{tr\_pr} = 126$ MPa, the interface new slip length approaches to the interface debonded length, i.e. $z(\sigma_{tr\_pr})/l_d = 1$, as shown in Figure 1.46c. When the interface shear stress is $\tau_i = 20$ MPa, the hysteresis loops correspond to the interface slip Case 1, i.e. the interface partially debonding and the fiber sliding completely relative to the matrix in the interface debonded region. Upon unloading, the interface counter slip length approaches to the interface debonded length at $\sigma_{tr\_pu} = 57$ MPa, i.e. $y(\sigma_{tr\_pu})/l_d = 1$; and upon reloading to $\sigma_{tr\_pr} = 123$ MPa, the interface new slip length approaches to the interface debonded length, i.e. $z(\sigma_{tr\_pr})/l_d = 1$, as shown in Figure 1.46c.

With the increase in the interface shear stress, the fatigue peak strain, residual strain, and fatigue hysteresis loops area decrease and the fatigue hysteresis modulus increases, as shown in Figure 1.46a.

The effect of interface debonded energy, i.e. $\xi_d = 0.5$ and $1.5\ J/m^2$, on the fatigue hysteresis loops and the interface slip of matrix cracking mode 3 and mode 5 is shown in Figure 1.47.

For the matrix cracking mode 3, when the interface debonding energy is $\xi_d = 0.5\ J/m^2$, the fatigue hysteresis loops correspond to the interface slip Case 2, i.e. the interface partially debonding and the fiber sliding partially relative to the matrix in the interface debonded region. Upon completely unloading, the interface counter slip length approaches to 74.1% of the interface debonded length, i.e. $y(\sigma_{min})/l_d = 74.1\%$; and upon reloading to peak stress, the interface new slip length approaches to 74.1% of the interface debonded length, i.e. $z(\sigma_{max})/l_d = 74.1\%$, as shown in Figure 1.47b. When the interface debonding energy is $\xi_d = 1.5\ J/m^2$, the fatigue hysteresis loops correspond to the interface slip Case 2, i.e. the interface partially debonding and the fiber sliding partially relative to the matrix in the interface debonded region. Upon completely unloading, the interface counter slip length approaches to 90.6% of the interface

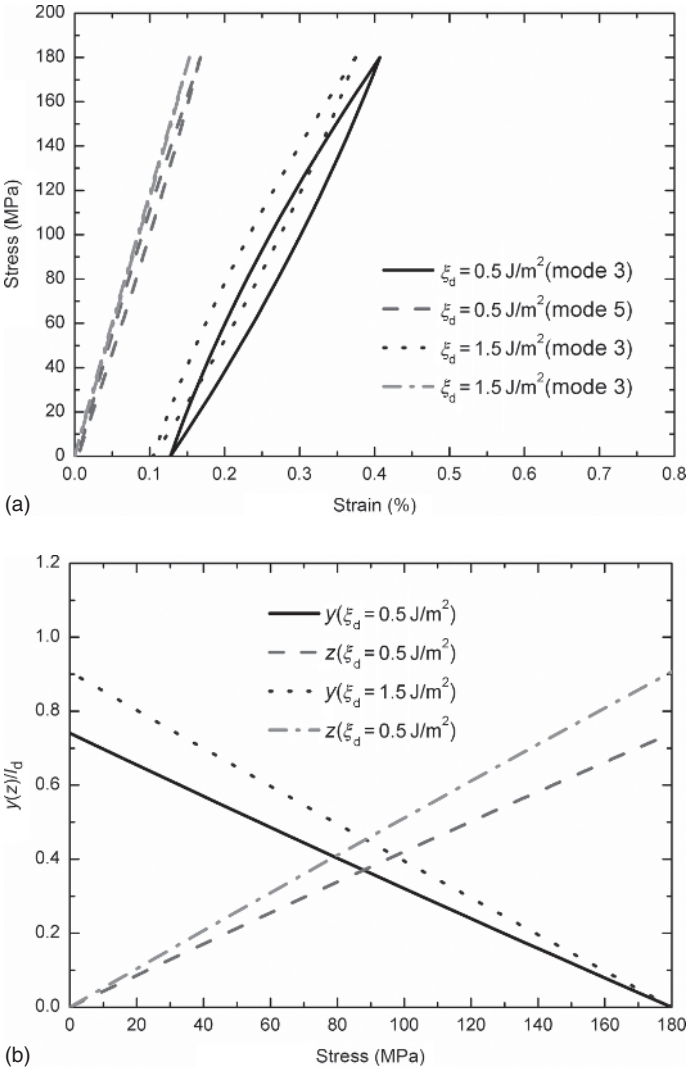

Figure 1.47 (a) The fatigue hysteresis loops of matrix cracking mode 3 and mode 5; (b) the interface slip lengths, i.e. y/l_d and z/l_d, of matrix cracking mode 3; and (c) the interface slip lengths, i.e. y/l_d and z/l_d, of matrix cracking mode 5 for different interface debonded energy.

debonded length, i.e. $y(\sigma_{min})/l_d = 90.6\%$; and upon reloading to peak stress, the interface new slip length approaches to 90.6% of the interface debonded length, i.e. $z(\sigma_{max})/l_d = 90.6\%$, as shown in Figure 1.47b.

For the matrix cracking mode 5, when the interface debonding energy is $\xi_d = 0.5\,J/m^2$, the fatigue hysteresis loops correspond to the interface slip Case 1, i.e. the interface partially debonding and the fiber sliding completely relative to the matrix in the interface debonded region. Upon unloading, the interface counter slip length approaches to the interface debonded length at the transition stress of $\sigma_{tr\_pu} = 54\,MPa$, i.e. $y(\sigma_{tr\_pu})/l_d = 1$; and upon reloading to the transition

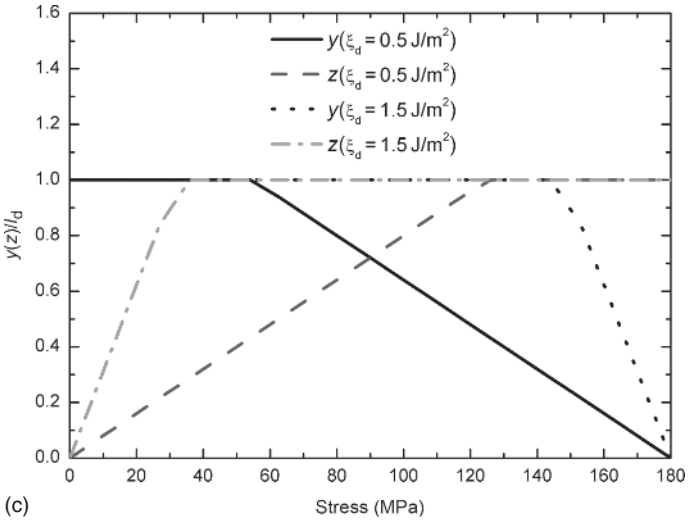

Figure 1.47 (*Continued*)

stress of $\sigma_{tr\_pr} = 126$ MPa, the interface new slip length approaches to the interface debonded length, i.e. $z(\sigma_{tr\_pr})/l_d = 1$, as shown in Figure 1.47c. When the interface debonding energy is $\xi_d = 1.5$ J/m^2, the fatigue hysteresis loops correspond to the interface slip Case 1, i.e. the interface partially debonding and the fiber sliding completely relative to the matrix in the interface debonded region. Upon unloading, the interface counter slip length approaches to the interface debonded length at the transition stress of $\sigma_{tr\_pu} = 144$ MPa, i.e. $y(\sigma_{tr\_pu})/l_d = 1$; and upon reloading to the transition stress of $\sigma_{tr\_pr} = 36$ MPa, the interface new slip length approaches to the interface debonded length, i.e. $z(\sigma_{tr\_pr})/l_d = 1$, as shown in Figure 1.47c.

With the increase in the interface debonded energy, the fatigue peak strain, residual strain, and fatigue hysteresis loops area decrease, and the fatigue hysteresis modulus increases, as shown in Figure 1.47a.

1.3.3.5 Effect of Matrix Racking Mode Proportion on Interface Sliding and Fatigue Hysteresis Loops

The effect of matrix cracking proportion, i.e. $\eta = 0$–1, on the fatigue hysteresis loops is shown in Figure 1.48a. When $\eta = 0$, there is only matrix cracking mode 5 in the composite; when $\eta = 1$, there is only matrix cracking mode 3 in the composite; and when $0 < \eta < 1$, there are both matrix cracking mode 3 and mode 5 in the composite. With the increase in matrix cracking mode 3 proportion η, the peak strain, residual strain, and hysteresis loops area increase, and the hysteresis modulus decreases, as shown in Figure 1.48a.

For the matrix cracking mode 3, the fatigue hysteresis loops correspond to the interface slip Case 2, i.e. the interface partially debonding and the fiber sliding partially relative to the matrix in the interface debonded region. Upon completely unloading, the interface counter slip length approaches to 70.8% of the interface debonded length of $y(\sigma_{min})/l_d = 70.8\%$; and upon reloading to peak stress, the

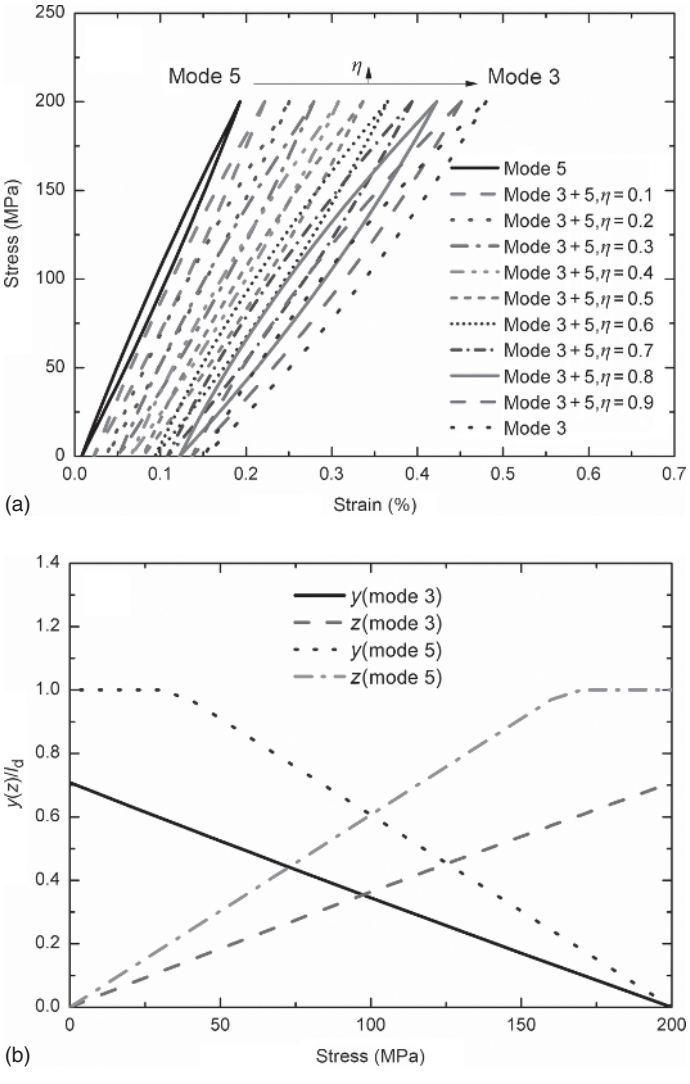

Figure 1.48 (a) The fatigue hysteresis loops of single matrix cracking mode 3 and mode 5, and with damage parameter $\eta = 0.1$–0.9; and (b) the interface slip lengths, i.e. y/l_d and z/l_d, of matrix cracking mode 3 and mode 5.

interface new slip length approaches to 70.8% of the interface debonded length of $z(\sigma_{max})/l_d = 70.8\%$, as shown in Figure 1.48b.

For the matrix cracking mode 5, the fatigue hysteresis loops correspond to the interface slip Case 1, i.e. the interface partially debonding and the fiber sliding completely relative to the matrix in the interface debonded region. Upon unloading, the interface counter slip length approaches to the interface debonded length at the transition stress of $\sigma_{tr\_pu} = 30$ MPa, i.e. $y(\sigma_{tr\_pu})/l_d = 1$; and upon reloading to the transition stress of $\sigma_{tr\_pr} = 170$ MPa, the interface new slip length

approaches to the interface debonded length, i.e. $z(\sigma_{tr\_pr})/l_d = 1$, as shown in Figure 1.48b.

1.3.4 Experimental Comparisons

1.3.4.1 Cross-Ply C/SiC Composite

The typical stress–strain curve of cross-ply C/SiC composite under cyclic loading/unloading tensile experiments at room temperature is shown in Figure 1.49. The specimen was unloading and subsequent reloading at the peak stress of 20, 40, 60, 80, 100, and 120 MPa and failed at the stress of 124.5 MPa with the failure strain of 0.24%. It can be found that the loading/unloading tensile stress–strain curve of cross-ply C/SiC composite exhibits obvious hysteresis behavior. Because of the large mismatch of the axial thermal expansion coefficient between the carbon fiber and silicon carbide matrix (-0.38×10^{-6}/°C versus 2.8×10^{-6}/°C), there are unavoidable microcracks existed within the SiC matrix in the 90° and 0° plies when the composites are cooled down from high process temperature to ambient temperature. These processing-induced microcracks propagated in conjunction with new microcracks during the loading process forming the mode 5 matrix cracking in 0° plies. As applied stress increasing, some transverse cracks in 90° plies connected with the matrix cracks in the 0° plies forming the mode 3 major cracks, which cross the 90° and 0° plies.

The experimental and analytical model predicted fatigue hysteresis loops of cross-ply C/SiC composite under the fatigue peak stress of $\sigma_{max} = 60$ MPa are shown in Figure 1.50a. The unloading interface counter slip length and reloading new slip length of the matrix cracking mode 3 and mode 5 as a function of applied stress are shown in Figure 1.50b. The fiber/matrix interface debonds partially for cracking mode 3 and mode 5 at the maximum stress of 60 MPa. As for matrix

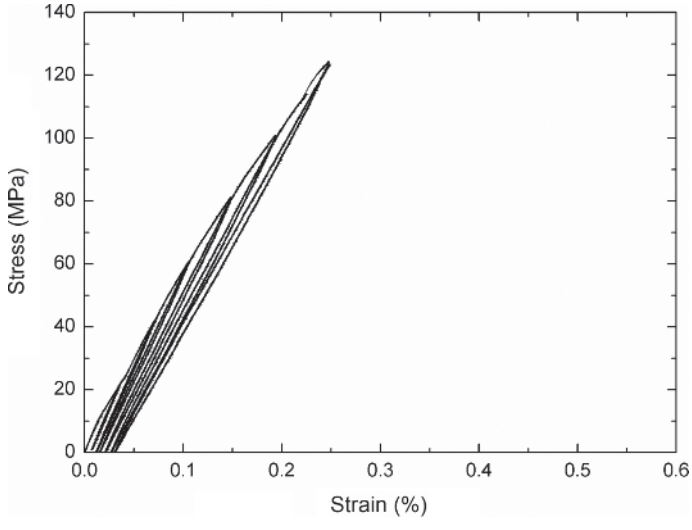

Figure 1.49 The loading/unloading tensile stress–strain curve of cross-ply C/SiC composite at room temperature.

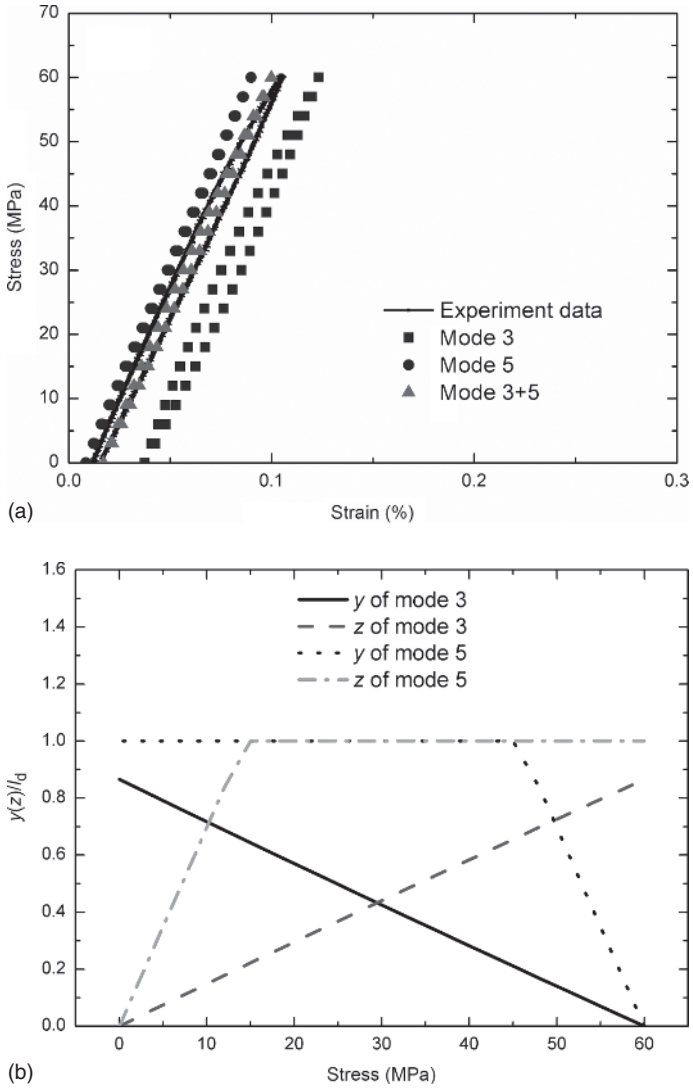

Figure 1.50 (a) The experimental and predicted fatigue hysteresis loops; (b) the unloading interface counter slip length and reloading interface new slip length versus the applied stress for the matrix cracking mode 3 and mode 5 of cross-ply C/SiC composite under the fatigue peak stress of $\sigma_{max} = 60$ MPa.

cracking mode 3, the unloading interface counter slip length y increases as stress decreases until the valley stress of σ_{min}, at which the unloading interface counter slip length does not approach to the interface debonding tip of $y(\sigma_{min}) < l_d$. The completely unloading interface counter slip length occupies 86.5% of the entire interface debonded region of $y(\sigma_{min})/l_d = 86.5\%$. The reloading interface new slip length does not approach to the interface debonding tip of $z(\sigma_{max}) < l_d$. The fatigue hysteresis loops of the matrix cracking mode 3 correspond to the interface slip Case 2, i.e. the interface partially debonding and the fiber sliding partially

relative to the matrix upon unloading and subsequent reloading. As for the matrix cracking mode 5, the unloading interface counter slip length increases as applied stress decreases until the transition stress of $\sigma_{tr\_pu} = 45$ MPa, at which the unloading interface counter slip length approaches to the interface debonding tip of $y(\sigma_{tr\_pu} = 45\,\text{MPa}) = l_d$, and the interface completely slips upon continued unloading. The reloading new slip length increases as the applied stress increases until the transition stress of $\sigma_{tr\_pr} = 15$ MPa, at which the reloading interface new slip length approaches to the interface debonding tip of $z(\sigma_{tr\_pr}) = l_d$ and the interface completely slips upon continued reloading. The fatigue hysteresis loops of the matrix cracking mode 5 correspond to the interface slip Case 1, i.e. the interface partially debonds and the fiber slides completely relative to the matrix upon unloading and subsequent reloading. As the matrix cracking mode 3 and mode 5 exist in the composites, the fatigue hysteresis loops considering the matrix cracking mode 3 and mode 5 together agree well with the experimental data. The value of damage mode parameter of cross-ply C/SiC composite at the fatigue peak stress of $\sigma_{max} = 60$ MPa is $\eta = 0.30$, which means that the proportion of the cracking mode 3 unit cell is 30% in the entire composites.

The experimental and analytical model predicted fatigue hysteresis loops of cross-ply C/SiC composite under the peak stress of $\sigma_{max} = 80$ MPa are shown in Figure 1.51a. The unloading interface counter slip length and reloading new slip length of the matrix cracking mode 3 and mode 5 as a function of applied stress are shown in Figure 1.51b. The fiber/matrix interface debonds partially for the matrix cracking mode 3 and mode 5 at the peak stress of $\sigma_{max} = 80$ MPa. As for the matrix cracking mode 3, the unloading interface counter slip length y increases as stress decreases until the valley stress of σ_{min}, at which the unloading interface counter slip length does not approach to the interface debonding tip of $y(\sigma_{min}) < l_d$. The completely unloading interface counter slip length occupies 73.5% of the entire interface debonded region of $y(\sigma_{min})/l_d = 73.5\%$. The reloading interface new slip length does not approach to the interface debonding tip of $z(\sigma_{max}) < l_d$. The fatigue hysteresis loops of the matrix cracking mode 3 correspond to the interface slip Case 2, i.e. the interface partially debonds and the fiber slides partially relative to the matrix upon unloading and subsequent reloading. As for the matrix cracking mode 5, the unloading interface counter slip length y increases as stress decreases until the transition stress of $\sigma_{tr\_pu} = 24$ MPa, at which the unloading interface counter slip length approaches to the interface debonding tip of $y(\sigma_{tr\_pu} = 24\,\text{MPa}) = l_d$, and the interface completely slips upon continued unloading. The reloading new slip length increases as the applied stress increases until the transition stress of $\sigma_{tr\_pr} = 56$ MPa, at which the reloading interface new slip length approaches to the interface debonding tip of $z(\sigma_{tr\_pr} = 56\,\text{MPa}) = l_d$, and the interface completely slips upon continued reloading. The fatigue hysteresis loops of the matrix cracking mode 5 correspond to the interface slip Case 1, i.e. the interface partially debonds and the fiber slides completely relative to the matrix upon unloading and subsequent reloading. As the matrix cracking mode 3 and mode 5 both exist in the composites, the stress–strain hysteresis loops considering mode 3 and mode 5 together agree well with the experimental data. The value of damage mode parameter of cross-ply C/SiC composite at the peak stress

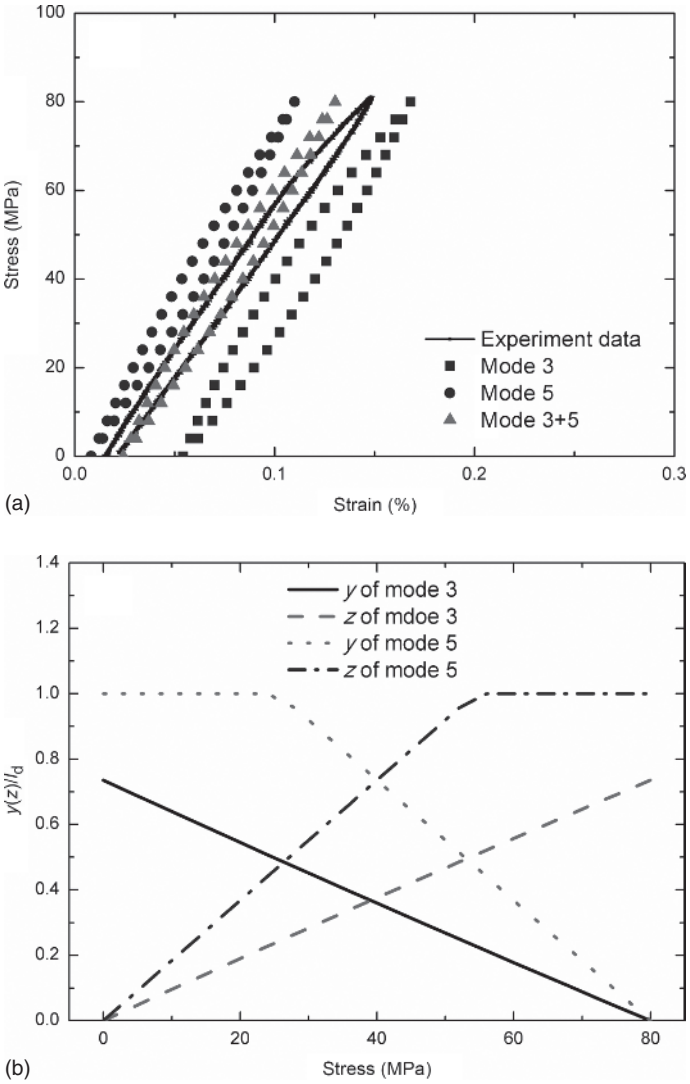

Figure 1.51 (a) The experimental and predicted fatigue hysteresis loops; (b) the unloading interface counter slip length and reloading interface new slip length versus the applied stress for the matrix cracking mode 3 and mode 5 of cross-ply C/SiC composite under the fatigue peak stress of $\sigma_{max} = 80$ MPa.

of $\sigma_{max} = 80$ MPa is $\eta = 0.35$, which means that the proportion of the cracking mode 3 unit cell is approximate 35% in the entire composites.

The experimental and analytical model predicted fatigue hysteresis loops of cross-ply C/SiC composite under the fatigue peak stress of $\sigma_{max} = 100$ MPa are shown in Figure 1.52a. The unloading interface counter slip length and reloading new slip length of the matrix cracking mode 3 and mode 5 as a function of the applied stress are shown in Figure 1.52b. The fiber/matrix interface debonds

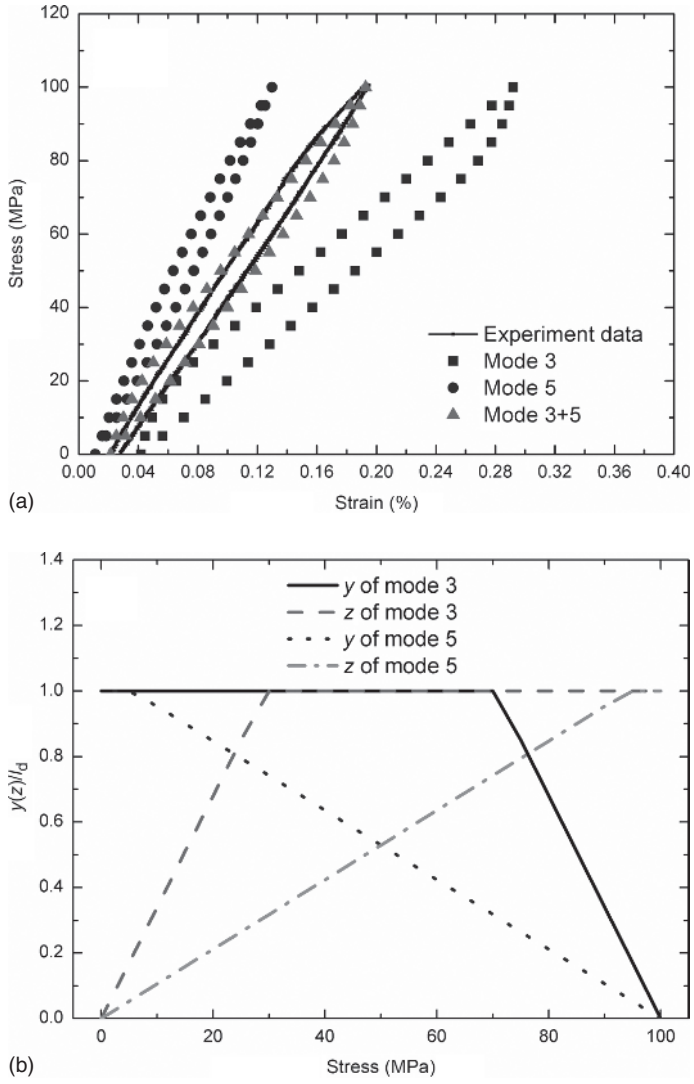

Figure 1.52 (a) The experimental and predicted fatigue hysteresis loops; (b) the unloading interface counter slip length and reloading interface new slip length versus the applied stress for the matrix cracking mode 3 and mode 5 of cross-ply C/SiC composite under the fatigue peak stress of $\sigma_{max} = 100$ MPa.

completely for the matrix cracking mode 3 and partially for the matrix cracking mode 5 at the peak stress of $\sigma_{max} = 100$ MPa. As for the matrix cracking mode 3, the unloading interface counter slip length increases as the applied stress decreases until the transition stress of $\sigma_{tr\_fu} = 70$ MPa, at which the unloading interface counter slip length approaches to the interface debonding length of $y(\sigma_{tr\_fu} = 70\,\text{MPa}) = l_d$, and the interface completely slips upon continued unloading. The reloading new slip length z increases as stress increases until the

transition stress of $\sigma_{tr\_pr} = 30\,MPa$, at which the reloading interface new slip length approaches to the interface debonding tip of $z(\sigma_{tr\_pr} = 30\,MPa) = l_d$ and the interface completely slips upon continued reloading. The fatigue hysteresis loops of the matrix cracking mode 3 correspond to the interface slip Case 4, i.e. the interface completely debonds and the fiber slides completely relative to matrix upon unloading and subsequent reloading. As for the matrix cracking mode 5, the unloading interface counter slip length increases as the applied stress decreases until the transition stress of $\sigma_{tr\_pu} = 95\,MPa$, at which the unloading interface counter slip length approaches to the interface debonding tip of $y(\sigma_{tr\_pu} = 95\,MPa) = l_d$, and the interface completely slips upon continued unloading. The reloading new slip length increases as the applied stress increases until the transition stress of $\sigma_{tr\_pr} = 5\,MPa$, at which the reloading interface new slip length approaches to the interface debonding tip of $z(\sigma_{tr\_pr} = 5\,MPa) = l_d$ and the interface completely slips upon continued reloading. The fatigue hysteresis loops of the matrix cracking mode 5 correspond to the interface slip Case 1, i.e. the interface partially debonds and the fiber slides completely relative to matrix during unloading and subsequent reloading. As matrix cracking mode 3 and mode 5 both exist in the composites, the fatigue hysteresis loops considering the matrix cracking mode 3 and mode 5 together agree well with the experimental data. The value of damage mode parameter of cross-ply C/SiC composite at the fatigue peak stress of $\sigma_{max} = 100\,MPa$ is $\eta = 0.40$, which means that the proportion of the cracking mode 3 unit cell is approximate 40% in the entire composites.

The experimental and analytical model predicted fatigue hysteresis loops of cross-ply C/SiC composite under the fatigue peak stress of $\sigma_{max} = 120\,MPa$ are shown in Figure 1.53a. The unloading interface counter slip length and reloading new slip length of the matrix cracking mode 3 and mode 5 as a function of the applied stress are shown in Figure 1.53b. The fiber/matrix interface debonds completely for the matrix cracking mode 3 and partially for cracking mode 5 at the peak stress of $\sigma_{max} = 120\,MPa$. As for the matrix cracking mode 3, the unloading interface counter slip length increases as the applied stress decreases until the transition stress of $\sigma_{tr\_fu} = 90\,MPa$, at which the unloading interface counter slip length y approaches to the interface debonding length, i.e. $y(\sigma_{tr\_fu} = 90\,MPa) = l_d$, and the interface completely slips upon continued unloading. The reloading interface new slip length approaches to the interface debonding length, i.e. $z(\sigma_{tr\_fr} = 30\,MPa) = l_d$. The fatigue hysteresis loops of the matrix cracking mode 3 correspond to the interface slip Case 4, i.e. the interface completely debonds and fiber slides completely relative to matrix upon unloading and subsequent reloading. As for the matrix cracking mode 5, the unloading interface counter slip length increases as the applied stress decreases until the valley stress of σ_{min}, at which the unloading interface counter slip length does not approach to the interface debonding tip of $y(\sigma_{min}) < l_d$. The completely unloading interface counter slip length occupies 89.3% of the entire interface debonded region of $y(\sigma_{min})/l_d = 89.3\%$. The reloading interface new slip length does not approach to the interface debonding tip of $z(\sigma_{max}) < l_d$. The fatigue hysteresis loops of the matrix cracking mode 5 correspond to the interface slip

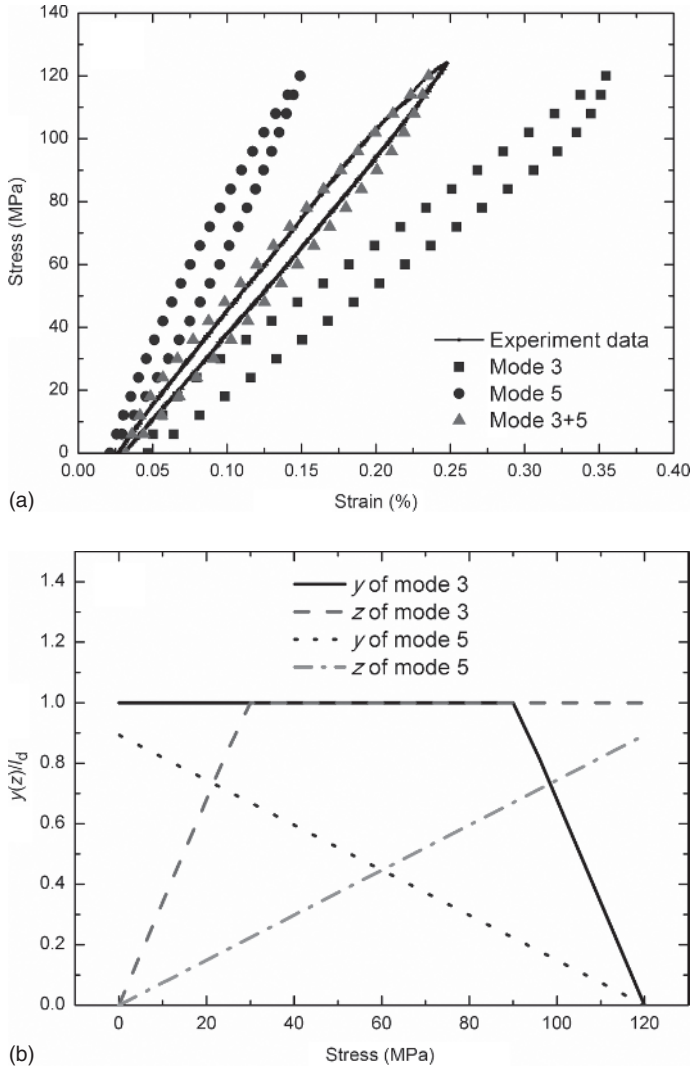

Figure 1.53 (a) The experimental and predicted fatigue hysteresis loops; (b) the unloading interface counter slip length and reloading interface new slip length versus the applied stress for the matrix cracking mode 3 and mode 5 of cross-ply C/SiC composites under the fatigue peak stress of $\sigma_{max} = 120$ MPa.

Case 2, i.e. the interface partially debonds and fiber slides partially relative to matrix upon unloading and subsequent reloading. As matrix cracking mode 3 and mode 5 both exist in the composites, the stress–strain hysteresis loops considering mode 3 and mode 5 together agree well with the experimental data. The value of damage mode parameter of cross-ply C/SiC composite at the peak stress of $\sigma_{max} = 120$ MPa is $\eta = 0.42$, which means that the proportion of the cracking mode 3 unit cell is approximate 42% in the entire composites.

1.3.4.2 2D SiC/SiC Composite

Li et al. (2014) investigated the cyclic loading/unloading hysteresis behavior of 2D SiC/SiC composite. The loading/unloading peak stresses are $\sigma_{max} = 152$, 166, 181, 195, 210, 224, 239, and 253 MPa, respectively. The fatigue hysteresis loops of 2D SiC/SiC composite corresponding to different fatigue peak stresses are predicted using the present analysis.

Under the fatigue peak stress of $\sigma_{max} = 152$ MPa, the experimental and theoretical hysteresis loops are shown in Figure 1.54a, in which the proportion of matrix cracking mode 3 is $\eta = 0.2$. For the matrix cracking mode 3,

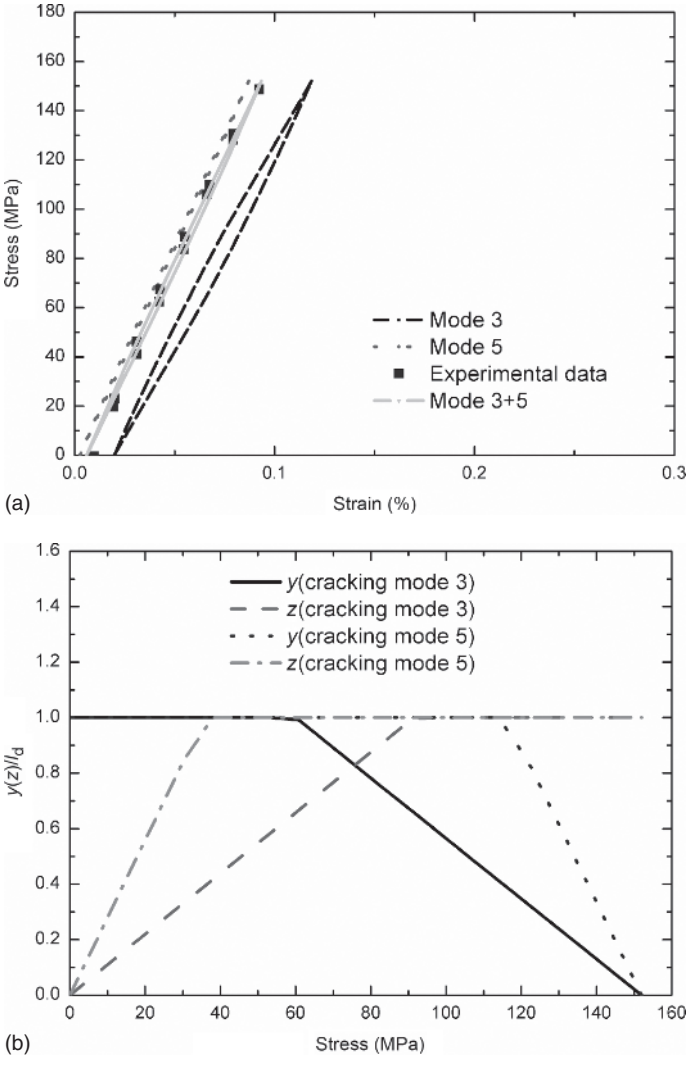

Figure 1.54 (a) The experimental and predicted fatigue hysteresis loops; and (b) the interface slip lengths of matrix cracking mode 3 and mode 5 of 2D SiC/SiC composite under the fatigue peak stress of $\sigma_{max} = 152$ MPa.

the fatigue hysteresis loops correspond to the interface slip Case 1, i.e. the fiber/matrix interface partially debonding and the fiber sliding completely relative to the matrix in the interface debonding region upon unloading and reloading, as shown in Figure 1.54b. Upon unloading, the interface counter slip length approaches to the interface debonded length at the transition stress of $\sigma_{tr\_pu} = 53.2$ MPa of $y(\sigma_{tr\_pu} = 53.2\,\text{MPa})/l_d = 1$; and upon reloading to the transition stress of $\sigma_{tr\_pr} = 98.8$ MPa, the interface new slip length approaches to the interface debonded length of $z(\sigma_{tr\_pr} = 98.8\,\text{MPa})/l_d = 1$. For the matrix cracking mode 5, the fatigue hysteresis loops correspond to the interface slip Case 1, i.e. the fiber/matrix interface partially debonding and the fiber sliding completely relative to the matrix in the interface debonding region upon unloading and reloading. Upon unloading, the interface counter slip length approaches to the interface debonded length at the transition stress of $\sigma_{tr\_pu} = 114$ MPa of $y(\sigma_{tr\_pu} = 114\,\text{MPa})/l_d = 1$; and upon reloading to the transition stress of $\sigma_{tr\_pr} = 38$ MPa, the interface new slip length approaches to the interface debonded length of $z(\sigma_{tr\_pr} = 38\,\text{MPa})/l_d = 1$.

Under the fatigue peak stress of $\sigma_{max} = 166$ MPa, the experimental and theoretical hysteresis loops are shown in Figure 1.55a, in which the proportion of matrix cracking mode 3 is $\eta = 0.25$. For the matrix cracking mode 3, the fatigue hysteresis loops correspond to the interface slip Case 1, i.e. the fiber/matrix interface partially debonding and the fiber sliding completely relative to the matrix in the interface debonding region upon unloading and reloading, as shown in Figure 1.55b. Upon unloading, the interface counter slip length approaches to the interface debonded length at the transition stress of $\sigma_{tr\_pu} = 41.5$ MPa, i.e. $y(\sigma_{tr\_pu} = 41.5\,\text{MPa})/l_d = 1$; and upon reloading to the transition stress of $\sigma_{tr\_pr} = 124.5$ MPa, the interface new slip length approaches to the interface debonded length, i.e. $z(\sigma_{tr\_pr} = 124.5\,\text{MPa})/l_d = 1$. For the matrix cracking mode 5, the fatigue hysteresis loops correspond to the interface slip Case 1, i.e. the fiber/matrix interface partially debonding and the fiber sliding completely relative to the matrix in the interface debonding region upon unloading and reloading. Upon unloading, the interface counter slip length approaches to the interface debonded length at the transition stress of $\sigma_{tr\_pu} = 99.6$ MPa, i.e. $y(\sigma_{tr\_pu} = 99.6\,\text{MPa})/l_d = 1$; and upon reloading to the transition stress of $\sigma_{tr\_pr} = 66.4$ MPa, the interface new slip length approaches to the interface debonded length, i.e., $z(\sigma_{tr\_pr} = 66.4\,\text{MPa})/l_d = 1$.

Under the fatigue peak stress of $\sigma_{max} = 181$ MPa, the experimental and predicted fatigue hysteresis loops are shown in Figure 1.56a, in which the proportion of matrix cracking mode 3 is $\eta = 0.35$. For the matrix cracking mode 3, the fatigue hysteresis loops correspond to the interface slip Case 1, i.e. the fiber/matrix interface partially debonding and the fiber sliding completely relative to the matrix in the interface debonding region upon unloading and reloading, as shown in Figure 1.56b. Upon unloading, the interface counter slip length approaches to the interface debonded length at the transition stress of $\sigma_{tr\_pu} = 27.1$ MPa, i.e. $y(\sigma_{tr\_pu} = 27.1\,\text{MPa})/l_d = 1$; and upon reloading to the transition stress of $\sigma_{tr\_pr} = 153.9$ MPa, the interface new slip length approaches to the interface debonded length, i.e. $z(\sigma_{tr\_pr} = 153.9\,\text{MPa})/l_d = 1$. For the matrix cracking mode 5, the fatigue hysteresis loops correspond to the interface slip

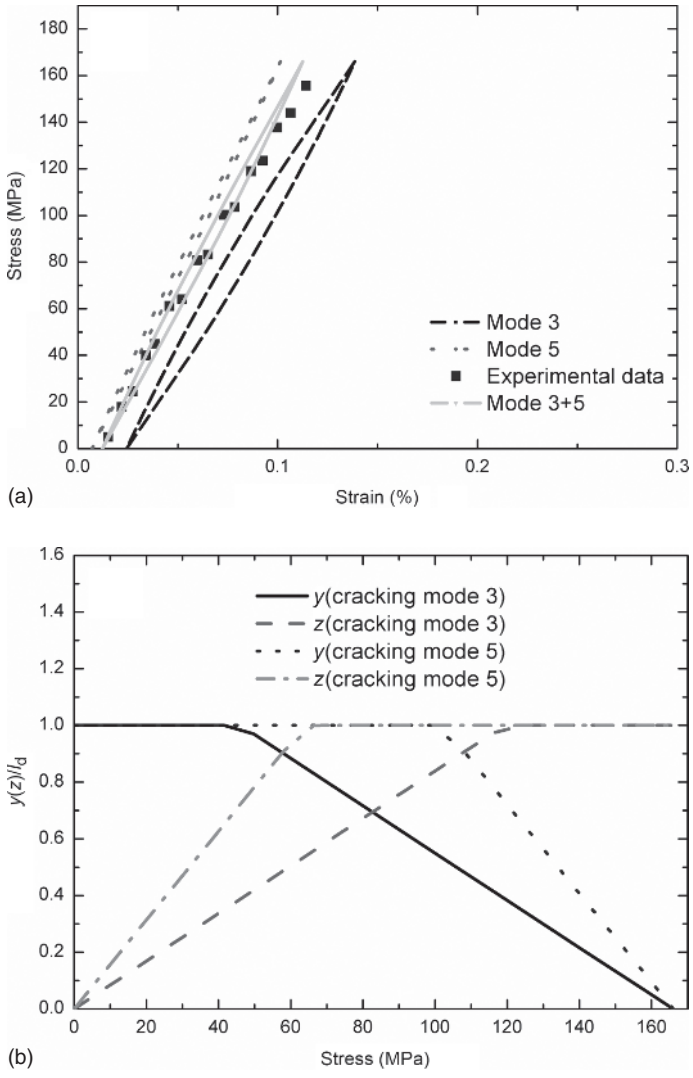

Figure 1.55 (a) The experimental and analytical model predicted fatigue hysteresis loops; and (b) the interface slip lengths of matrix cracking mode 3 and mode 5 of 2D SiC/SiC composite under the fatigue peak stress of $\sigma_{max} = 166$ MPa.

Case 1, i.e. the fiber/matrix interface partially debonding and the fiber sliding completely relative to the matrix in the interface debonding region upon unloading and reloading. Upon unloading, the interface counter slip length approaches to the interface debonded length at the transition stress of $\sigma_{tr\_pu} = 81.5$ MPa, i.e. $y(\sigma_{tr\_pu} = 81.5\,\text{MPa})/l_d = 1$; and upon reloading to the transition stress of $\sigma_{tr\_pu} = 99.5$ MPa, the interface new slip length approaches to the interface debonded length, i.e. $z(\sigma_{tr\_pr} = 99.5\,\text{MPa})/l_d = 1$.

Under the fatigue peak stress of $\sigma_{max} = 195$ MPa, the experimental and predicted fatigue hysteresis loops are shown in Figure 1.57a, in which the

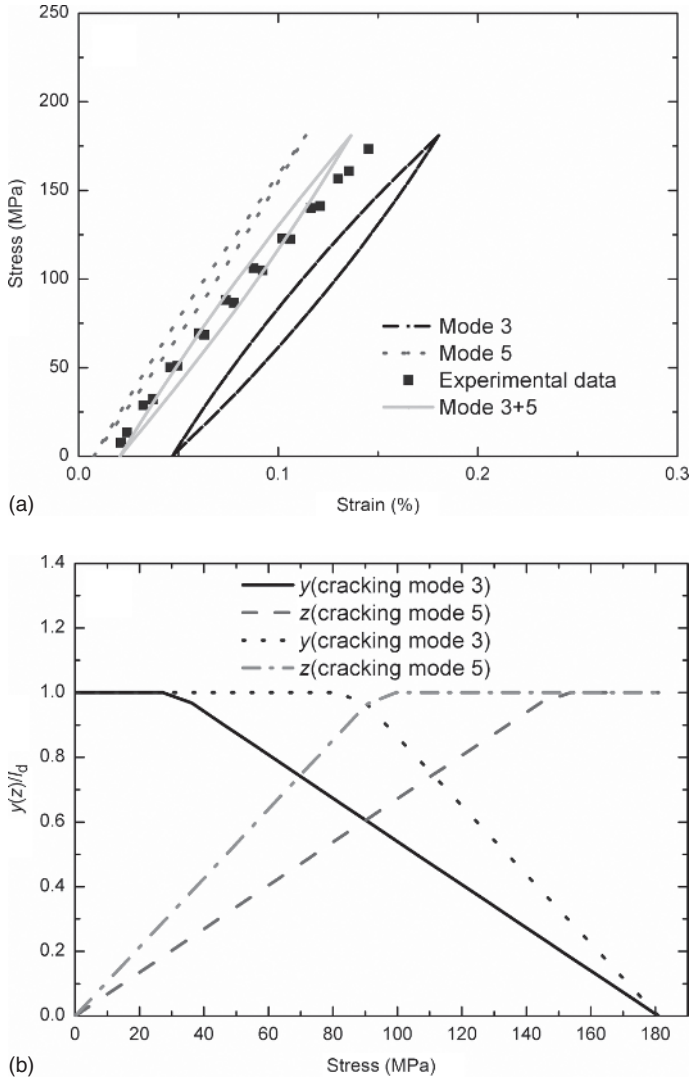

Figure 1.56 (a) The experimental and predicted fatigue hysteresis loops; and (b) the interface slip lengths of matrix cracking mode 3 and mode 5 of 2D SiC/SiC composite under the fatigue peak stress of $\sigma_{max} = 181$ MPa.

proportion of matrix cracking mode 3 is $\eta = 0.45$. For the matrix cracking mode 3, the fatigue hysteresis loops correspond to the interface slip Case 1, i.e. the fiber/matrix interface partially debonding and the fiber sliding completely relative to the matrix in the interface debonding region upon unloading and reloading, as shown in Figure 1.57b. Upon unloading, the interface counter slip length approaches to the interface debonded length at the transition stress of $\sigma_{tr\_pu} = 9.7$ MPa, i.e. $y(\sigma_{tr\_pu} = 9.7\,\text{MPa})/l_d = 1$; and upon reloading to the transition stress of $\sigma_{tr\_pr} = 185.3$ MPa, the interface new slip length approaches

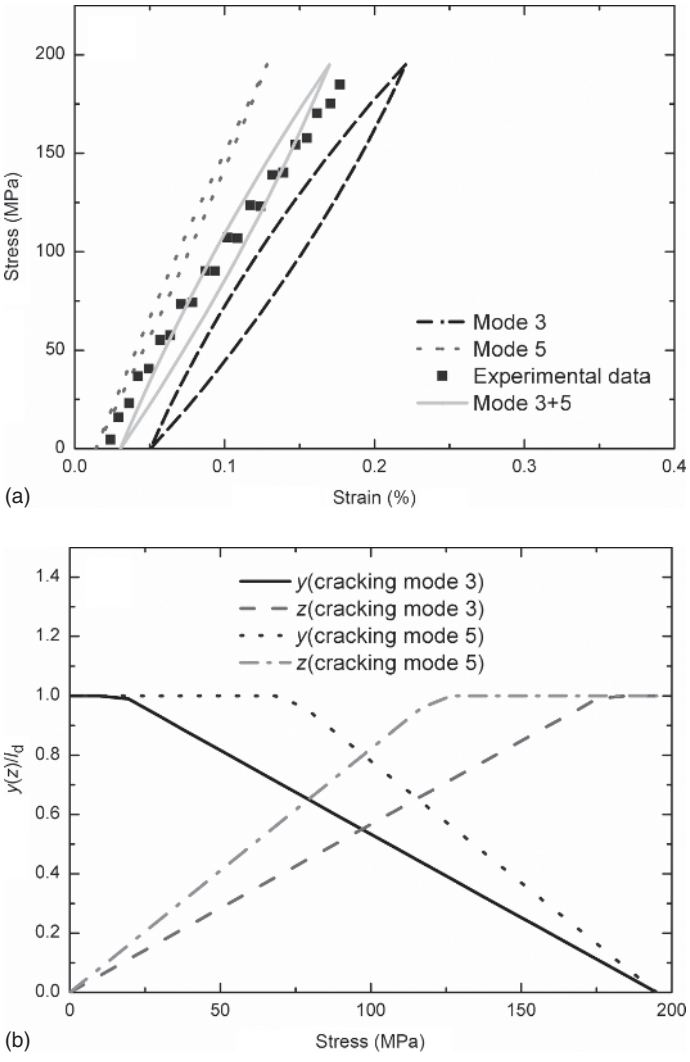

Figure 1.57 (a) The experimental and predicted fatigue hysteresis loops; and (b) the interface slip lengths, i.e. y/l_d and z/l_d, of matrix cracking mode 3 and mode 5 of 2D SiC/SiC composite under the fatigue peak stress of $\sigma_{max} = 195$ MPa.

to the interface debonded length, i.e. $z(\sigma_{tr\_pr} = 185.3\,\text{MPa})/l_d = 1$. For the matrix cracking mode 5, the fatigue hysteresis loops correspond to the interface slip Case 1, i.e. the fiber/matrix interface partially debonding and the fiber sliding completely relative to the matrix in the interface debonding region upon unloading and reloading. Upon unloading, the interface counter slip length approaches to the interface debonded length at the transition stress of $\sigma_{tr\_pu} = 68.2$ MPa, i.e. $y(\sigma_{tr\_pu} = 68.2\,\text{MPa})/l_d = 1$; and upon reloading to the transition stress of $\sigma_{tr\_pr} = 126.8$ MPa, the interface new slip length approaches to the interface debonded length, i.e. $z(\sigma_{tr\_pr} = 126.8\,\text{MPa})/l_d = 1$.

Under the fatigue peak stress of $\sigma_{max} = 210$ MPa, the experimental and predicted fatigue hysteresis loops are shown in Figure 1.58a, in which the proportion of matrix cracking mode 3 is $\eta = 0.5$. For the matrix cracking mode 3, the fatigue hysteresis loops correspond to the interface slip Case 1, i.e. the fiber/matrix interface partially debonding and the fiber sliding completely relative to the matrix in the interface debonding region upon unloading and reloading, as shown in Figure 1.58b. Upon completely unloading, the interface counter slip length approaches to the interface debonded length of $y(\sigma_{min})/l_d = 1$;

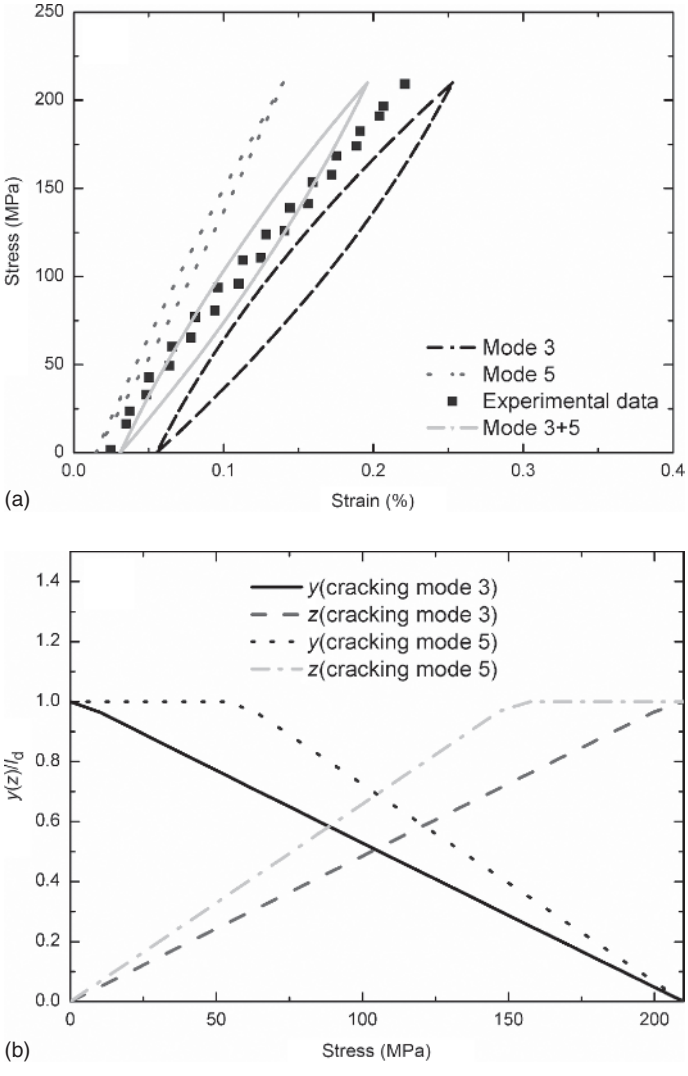

Figure 1.58 (a) The experimental and predicted fatigue hysteresis loops; and (b) the interface slip lengths of matrix cracking mode 3 and mode 5 of 2D SiC/SiC composite under the fatigue peak stress of $\sigma_{max} = 210$ MPa.

and upon reloading to peak stress, the interface new slip length approaches to the interface debonded length of $z(\sigma_{max})/l_d = 1$. For the matrix cracking mode 5, the fatigue hysteresis loops correspond to the interface slip Case 1, i.e. the fiber/matrix interface partially debonding and the fiber sliding completely relative to the matrix in the interface debonding region upon unloading and reloading. Upon unloading, the interface counter slip length approaches to the interface debonded length at the transition stress of $\sigma_{tr\_pu} = 52.5$ MPa of $y(\sigma_{tr\_pu} = 52.5\,\text{MPa})/l_d = 1$; and upon reloading to the transition stress of $\sigma_{tr\_pr} = 157.5$ MPa, the interface new slip length approaches to the interface debonded length, i.e. $z(\sigma_{tr\_pr} = 157.5\,\text{MPa})/l_d = 1$.

Under the fatigue peak stress of $\sigma_{max} = 224$ MPa, the experimental and theoretical hysteresis loops are shown in Figure 1.59a, in which the proportion of matrix cracking mode 3 is $\eta = 0.55$. For the matrix cracking mode 3, the fatigue hysteresis loops correspond to the interface slip Case 2, i.e. the fiber/matrix interface partially debonding and the fiber sliding completely relative to the matrix in the interface debonding region upon unloading and reloading, as shown in Figure 1.59b. Upon completely unloading, the interface counter slip length approaches to 95.3% of the interface debonded length of $y(\sigma_{min})/l_d = 1$; and upon reloading to peak stress, the interface new slip length approaches to 95.3% of the interface debonded length of $z(\sigma_{max})/l_d = 1$. For matrix cracking mode 5, the hysteresis loops correspond to the interface slip Case 1, i.e. the fiber/matrix interface partially debonding and the fiber sliding completely relative to the matrix in the interface debonding region upon unloading and reloading. Upon unloading, the interface counter slip length approaches to the interface debonded length at the transition stress of $\sigma_{tr\_pu} = 33.6$ MPa of $y(\sigma_{tr\_pu} = 33.6\,\text{MPa})/l_d = 1$; and upon reloading to the transition stress of $\sigma_{tr\_pr} = 190.4$ MPa, the interface new slip length approaches to the interface debonded length, i.e. $z(\sigma_{tr\_pr} = 190.4\,\text{MPa})/l_d = 1$.

Under the fatigue peak stress of $\sigma_{max} = 239$ MPa, the experimental and theoretical hysteresis loops are shown in Figure 1.60a, in which the proportion of matrix cracking mode 3 is $\eta = 0.6$. For the matrix cracking mode 3, the hysteresis loops correspond to the interface slip Case 2, i.e. the fiber/matrix interface partially debonding and the fiber sliding partially relative to the matrix in the interface debonding region upon unloading and reloading, as shown in Figure 1.60b. Upon completely unloading, the interface counter slip length approaches to 90.2% of the interface debonded length of $y(\sigma_{min})/l_d = 90.2\%$; and upon reloading to peak stress, the interface new slip length approaches to 90.2% of the interface debonded length of $z(\sigma_{max})/l_d = 90.2\%$. For the matrix cracking mode 5, the hysteresis loops correspond to the interface slip Case 1, i.e. the fiber/matrix interface partially debonding and the fiber sliding completely relative to the matrix in the interface debonding region upon unloading and reloading. Upon unloading, the interface counter slip length approaches to the interface debonded length at the transition stress of $\sigma_{tr\_pu} = 23.9$ MPa of $y(\sigma_{tr\_pu} = 23.9\,\text{MPa})/l_d = 1$; and upon reloading to the transition stress of $\sigma_{tr\_pr} = 215.1$ MPa, the interface new slip length approaches to the interface debonded length of $z(\sigma_{tr\_pr} = 215.1\,\text{MPa})/l_d = 1$.

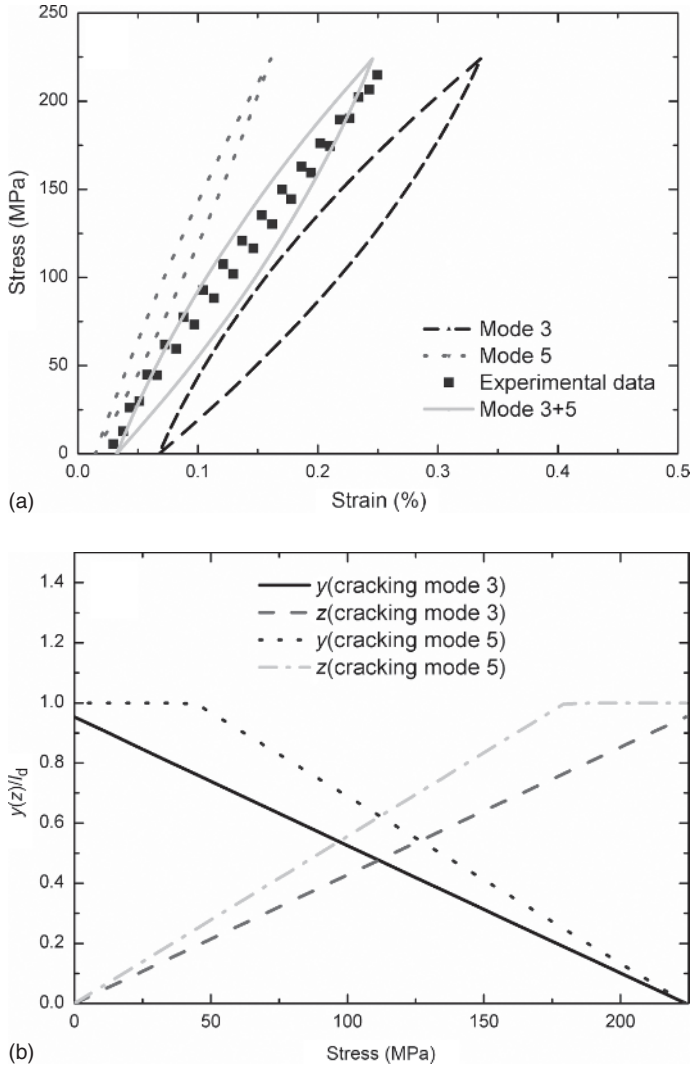

Figure 1.59 (a) The experimental and predicted fatigue hysteresis loops; and (b) the interface slip lengths of matrix cracking mode 3 and mode 5 of 2D SiC/SiC composite under the fatigue peak stress of $\sigma_{max} = 224$ MPa.

Under the fatigue peak stress of $\sigma_{max} = 253$ MPa, the experimental and theoretical fatigue hysteresis loops are shown in Figure 1.61a, in which the proportion of matrix cracking mode 3 is $\eta = 0.65$. For the matrix cracking mode 3, the fatigue hysteresis loops correspond to the interface slip Case 2, i.e. the fiber/matrix interface partially debonding and the fiber sliding partially relative to the matrix in the interface debonding region upon unloading and reloading, as shown in Figure 1.61b. Upon completely unloading, the interface counter slip length approaches to 86.4% of the interface debonded length, i.e. $y(\sigma_{min})/l_d = 86.4\%$; and upon reloading to peak stress, the interface new slip length approaches to 86.4%

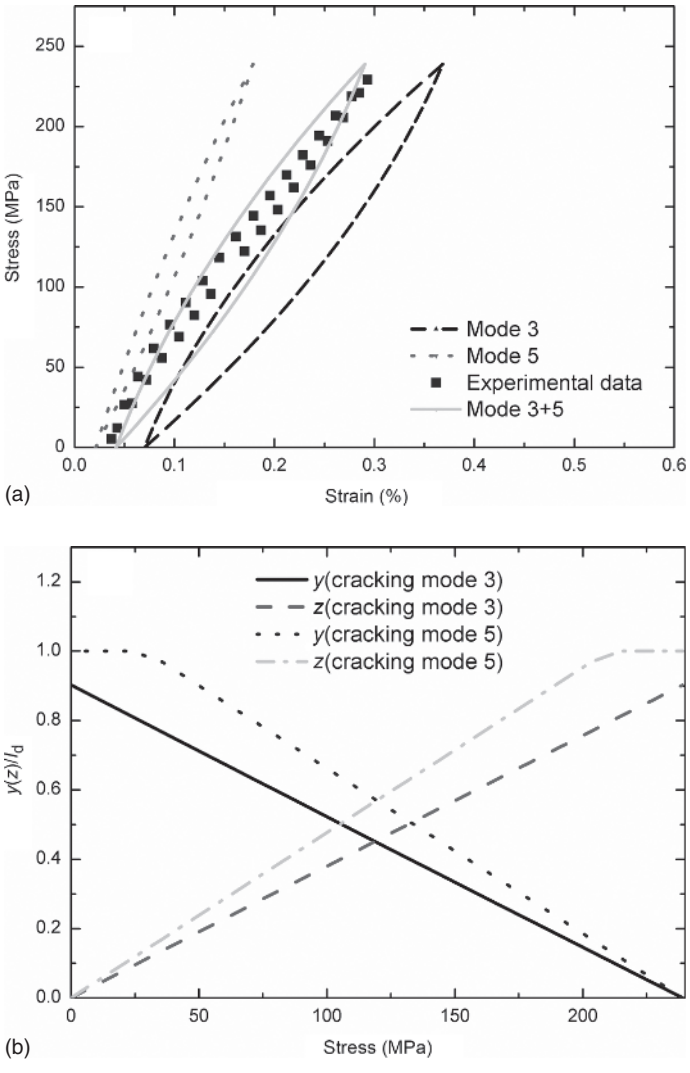

Figure 1.60 (a) The experimental and predicted fatigue hysteresis loops; and (b) the interface slip lengths of matrix cracking mode 3 and mode 5 of 2D SiC/SiC composite under the fatigue peak stress of $\sigma_{max} = 239$ MPa.

of the interface debonded length, i.e. $z(\sigma_{max})/l_d = 86.4\%$. For the matrix cracking mode 5, the fatigue hysteresis loops correspond to the interface slip Case 1, i.e. the fiber/matrix interface partially debonding and the fiber sliding completely relative to the matrix in the interface debonding region upon unloading and reloading. Upon unloading, the interface counter slip length approaches to the interface debonded length at the unloading transition stress of $\sigma_{tr\_pu} = 12.6$ MPa, i.e. $y(\sigma_{tr\_pu} = 12.6\,\text{MPa})/l_d = 1$; and upon reloading to the reloading transition stress of $\sigma_{tr\_pr} = 240.4$ MPa, the interface new slip length approaches to the interface debonded length, i.e. $z(\sigma_{tr\_pr} = 240.4\,\text{MPa})/l_d = 1$.

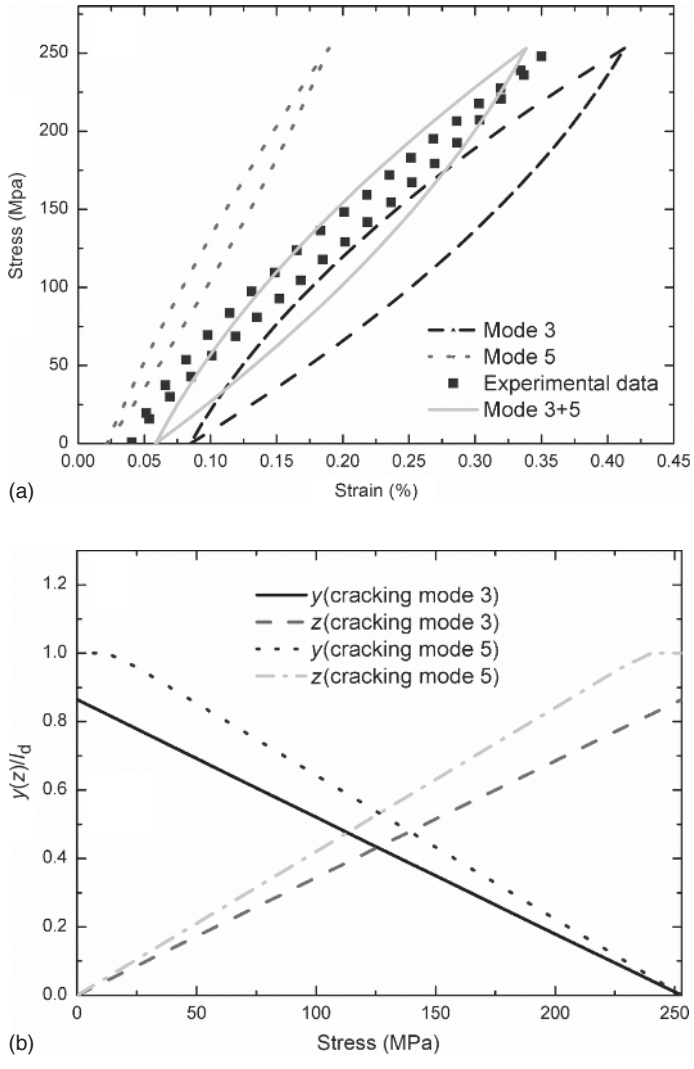

Figure 1.61 (a) The experimental and predicted fatigue hysteresis loops; and (b) the interface slip lengths of matrix cracking mode 3 and mode 5 of 2D SiC/SiC composite under the fatigue peak stress of $\sigma_{max} = 253$ MPa.

1.4 2.5D and 3D Ceramic-Matrix Composites

In this section, based on the analysis of the microstructure, the woven ceramic composites were divided into four elements: 0° warp yarns, 90° weft yarns, matrix outside of the yarns, and open porosity. By assuming that the mechanical hysteresis behavior of the woven ceramic composites is mainly controlled by the fiber/matrix interface slip in the 0° warp yarns, the unloading interface counter slip length and reloading interface new slip length are determined. The hysteresis loops of three cases include (i) the fiber/matrix interface partially debonding and

the fiber sliding partially relative to matrix in the interface debonded region of the 0° warp yarns; (ii) the fiber/matrix interface completely debonding and the fiber sliding partially relative to matrix in the interface debonded region of the 0° warp yarns; and (iii) the fiber/matrix interface completely debonding and the fiber sliding completely relative to matrix in the interface debonded region of the 0° warp yarns upon unloading and subsequent reloading, are derived. The fatigue hysteresis loops and hysteresis loss energy for the strain energy lost per volume during corresponding cycle for 2.5D C/SiC composite are predicted.

1.4.1 Materials and Experimental Procedures

1.4.1.1 2.5D C/SiC Composite

The 2.5D C/SiC composite was reinforced by a 2.5 dimensional woven T-300 carbon fiber (1K, Toray Co., Japan) preform. The preform of the 2.5D C/SiC composite is composed of layers of straight weft yarns and a set of sinusoidal warp yarns. The interlaminar strength of the composite is improved significantly due to interlaced warp yarns in the adjacent layers. Each yarn contained 6K fibers. The densities of the fiber in the warp and weft direction are 10 and 3 ends/cm, respectively. The reinforcement contained 20 layers of weft carbon fiber yarns. A low pressure CVI was used to prepare the composite. The PyC interphase with thickness of 0.2 μm was deposited on the carbon fibers. After SiC deposition, the contoured, edge-loaded test specimens were machined from the fabricated plates with 40 vol% fiber. The specimens were further coated with a SiC coating of about 50 μm in thickness. These processing steps resulted in a material having a bulk density about 2.1 g/cm^3 and an open porosity inherent to the CVI process in the range of 10–15 vol%.

The dog-bone shaped tension specimens were cut from an as-processing composite panel along the warp directions, and then the specimens were sealed with CVD SiC coating. The overall dimensions of the tensile specimens are 120 mm × 12 mm × 3.5 mm with a central reduced gage section of 30 mm × 10 mm × 3.5 mm. The cyclic loading/unloading tensile tests were measured using Instron 1196 test machine at a crosshead speed of 0.05 mm/min. Strains were recorded with an extensometer with a gage length of 25 mm.

1.4.1.2 3D Braided C/SiC Composite

Three-dimensional and four-directional braided fiber prefabricated sheets were obtained by two-step method. The fibers were T300 carbon fibers (Japan Toray, 1k), 240 mm × 60 mm × 3 mm in size, 40% in volume fraction, and 22° in braiding angle. A PyC interfacial layer was deposited on the surface of fibers by isothermal-low pressure chemical vapor infiltration (I-LCVI) process with a thickness of about 0.2 μm. SiC matrix was deposited in fiber preform by I-LCVI process. The deposition temperature was 1000 °C and the pressure was 5 kPa. The composite plate was cut into specimens along the length direction. Two layers of SiC coating were deposited on the surface of the sample by CVD. The thickness of each layer was about 20 μm, the deposition temperature was 1000 °C, and the pressure was 5 kPa. The cyclic loading and unloading tests were carried out on Instron 8801 test machine at a loading rate of 0.06 mm/min.

The strain was assessed directly by a contact Instron extensometer with a gage length of 25 mm. The cyclic unloading–reloading tests were performed up to final rupture of the composite specimens.

1.4.1.3 3D Needled C/SiC Composite

T300-3k carbon fibers from Toray Company of Japan were used to fabricate 2D needle-punched carbon fibers preform. Its characteristics of 0° non-woven fiber cloth, short fiber web, 90° non-woven fiber cloth, and needled fibers were successively superimposed. Relay needling technology was used to introduce carbon fiber bundles perpendicular to the ply direction to obtain three-dimensional prefabricated reinforcement. The fiber content is 30%. The ratio of short fiber web to non-woven fiber cloth is 1 : 3 in preform, and the needle density is 30–35 needles/cm^2. After the CVI, polymer impregnation and pyrolysis (PIP), and liquid silicon infiltration (LSI) processes for the 3D needled preforms, the 3D needled C/SiC composites were manufactured.

The cyclic loading and unloading tests were carried out on Instron 1186 test machine at a loading rate of 50 MPa/min. The specimen was loaded to a specific stress level and then unloaded at the same crosshead speed to zero load. Strains were recorded using strain gages clip-on on the specimens.

1.4.2 Hysteresis Theories

Based on the analysis of the microstructure, the CMCs are divided into four elements: 0° warp yarns, 90° weft yarns, matrix outside of the yarns, and open porosity. If matrix cracking and fiber/matrix interface debonding in the 0° warp yarns are present upon first loading of woven ceramic composites, the stress–strain hysteresis loops would develop attributed to the interface frictional sliding between the fiber and matrix in the 0° warp yarns during unloading and subsequent reloading. The shape, size, and location of the hysteresis loops depend upon the fiber/matrix interface debonding and slipping. The hysteresis loops of three cases are discussed in the following:

(1) Case 1, the fiber/matrix interface partially debonds and fiber slides partially relative to matrix in the debonded region upon unloading/reloading.
(2) Case 2, the fiber/matrix interface completely debonds and fiber slides partially relative to matrix in the interface debonded region upon unloading/reloading
(3) Case 3, the fiber/matrix interface completely debonds and fiber slides completely relative to matrix in the interface debonded region upon unloading/reloading.

1.4.2.1 Interface Slip Case 1

When $\sigma_{max} < \sigma_b$, the fiber/matrix interface partially debonds upon first loading to the fatigue peak stress:

$$\sigma_b = \frac{V_{f0}}{1 - V_{f0}} \frac{E_{inner0}}{E_{m\text{-}mini}} \frac{l_c}{r_f} \tau_i - \sigma_{th} \tag{1.118}$$

where E_{inner0} denotes the elastic modulus of the 0° warp yarns, $E_{\text{m-mini}}$ denotes the elastic modulus of the 90° weft yarns and outside matrix, V_{f0} denotes the volume fraction of fiber along the 0° warp yarns direction, l_{c} denotes the matrix cracking space in the 0° warp yarns, r_{f} denotes the fiber radius, τ_{i} denotes the fiber/matrix interface shear stress, and σ_{th} denotes the thermal residual stress of the composites.

The unit cell of the 0° warp yarns can be divided into the interface debonded region and the interface bonded region. Upon unloading, the interface debonded region can be divided into the interface counter slip region and the interface slip region. The fiber axial stress distribution during unloading can be described using the following equation:

$$\begin{cases} \sigma_{\text{f}}(x) = \frac{\sigma}{V_{\text{f0}}} + \frac{2\tau_{\text{i}}}{r_{\text{f}}}x, & x \in (0, y) \\ \sigma_{\text{f}}(x) = \frac{\sigma}{V_{\text{f0}}} + \frac{2\tau_{\text{i}}}{r_{\text{f}}}(2y - x), & x \in (y, l_{\text{d}}) \\ \sigma_{\text{f}}(x) = \frac{E_{\text{f}}}{E_{\text{c}}}\sigma - \frac{(1-V_{\text{f0}})E_{\text{m-mini}}}{V_{\text{f0}}E_{\text{innier0}}}\sigma_{\text{th}}, & x \in (l_{\text{d}}, l_{\text{c}}/2) \end{cases} \tag{1.119}$$

where the unloading interface counter slip length y is can be described using the following equation:

$$y = \frac{r_{\text{f}}}{4\tau_{\text{i}}}\frac{1 - V_{\text{f0}}}{V_{\text{f0}}}\frac{E_{\text{m-mini}}}{E_{\text{inner0}}}(\sigma_{\max} - \sigma) \tag{1.120}$$

Upon reloading to σ ($\sigma_{\min} < \sigma < \sigma_{\max}$), slip again occurs near the matrix crack plane over a distance z, which denotes the new interface slip length. The interface debonded region can be divided into the new slip region, counter slip region, and slip region. The fiber axial stress distribution during reloading can be described using the following equation:

$$\begin{cases} \sigma_{\text{f}}(x) = \frac{\sigma}{V_{\text{f0}}} - \frac{2\tau_{\text{i}}}{r_{\text{f}}}x, & x \in (0, z) \\ \sigma_{\text{f}}(x) = \frac{\sigma}{V_{\text{f0}}} - \frac{2\tau_{\text{i}}}{r_{\text{f}}}(2z - x), & x \in (z, y) \\ \sigma_{\text{f}}(x) = \frac{\sigma}{V_{\text{f0}}} + \frac{2\tau_{\text{i}}}{r_{\text{f}}}2(y - z) - \frac{2\tau_{\text{i}}}{r_{\text{f}}}x, & x \in (y, l_{\text{d}}) \\ \sigma_{\text{f}}(x) = \frac{E_{\text{f}}}{E_{\text{c}}}\sigma - \frac{(1-V_{\text{f0}})E_{\text{m-mini}}}{V_{\text{f0}}E_{\text{inner0}}}\sigma_{\text{th}}, & x \in (l_{\text{d}}, l_{\text{c}}/2) \end{cases} \tag{1.121}$$

where the interface new slip length z can be determined using the following equation:

$$z = y(\sigma_{\min}) - \frac{r_{\text{f}}}{4\tau_{\text{i}}}\frac{1 - V_{\text{f0}}}{V_{\text{f0}}}\frac{E_{\text{m-mini}}}{E_{\text{inner0}}}(\sigma_{\max} - \sigma) \tag{1.122}$$

1.4.2.2 Interface Slip Case 2

When $\sigma_{\text{b}} < \sigma_{\max} < \sigma_{\text{p}}$, the fiber/matrix interface completely debonds upon first loading to the fatigue peak stress. Upon completely unloading, the interface counter slip length y is less than the half matrix crack spacing $l_{\text{c}}/2$, i.e. $y(\sigma_{\min}) < l_{\text{c}}/2$:

$$\sigma_{\text{p}} = 2\frac{V_{\text{f0}}}{1 - V_{\text{f0}}}\frac{E_{\text{inner0}}}{E_{\text{m-mini}}}\frac{l_{\text{c}}}{r_{\text{f}}}\tau_{\text{i}} + \sigma_{\min} \tag{1.123}$$

The fiber axial stress during unloading can be described using the following equation:

$$\begin{cases} \sigma_f(x) = \frac{\sigma}{V_{f0}} + \frac{2\tau_i}{r_f}x, & x \in (0, y) \\ \sigma_f(x) = \frac{\sigma}{V_{f0}} + \frac{2\tau_i}{r_f}(2y - x), & x \in (y, l_c/2) \end{cases} \tag{1.124}$$

where the unloading interface counter slip length is given by Eq. (1.120).

The fiber axial stress distribution upon reloading can be described using the following equation:

$$\begin{cases} \sigma_f(x) = \frac{\sigma}{V_{f0}} - \frac{2\tau_i}{r_f}x, & x \in (0, z) \\ \sigma_f(x) = \frac{\sigma}{V_{f0}} - \frac{2\tau_i}{r_f}(2z - x), & x \in (z, y) \\ \sigma_f(x) = \frac{\sigma}{V_{f0}} + \frac{2\tau_i}{r_f}2(y - z) - \frac{2\tau_i}{r_f}x, & x \in (y, l_c/2) \end{cases} \tag{1.125}$$

where the reloading interface new slip length is given by Eq. (1.122).

1.4.2.3 Interface Slip Case 3

When $\sigma_p < \sigma_{max}$, upon unloading to the transition stress of σ_{tr_fu} ($\sigma_{tr\_fu} > \sigma_{min}$), the interface counter slip length reaches the half matrix crack spacing $l_c/2$, i.e. $y(\sigma_{tr\_fu}) = l_c/2$:

$$\sigma_{tr\_fu} = \sigma_{max} - 2\frac{V_{f0}}{1 - V_{f0}}\frac{E_{inner0}}{E_{m\text{-}mini}}\frac{l_c}{r_f}\tau_i \tag{1.126}$$

When $\sigma > \sigma_{tr\_fu}$, the interface counter slip length y is less than the half matrix crack spacing $l_c/2$, $y(\sigma > \sigma_{tr\_fu}) < l_c/2$. The fiber axial stress distribution is given by Eq. (1.124). When $\sigma < \sigma_{tr\_fu}$, the interface counter slip length occupies the entire matrix crack spacing, and the fiber axial stress distribution is given by Eq. (1.124) by setting $y = l_c/2$.

Upon reloading to the transition stress of σ_{tr_fr} ($\sigma_{tr\_fr} < \sigma_{max}$), the interface new slip length z reaches the half matrix crack spacing $l_c/2$, i.e. $z(\sigma_{tr\_fr}) = l_c/2$:

$$\sigma_{tr\_fr} = \sigma_{min} + 2\frac{V_{f0}}{1 - V_{f0}}\frac{E_{inner0}}{E_{m\text{-}mini}}\frac{l_c}{r_f}\tau_i \tag{1.127}$$

When $\sigma < \sigma_{tr\_fr}$, the interface new slip length z is less than the half matrix crack spacing $l_c/2$, i.e. $z < l_c/2$. The fiber axial stress distribution is given by Eq. (1.125). When $\sigma_{tr\_fr} < \sigma < \sigma_{max}$, new slip length occurs over the entire matrix crack spacing, and the fiber axial stress distribution is given by Eq. (1.125) by setting $z = l_c/2$.

1.4.2.4 Hysteresis Loops

When damage forms within the composites, the composite strain is determined from Eq. (1.128), which assumes that the composite strain is equivalent to the average strain in an undamaged fiber. The undamaged fiber is bridging a matrix crack.

$$\varepsilon_c = \frac{2}{E_f l_c}\int_{l_c/2} \sigma_f(x)\mathrm{d}x - (\alpha_c - \alpha_f)\Delta T \tag{1.128}$$

Substituting Eq. (1.119) into Eq. (1.128), the unloading stress–strain relationship for the interface partially debonding and fiber sliding partially relative to matrix can be described using the following equation:

$$\varepsilon = \frac{\sigma}{E_c} + 3\frac{1-V_{f0}}{V_{f0}}\frac{E_{m\text{-}mini}}{E_f E_{inner0}}\frac{l_d}{l_c}(\sigma+\sigma_{th}) - 2\frac{1-V_{f0}}{V_{f0}}\frac{E_{m\text{-}mini}}{E_f E_{inner0}}\frac{l_d}{l_c}(\sigma+\sigma_{th})\left(1-\frac{y}{l_d}\right)^2 \tag{1.129}$$

Substituting Eq. (1.121) into Eq. (1.128), the reloading stress–strain relationship for the interface partially debonding and fiber sliding partially relative to matrix can be described using the following equation:

$$\varepsilon = \frac{\sigma}{E_c} + \frac{1-V_{f0}}{V_{f0}}\frac{E_{m\text{-}mini}}{E_f E_{inner0}}\frac{l_d}{l_c}(\sigma+\sigma_{th}) + 2\frac{1-V_{f0}}{V_{f0}}\frac{E_{m\text{-}mini}}{E_f E_{inner0}}\frac{l_d}{l_c}(\sigma+\sigma_{th})\left[\left(\frac{z}{l_d}-1\right)^2-\left(\frac{y}{l_d}-1\right)^2\right] \tag{1.130}$$

Substituting Eq. (1.124) into Eq. (1.128), the unloading stress–strain relationship for the interface completely debonding and fiber sliding partially relative to matrix can be described using the following equation:

$$\varepsilon = \frac{\sigma}{E_c} + \frac{3}{2}\frac{1-V_{f0}}{V_{f0}}\frac{E_{m\text{-}mini}}{E_f E_{inner0}}(\sigma+\sigma_{th}) - \frac{1-V_{f0}}{V_{f0}}\frac{E_{m\text{-}mini}}{E_f E_{inner0}}(\sigma+\sigma_{th})\left(1-\frac{2y}{l_c}\right)^2 \tag{1.131}$$

Substituting Eq. (1.125) into Eq. (1.128), the reloading stress–strain relationship for the interface completely debonding and fiber sliding partially relative to matrix can be described using the following equation:

$$\varepsilon = \frac{\sigma}{E_c} + \frac{1}{2}\frac{1-V_{f0}}{V_{f0}}\frac{E_{m\text{-}mini}}{E_f E_{inner0}}(\sigma+\sigma_{th}) + \frac{1-V_{f0}}{V_{f0}}\frac{E_{m\text{-}mini}}{E_f E_{inner0}}(\sigma+\sigma_{th})\left[\left(\frac{2z}{l_c}-1\right)^2-\left(\frac{2y}{l_c}-1\right)^2\right] \tag{1.132}$$

When fiber completely slides relative to matrix upon unloading/reloading, the unloading stress–strain relationship is divided into two parts. When $\sigma > \sigma_{tr\_fu}$, the unloading stress–strain relationship is given by Eq. (1.131); when $\sigma < \sigma_{tr\_fu}$, the unloading strain is given by Eq. (1.131) by setting $y = l_c/2$. The reloading stress–strain relationship is divided into two parts too. When $\sigma < \sigma_{tr\_fr}$, the reloading stress–strain relationship is given by Eq. (1.132); when $\sigma > \sigma_{tr\_fr}$, the reloading strain is given by Eq. (1.132) by setting $z = l_c/2$.

1.4.3 Experimental Comparisons

1.4.3.1 2.5D C/SiC Composite

The cyclic loading/unloading tensile stress–strain curves of 2.5D C/SiC at room temperature are shown in Figure 1.62 (Wang et al. 2008). The composite was

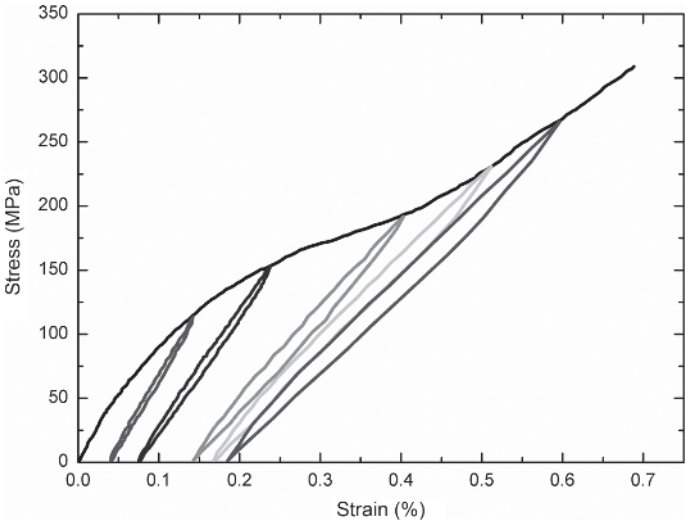

Figure 1.62 The cyclic loading/unloading hysteresis loops of 2.5D C/SiC composite at room temperature.

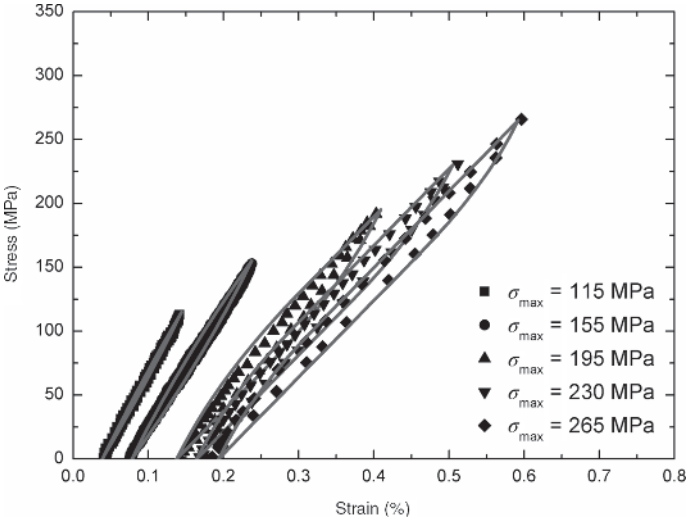

Figure 1.63 The experimental and theoretical hysteresis loops of 2.5D C/SiC composite corresponding to different fatigue peak stresses.

unloading and subsequent reloading at the peak stresses of σ_{max} = 115, 155, 195, 230, and 265 MPa and failed at the stress of σ_{UTS} = 308 MPa with failure strain of ε_f = 0.68%. The experimental and theoretical hysteresis loops corresponding to σ_{max} = 115, 155, 195, 230, and 265 MPa are shown in Figure 1.63. The fatigue hysteresis dissipated energy increases from U = 5.8 kJ/m^3 at the fatigue peak stress of σ_{max} = 115 MPa to U = 61.1 kJ/m^3 at the fatigue peak stress of σ_{max} = 265 MPa; and the fatigue hysteresis modulus decreases from

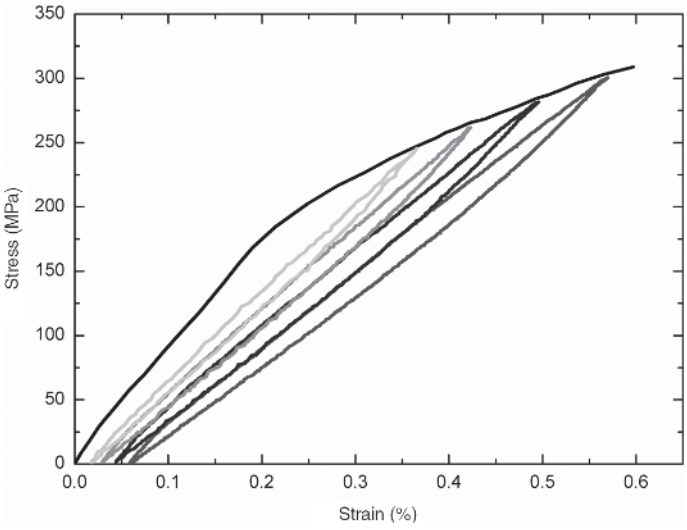

Figure 1.64 The cyclic loading/unloading hysteresis loops of 3D braided C/SiC composite at room temperature.

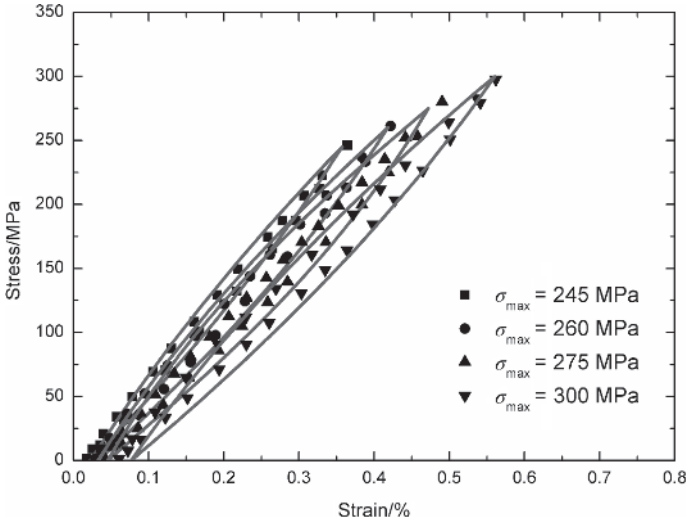

Figure 1.65 The experimental and theoretical hysteresis loops of 3D braided C/SiC composite corresponding to different fatigue peak stresses.

$E = 110.6\,\text{GPa}$ at the fatigue peak stress of $\sigma_{\max} = 115\,\text{MPa}$ to $E = 64.2\,\text{GPa}$ at the fatigue peak stress of $\sigma_{\max} = 265\,\text{MPa}$.

1.4.3.2 3D Braided C/SiC Composite

The cyclic loading/unloading tensile stress–strain curves of 3D braided C/SiC at room temperature are shown in Figure 1.64 (Mei and Cheng 2009). The composite was unloading and subsequent reloading at the peak stresses of $\sigma_{\max} = 245$,

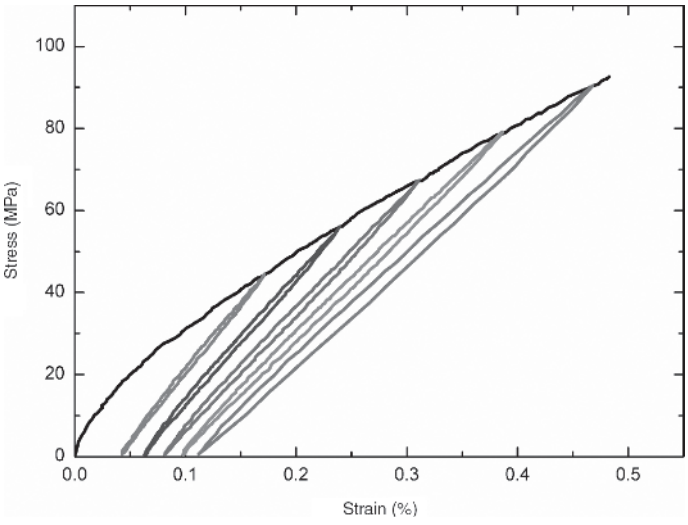

Figure 1.66 The cyclic loading/unloading hysteresis loops of 3D needled C/SiC composite at room temperature.

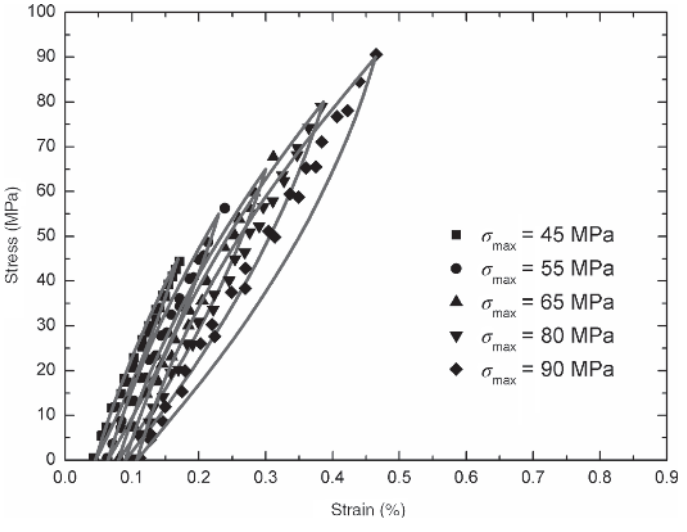

Figure 1.67 The experimental and theoretical hysteresis loops of 3D needled C/SiC composite corresponding to different fatigue peak stresses.

260, 275, and 300 MPa and failed at the stress of $\sigma_{UTS} = 308$ MPa with failure strain of $\varepsilon_f = 0.59\%$. The experimental and theoretical hysteresis loops corresponding to $\sigma_{max} = 245$, 260, 275, and 300 MPa are illustrated in Figure 1.65. The fatigue hysteresis dissipated energy increases from $U = 35.1\,kJ/m^3$ at the fatigue peak stress of $\sigma_{max} = 245$ MPa to $U = 76.2\,kJ/m^3$ at the fatigue peak stress of $\sigma_{max} = 300$ MPa; and the fatigue hysteresis modulus decreases from $E = 70.5$ GPa

at the fatigue peak stress of $\sigma_{max} = 245$ MPa to $E = 59.1$ GPa at the fatigue peak stress of $\sigma_{max} = 300$ MPa.

1.4.3.3 3D Needled C/SiC Composite

The cyclic loading/unloading tensile stress–strain curves of 3D needled C/SiC at room temperature are shown in Figure 1.66 (Xie et al. 2016). The composite was unloading and subsequent reloading at the peak stresses of $\sigma_{max} = 45$, 55, 65, 80, and 90 MPa and failed at the stress of $\sigma_{UTS} = 92.6$ MPa with failure strain of $\varepsilon_f = 0.48\%$. The experimental and theoretical hysteresis loops corresponding to $\sigma_{max} = 45$, 55, 65, 80, and 90 MPa are shown in Figure 1.67. The fatigue hysteresis dissipated energy increases from $U = 1.6$ kJ/m^3 at the fatigue peak stress of $\sigma_{max} = 45$ MPa to $U = 10.6$ kPa at the fatigue peak stress of $\sigma_{max} = 90$ MPa; and the fatigue hysteresis modulus decreases from $E = 34.1$ GPa at the fatigue peak stress of $\sigma_{max} = 45$ MPa to $E = 25.4$ GPa at the fatigue peak stress of $\sigma_{max} = 90$ MPa.

1.5 Conclusions

In this chapter, the cyclic loading/unloading hysteresis behavior of CMCs with different fiber preforms, i.e. unidirectional, cross-ply, 2D and 2.5D woven, 3D braided, and 3D needled, have been investigated. Based on fiber sliding mechanisms, the hysteresis loop models considering different interface slip cases have been developed. The unloading interface counter slip length and reloading interface new slip length have been determined by the fracture mechanics approach. The effects of fiber volume fraction, matrix cracking density, interface shear stress, interface debonded energy, and fiber failure on the hysteresis loops, hysteresis dissipated energy, hysteresis width, and hysteresis modulus have been analyzed. The hysteresis loops, hysteresis dissipated energy, and hysteresis modulus of unidirectional, cross-ply, 2D and 2.5D woven, 3D braided, and 3D needled CMCs have been predicted.

References

Ahn, B.K. and Curtin, W.A. (1997). Strain and hysteresis by stochastic matrix cracking in ceramic matrix composites. *Journal of Mechanics and Physics of Solids* 45: 177–209.

Aveston, J., Cooper, G.A., and Kelly, A. (1971). Single and multiple fracture. In: *Properties of Fiber Composites: Conference on Proceedings*, 15–26. England: National Physical Laboratory, IPC.

Budiansky, B., Hutchinson, J.W., and Evans, A.G. (1986). Matrix fracture in fiber-reinforced ceramics. *Journal of Mechanics and Physics of Solids* 34: 167–189.

Cao, H.C. and Thouless, M.D. (1990). Tensile tests of ceramic-matrix composites: theory and experiment. *Journal of the American Ceramic Society* 73: 2091–2094.

Cheng, Q.Y. (2010). Simulation and assessment on the low velocity impact properties of plain woven C/SiC composites. PhD thesis. Northwestern Polytechnical University, Xi'an, China.

Chiang, Y.C. (2001). On fiber debonding and matrix cracking in fiber-reinforced ceramics. *Composites Science and Technology* 61: 1743–1756.

Curtin, W.A. (1991). Theory of mechanical properties of ceramic-matrix composites. *Journal of the American Ceramic Society* 74: 2837–2845.

Curtin, W.A. (1993). Multiple matrix cracking in brittle matrix composites. *Acta Metallurgica et Materialia* 41: 1369–1377.

Curtin, W.A. (1994). In situ fiber strength in ceramic-matrix composites from fracture mirrors. *Journal of the American Ceramic Society* 77: 1075–1078.

Curtin, W.A. (2000, 2000). *Stress–Strain Behavior of Brittle Matrix Composites*, Comprehensive Composite Materials, vol. 4, 47–76. Elsevier Science Ltd.

Curtin, W.A., Ahn, B.K., and Takeda, N. (1998). Modeling brittle and tough stress-strain behavior in unidirectional ceramic matrix composites. *Acta Materialia* 46: 3409–3420.

Dalmaz, A., Reynaud, P., Rouby, D., and Fantozzi, G. (1996). Damage propagation in carbon/silicon carbide composites during tensile tests under the SEM. *Journal of Materials Science* 31: 4213–4219.

Daniel, I.M. and Lee, J.W. (1993). The behavior of ceramic matrix fiber composites under longitudinal loading. *Composites Science and Technology* 46: 105–113.

Dutton, R.E., Pagano, N.J., and Kim, R.Y. (2000). Modeling the ultimate tensile strength of unidirectional glass-matrix composites. *Journal of the American Ceramic Society* 83: 166–174.

Evans, A.G., Zok, F.W., and McMeeking, R.M. (1995). Fatigue of ceramic matrix composites. *Acta Metallurgica et Materialia* 43: 859–875.

Fantozzi, G. and Reynaud, P. (2009). Mechanical hysteresis in ceramic matrix composites. *Materials Science and Engineering A* 521–522: 18–23.

Fantozzi, G., Reynaud, P., and Rouby, D. (2001). Thermomechanical behavior of long fibers ceramic–ceramic composites. *Silicates Industriels* 66: 109–119.

French National Organization for Standardization (1989). Determination of tensile characteristics of ceramic matrix composites with 1D, 2D, 3D reinforcements at room temperature. Paris, August 1989.

Fukunaga, H., Chou, T.W., Peters, P.W.M., and Schulte, K. (1984). Probabilistic failure strength analysis of graphite/epoxy cross-ply laminates. *Journal of Composite Materials* 18: 339–356.

Gao, Y.C., Mai, Y.W., and Cotterell, B. (1988). Fracture of fiber-reinforced materials. *Journal of Applied Mathematics and Physics* 39: 550–572.

Garrett, K.W. and Bailey, J.E. (1977). Multiple transverse fracture in 90° cross-ply laminates of a glass fiber-reinforced polyester. *Journal of Materials Science* 12: 157–168.

Hild, F., Domergue, J.M., Leckie, F.A., and Evans, A.G. (1994). Tensile and flexural ultimate strength of fiber-reinforced ceramic-matrix composites. *International Journal of Solids and Structure* 31: 1035–1045.

Hsueh, C.H. (1996). Crack-wake interface debonding criterion for fiber-reinforced ceramic composites. *Acta Materialia* 44: 2211–2216.

Keith, W.P. and Kedward, K.T. (1995). The stress–strain behavior of a porous unidirectional ceramic matrix composite. *Composites* 26: 163–174.

Kotil, T., Holmes, J.W., and Comninou, M. (1990). Origin of hysteresis observed during fatigue of ceramic-matrix composites. *Journal of the American Ceramic Society* 73: 1879–1883.

Kun, F. and Herrmann, H.J. (2000). Damage development under gradual loading of composites. *Journal of Materials Science* 35: 4685–4693.

Kuo, W.S. and Chou, T.W. (1995). Multiple cracking of unidirectional and cross-ply ceramic matrix composites. *Journal of the American Ceramic Society* 78: 745–755.

Laws, N. and Dvorak, G.J. (1988). Progressive transverse cracking in composite laminates. *Journal of Composite Materials* 22: 900–916.

Lee, J.W. and Daniel, I.M. (1990). Progressive transverse cracking of crossply composite laminates. *Journal of Composite Materials* 24: 1225–1243.

Li, L. (2013). Modeling hysteresis behaviour of cross-ply C/SiC ceramic matrix composites. *Composites Part B* 53: 36–45.

Li, L. (2016a). Hysteresis loops of carbon fiber-reinforced ceramic-matrix composites with different fiber preforms. *Ceramics International* 42: 16535–16551.

Li, L. (2016b). Modeling the effect of multiple matrix cracking modes on cyclic hysteresis loops of 2D woven ceramic-matrix composites. *Applied Composite Materials* 23: 555–581.

Li, L. and Song, Y.D. (2010a). An approach to estimate interface shear stress of ceramic matrix composites from hysteresis loops. *Applied Composite Materials* 17: 309–328.

Li, L. and Song, Y.D. (2010b). Fatigue behavior of cross-ply C/SiC ceramic matrix composites at ambient and elevated temperatures. In: *The 7th International Conference on High Temperature Ceramic Matrix Composites (20–22 September 2010)*, 314–319. Germany: Bayreuth.

Li, L. and Song, Y.D. (2011a). Estimate interface frictional coefficient of ceramic matrix composites from hysteresis loops. *Journal of Composite Materials* 45: 989–1006.

Li, L. and Song, Y.D. (2011b). Influence of fiber failure on fatigue hysteresis loops of ceramic matrix composites. *Journal of Reinforced Plastics and Composites* 30: 12–25.

Li, L., Song, Y.D., and Sun, Z.G. (2009). Influence of interface debonding on the fatigue hysteresis loops of ceramic matrix composites. *Chinese Journal of Solid Mechanics* 30: 8–14.

Li, L., Song, Y., and Sun, Y. (2013). Modeling loading/unloading hysteresis behaviour of unidirectional C/SiC ceramic matrix composites. *Applied Composite Materials* 20: 655–672.

Li, P., Wang, B., Zhen, W., and Jiao, G. (2014). Tensile loading/unloading stress-strain behavior of 2D SiC/SiC composites. *Acta Materiae Compositae Sinica* 31: 676–682.

Liao, K. and Reifsnider, K.L. (2000). A tensile strength model for unidirectional fiber-reinforced brittle matrix composite. *International Journal of Fracture* 106: 95–115.

Mei, H. and Cheng, L.F. (2009). Comparison of the mechanical hysteresis of carbon/ceramic-matrix composites with different fiber performs. *Carbon* 47: 1034–1042.

Naslain, R. (2004). Design, preparation and properties of non-oxide CMCs for application in engines and nuclear reactors: an overview. *Composites Science and Technology* 64: 155–170.

Paar, R., Valles, J.L., and Danzer, R. (1998). Influence of fiber properties on the mechanical behavior of unidirectionally-reinforced ceramic matrix composites. *Materials Science and Engineering A* 250: 209–216.

Phoenix, S.L. and Raj, R. (1992). Scalings in fracture probabilities for a brittle matrix fiber composite. *Acta Metallurgica et Materialia* 40: 2813–2828.

Pryce, A.W. and Smith, P.A. (1993). Matrix cracking in unidirectional ceramic matrix composites under quasi-static and cyclic loading. *Acta Metallurgica et Materialia* 41: 1269–1281.

Ramakrishnan, N. and Arunachalam, V.S. (1993). Effective elastic moduli of porous ceramic materials. *Journal of the American Ceramic Society* 76: 2745–2752.

Reynaud, P. (1996). Cyclic fatigue of ceramic-matrix composites at ambient and elevated temperatures. *Composites Science and Technology* 56: 809–814.

Rouby, D. and Reynaud, P. (1993). Fatigue behavior related to interface modification during load cycling in ceramic-matrix fiber composites. *Composites Science and Technology* 48: 109–118.

Schwietert, H.R. and Steif, P.S. (1990). A theory for the ultimate strength of a brittle-matrix composite. *Journal of the Mechanics and Physics of Solids* 38: 325–343.

Solti, J.P., Mall, S., and Robertson, D.D. (1995). Modeling damage in unidirectional ceramic-matrix composites. *Composites Science and Technology* 54: 55–66.

Sun, Y.J. and Singh, R.N. (1998). The generation of multiple matrix cracking and fiber-matrix interfacial debonding in a glass composite. *Acta Materialia* 46: 1657–1667.

Sutcu, M. (1989). Weibull statistics applied to fiber failure in ceramic composites and work of fracture. *Acta Metallurgica et Materialia* 37: 651–661.

Takeda, N. and Kiriyama, M. (1999). Matrix crack evolution in SiC fiber/glass matrix cross-ply laminates. *Composites: Part A* 30: 593–597.

Thouless, M.D. and Evans, A.G. (1988). Effects of pull-out on the mechanical properties of ceramic matrix composites. *Acta Metallurgica et Materialia* 36: 517–522.

Wang, Y.Q., Zhang, L.T., Cheng, L.F. et al. (2008). Tensile performance and damage evolution of a 2.5D C/SiC composite characterized by acoustic emission. *Applied Composite Materials* 15: 183–188.

Weitsman, Y. and Zhu, H. (1993). Multiple-fracture of ceramic composites. *Journal of the Mechanics and Physics of Solids* 41: 351–388.

Xia, Z.H. and Curtin, W.A. (2000). Toughness-to-brittle transitions in ceramic-matrix composites with increasing interfacial shear stress. *Acta Materialia* 48: 4879–4892.

Xie, J.B., Fang, G.D., Chen, Z., and Liang, J. (2016). Modeling of nonlinear mechanical behavior for 3D needled C/C-SiC composites under tensile load. *Applied Composite Materials* 23: 1–15.

Yang, B. and Mall, S. (2003). Cohesive-shear-lag model for cycling stress-strain behavior of unidirectional ceramic matrix composites. *International Journal of Damage Mechanics* 12: 45–64.

Zhou, S.J. and Curtin, W.A. (1995). Failure of fiber composites: a lattice green function model. *Acta Metallurgica et Materialia* 43: 3093–3104.

Zhu, H. and Weitsman, Y. (1994). The progression of failure mechanisms in unidirectional reinforced ceramic composites. *Journal of Mechanics and Physics of Solids* 42: 1601–1632.

Zok, F.W. and Spearing, S.M. (1992). Matrix crack spacing in brittle matrix composites. *Acta Metallurgica et Materialia* 40: 2033–2043.